UNIVERSITY
OF TRENTO - Italy
DEPARTMENT OF INDUSTRIAL ENGINEERING

XXXV cycle

Doctoral School in Materials, Mechatronics
and Systems Engineering

Progress on 2D-MoS_2: development of a scalable fabrication method and demonstration of an X-ray detector

Alberto Taffelli

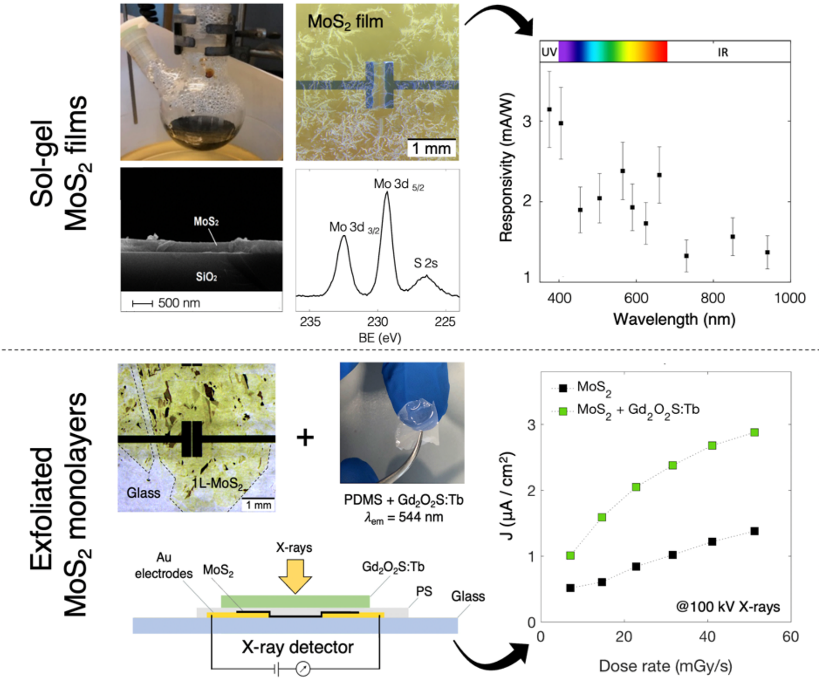

July 2023

PROGRESS ON 2D-MoS_2: DEVELOPMENT OF A SCALABLE FABRICATION METHOD AND DEMONSTRATION OF AN X-RAY DETECTOR

Alberto Taffelli, PhD candidate
E-mail:alberto.taffelli@unitn.it

Prof. Lucio Pancheri, Advisor
Department of Industrial Engineering
University of Trento, Italy.

Prof. Emil J.W.List-Kratochvil, Co-Advisor
IRIS Adlershof Center
Humboldt University, Berlin.

Prof. Sandra Dirè, Co-advisor
Department of Industrial Engineering
University of Trento, Italy.

Prof. Alberto Quaranta, Co-advisor
Department of Industrial Engineering
University of Trento, Italy.

University of Trento,
Department of Industrial Engineering

July 2023

Table of Contents

Abstract

Two-dimensional transition metal dichalcogenides (TMDCs) aroused significant interest in the last years as semiconductor materials for application in the field of electronics, due to their tunable bandgap, good carrier mobility, and strong light absorption. Among TMDCs, two-dimensional molybdenum disulfide (2D-MoS_2) has been the most investigated for electronic and optoelectronic applications, like transistors and photodetectors. 2D-MoS_2 can particularly benefit from the excellent light matter interaction properties in the UV-VIS spectrum combined with good charge carrier transport properties. The literature reports photodetectors based on 2D-MoS_2 fabricated with different techniques, including exfoliation, chemical vapor deposition (CVD) and wet chemical synthesis. However, it is still challenging to scale the proposed devices to the industrial level, due to the lack of a versatile fabrication process that ensures both reproducibility and scalability.

A possible solution to this could rise from wet chemical synthesis. In the first part of this work, I discuss the development and optimization of a fabrication method for MoS_2 thin films based on a sol-gel process which allows for scalable productions. This route allowed the fabrication of large area (~cm^2) MoS_2 thin films of 200 nm thickness on technological relevant substrates (i.e., glass, gold, silicon). The films displayed good uniformity, although the crystallinity was affected by residual impurities. The films produced with this technique were employed for the fabrication of photodetectors, displaying responsivity of few mA/W in the NUV-VIS-NIR spectrum. However, the performance of the device was affected by a still limited quality of the MoS_2 films obtained with the current method that require further optimization. Further studies will overcome the current limitations and solutions to be investigated in future works are proposed.

The second part of this work focuses on expanding the detection capability of 2D-MoS_2 (currently limited to the UV-VIS-NIR spectrum), by exploring for the first time X-rays sensing, taking advantage of the X-ray cross section of MoS_2 associated with the high atomic number Z of Mo. A detector based on an exfoliated MoS_2 monolayer (1L-MoS_2) was fabricated and characterized for the purpose. The detector showed direct detection of ~10^2 keV X-rays down to dose rates of 0.08 mGy/s, with X-ray sensitivity is in the range 10^8-10^9 $\mu C \cdot Gy^{-1} \cdot cm^{-3}$, outperforming most of the reported organic and inorganic materials. A strategy to improve the device response was also studied by adding a scintillator film, which resulted in a three-fold increase of the signal. These results suggest to consider 2D-MoS_2 for in-vivo dosimetry applications.

Introduction

Two-dimensional (2D) materials have gained tremendous attention in the scientific community since graphene was first exfoliated by A. Geim, K. Novoselov in 2004 [1], which contributed to their Nobel Prize winning in Physics in 2010. With respect to their bulk counterpart, 2D materials, generally intended as single or few layer materials, have ultra-high specific surface area, enabling their electronic properties to be very sensitive to external perturbations. This allows the fabrication of sensitive and tunable electronic devices. Also, their 2D structure permits to build ultra-thin devices, matching the recent interest of electronics to become flexible and wearable.

Among 2D materials, transition metal dichalcogenides (TMDCs), have attracted interest for the field of electronics in the last decade. Differently from graphene, which suffers in several applications from the absence of a bandgap in its energy structure, TMDCs are indeed semiconductors, they possess a finite bandgap, which is direct in the monolayer limit. Among TMDCs, two-dimensional molybdenum disulfide (2D-MoS_2) has been the most studied material. 2D-MoS_2 displays remarkable light matter interaction in the ultraviolet and visible (UV-VIS) spectral range and possess excellent charge transport properties, fundamental characteristics that can be exploited for electronic and optoelectronic applications.

In 2011 Radisavljevic et al. [2] published a contribution reporting a transistor based on a molybdenum disulfide monolayer (1L-MoS_2), demonstrating for the first time its enormous potential in the field of electronics and opening the way for the production of devices based on MoS_2. Since then, efforts of research focused on the fabrication of 2D-MoS_2 and works have been published on transistors, photodetectors, LEDs, solar cells, hydrogen evolution reactors and photoelectrochemical converters. The reader can refer to the reviews cited as reference [3,4] for a broaden overview of the electronic devices based on 2D-MoS_2. Among the devices based on 2D-MoS_2 that gathered attention, photodetectors have been considered and different device architectures have been reported, including photoconductors, photodiodes and phototransistors.

Photodetectors based on 2D-MoS_2 showed high performance in terms of response to light in the visible (VIS) spectrum and strategies to sensitize the response also in the near ultraviolet (NUV) and near infrared (NIR) spectrum have been demonstrated [5,6].

This has been accompanied by the development of different fabrication methods for 2D-MoS_2, including exfoliation techniques, chemical vapor deposition (CVD) as well as wet chemical synthesis.

The breakthrough for this material to move into actual applications would be to develop a facile manufacturing method, which is reproducible, versatile and scalable for large productions. Although exfoliation remains the simplest method to obtain mono- to few-layer MoS_2 and it is still used to demonstrate material properties and applications, other fabrication methods are needed to overcome the intrinsic limitations of exfoliation, that are mainly related to the scalability and reproducibility of the process. This resulted in the development of more scalable fabrication techniques, such as chemical vapor deposition (CVD), as well as wet chemical synthesis, leading to the fabrication of 2D-MoS_2 structures, such as monolayers, multilayers, and thin films. Though these approaches have proven to be suitable for the production of MoS_2-based photodetectors [6], providing good quality of the MoS_2 crystals, they have limited versatility due to the use high temperature processes (700-1000°C), which excludes the use of technologically relevant substrates (e.g. glass, PET, Kapton). Also, the processes often involve toxic compounds at a certain stage, requiring disposal of the toxic byproducts. Moreover, it is still challenging obtain MoS_2 large areas, limiting the scalability of the process.

A significant question that needs to be addressed regarding the manufacturing of MoS_2 is therefore:

Q1. Is it possible to fabricate large area 2D-MoS_2 via a facile, versatile, and scalable process, that can be used to produce photodetectors?

A possible solution was suggested by Nardi et al.[7] in 2018 with the introduction of a facile aqueous sol-gel process to produce MoS_2 thin films. However, the fabrication method was not optimized to produce large area and uniform MoS_2 films and never tested in photodetectors, leaving the doubt on the feasibility of the method to be exploited in applications.

A second important observation about 2D-MoS_2 based photodetectors is that the majority of works limits their use to the detection of light in the NUV-VIS-NIR spectrum. Potentially, 2D-MoS_2 possesses attractive properties for the direct detection of ionizing radiations (e.g. X-rays, γ-rays), such as high atomic number Z and good carrier mobility. Interestingly, its use as an absorption layer in a radiation detector has never been proven. An important use of radiation detectors is in radiation dosimetry

applications, i.e., determination of the dose released in media by ionizing radiation. This is of particular importance in the field of radioprotection to assess and prevent unwanted excess doses. One limitation of dosimetry is the need for radiation detectors that can monitor in real-time radiation quantities on the target during the irradiation of the target itself. This because the current detectors often present cumbersome structures, preventing their use in line with radiation beams without causing field perturbations. Such measurements will be of help when the irradiated target is a living patient, e.g., during radiotherapeutic irradiations or diagnostic exams. This branch of dosimetry is called *in-vivo* dosimetry. 2D materials can represent a solution to the problem, thanks to their low thickness leading to reduced beam attenuation. Organic, inorganic and hybrid materials have been studied for the purpose [8], albeit further research on materials is needed to move to actual devices.
A second point about MoS_2-based applications that is worth discussing is therefore:

Q2. Can 2D-MoS_2 be used as a direct radiation detection material, and can it be considered as an alternative for in-vivo dosimetry applications?

The aim of this thesis is to address the two questions mentioned above through a series of experiments and analyses that were performed in the doctoral project.

The doctoral project condensed in this doctoral thesis was carried out in the framework of the department of Excellence 2018-2022 (DII-UNITN)-Italian Ministry of University and Research (MIUR). The work was performed under the supervision of Prof. Lucio Pancheri, associate professor at the Industrial Engineering Department of the University of Trento, expert in modeling, fabrication and experimental characterization of detectors for electromagnetic radiation and particles. The doctoral project is also the result of the synergistic collaboration and shared knowledge between the Industrial Engineering Department of the University of Trento and the IRIS Adlershof center at the Humboldt university of Berlin, where Prof. Emil List-Kratochvil leads research on hybrid material and related devices, including TMDC for fabrication of transistors, detectors and neuromorphic applications.

Question Q1 will be addressed in Chapter 2, where an approach based on wet chemical synthesis will be presented. Based on the recipe first developed by Nardi et al. [7], a versatile and scalable method to produce large area MoS_2 thin films will be described. The method was exploited to produce a photodetector, to demonstrate a possible application in the field of optoelectronics.

An answer to question Q2 will be instead provided in Chapter 3, in which a more established fabrication technique was adopted to demonstrate the application of MoS_2 in the field radiation detection. A detector based on exfoliated MoS_2 monolayer (1L-MoS_2) was fabricated and characterized in a wide region of the electromagnetic spectrum.

The doctoral thesis is therefore articulated as follows:

1. The first chapter is structured in three sections and aims to give the reader the background and the framework of the doctoral project. The first section presents an overview of the state of the art of MoS_2 based photodetectors, describing material properties, fabrication strategies and presenting several works that are reported in literature, comprising MoS_2-based photodetectors for the electromagnetic spectrum in the NUV-VIS-NIR spectral range. The chapter continues with a second section regarding ionizing radiation detection and to the most common radiation detectors. The section continues reviewing the state of the art of detectors employing organic and hybrid materials for in-vivo dosimetry, which is the subject of the application described in chapter 3 in the case of a MoS_2 based X-ray detector. A significant part of the literature research that stands behind the first chapter was the basis of a review that I recently published on Sensors, MDPI, as a review article entitled *MoS_2 Based Photodetectors: A Review.*[6]

2. With chapter 2 we begin to describe the experimental work performed during the doctoral project. The chapter presents the development of a wet chemical synthesis exploiting a facile sol-gel route to fabricate MoS_2 thin films. The films are then characterized, and the results discussed. Afterwards, the use of the obtained films in a photodetector is demonstrated. Novelties and limits of the fabrication method are discussed, leaving room for future perspectives as a cue for future works, which are discussed in a dedicated section. This chapter is based and expand the results that I recently published on Optical materials, Elsevier, as an article entitled *Large area MoS_2 films fabricated via sol-gel used for photodetectors*.[9]

3. Chapter 3 describes the experimental work performed to demonstrate the use of 1L-MoS_2 as radiation detector material. This chapter initially describes the fabrication process of the detector which is based on an exfoliation approach.

The obtained detector is first characterized in the NUV-VIS-NIR spectral range to confirm the 1L-MoS_2 light conversion properties. The device is then characterized in the X-ray spectrum to demonstrate the use of the 1L-MoS_2 as radiation detector, showing its potential for in-vivo dosimetry applications. The results presented in this chapter have been recently submitted for publication in APL materials, AIP publishing, entitled *Demonstrating the high sensitivity of* *MoS_2 monolayers in direct X-ray detectors*, and the article is currently (01.07.2023) under review.

4. Chapter 4 presents the conclusion of the work, recalling the purpose of the conducted research and summarizing the main results. The chapter highlights the innovative aspects as well as the limits of the proposed strategies and aims to suggest the future research that may take inspiration from this work.

Chapter 1: Fundamentals and background

The aim of this chapter is to introduce the subjects of the study and to provide the reader with the framework of the project and the background needed to better understand the work. The section 1.1 introduces the properties of 2D-MoS_2 and of the technologies behind its fabrication. Also, it presents the basics of photodetection for 2D-MoS_2 in the NUV-VIS-NIR spectrum, and it recalls the state of the art of MoS_2-based photodetectors reported in the literature. The section is based and reports a review article entitled *MoS_2 Based Photodetectors: A Review* [6], that we published on the open access journal *Sensors, MDPI* in 2021. The full link to the article can be found at: Taffelli, A.; Dirè, S.; Quaranta, A.; Pancheri, L. MoS_2 Based Photodetectors: A Review. Sensors 2021, 21, 2758. https://doi.org/10.3390/s21082758.[6]
The second section focuses instead on detectors for ionizing radiation, introducing the basis of the X-ray detection and reporting the commercially available solutions. The section will then focus on the state of the art of X-ray detectors for in-vivo dosimetry which is the application investigated in Chapter 3 for 2D-MoS_2, where for the first time a device based on 1L-MoS_2 is demonstrated as direct X-ray detector.

1.1 MoS_2 properties and MoS_2 based photodetectors

Recent improvements in optoelectronics have been partly focused on the use of two-dimensional materials to produce photodetectors. The possibility of fabricating very thin optoelectronic devices, having high performance, low production costs and mechanical flexibility has been emerging in the last decade. Graphene was the first 2D material considered for photodetection applications, thanks to its outstanding electrical properties, in particular its impressive planar mobility, reaching 200,000 cm^2 /(V s), that allows to build photodetectors with bandwidth up to 40 GHz [10,11]. However, one of its mayor limitations for its use as photodetector active layer is the absence of an energy band gap, leading to high noise contribution to the signal, arising from dark currents.

Therefore, the investigation of 2D materials with finite bandgap has increased in recent years and transition metal dichalcogenides (TMDCs) have aroused more and more interest in the scientific community. Despite the modest mobility reported for these materials, which can reach about 200 cm^2 /(V s) [2], TMDCs possess interesting electro-optical properties. A transition from indirect to direct bandgap has been observed in TMDCs by reducing the dimensions from the bulk material to the monolayer limit [12]. Moreover, a strong light–matter interaction is observed for TMDCs, due to the direct band gap and to the strong excitonic nature of their low dimensional structures. For TMDCs, absorbance values that are one order of

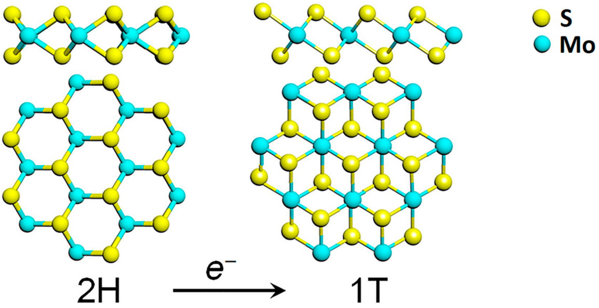

Figure 1: Transformation of the hexagonal 2H polymorph of MoS_2 into its 1T phase, through electron transfer. Reprinted with permission from ref [17]. © 2017 AIP Publishing.

magnitude higher than Si and GaAs are reported [13], thus providing strong light absorption with a very thin layer of the photoactive material. These features, combined with a higher mechanical flexibility of TMDCs compared to their bulk structures, allow us to fabricate very thin photodetectors also based on flexible substrates, opening the possibility to realize flexible and wearable devices. Applications for such devices can be related to medicine, biosensing, optical communications and security.

1.1.1 MoS_2 properties

Due to the relative abundance of molybdenite in nature, among the TMDCs, molybdenum disulfide (MoS_2) attracted much interest in the last decade. MoS_2 belongs to the family of the group VI transition metal dichalcogenides, where a layer of transition metal atoms (Mo, W) is sandwiched between two layers of chalcogen atoms (S, Se, Te).

Each MoS_2 layer is stacked onto each other via weak van der Waals forces, building a hexagonal (2H) structure which possesses a semiconducting behavior (Figure 1, left side). Another metastable phase of MoS_2 is known, with a tetragonal (1T) structure (Figure 1, right side). The 1T phase of MoS_2 is not stable at room temperature [14], but it can be induced by several processes such as chemical treatment [15], plasmonic hot electron transfer [16], electron beam irradiation [17,18], through charge transfer in the MoS_2 lattice. A subsequent annealing process is then required to restore the 2H-MoS_2 phase [9].

Bulk TMDC electronic properties are dominated by indirect transition from the maxi mum of the valence band, located at the Γ point of the Brillouin zone, and the minimum of the conduction band [19–21]. For MoS_2, the bulk electronic structure is characterized by an indirect energy band gap of about 1.2 eV. As for other group VI TMDCs, at the monolayer limit MoS_2 modifies its energy band structure towards a direct electronic transition from the K and K' points of the Brillouin zone, reaching an energy band gap of 1.8 eV [22,23]. This behavior can be explained by an increase in the indirect band gap due to a considerable quantum confinement effect in the out-of-plane direction when the dimensions of the material are reduced to few layers. On the other hand, the direct transition remains unaffected, becoming the minimum energetic band-to-band transition. This is well depicted in Figure 2 (top), where the evolution of the energetic band structure for MoS_2 is represented when moving from the bulk to the monolayer limit. Moreover, TMDCs are reported to have strong spin-orbit coupling (SOC), associated with the d-orbitals of transition metals [17,24,25]. The spin-orbit coupling breaks the degeneracy in the valence band, leading to two energetic maxima located at the K and K' points, separated by an energy splitting of 160 meV for a MoS_2 monolayer [16]. Figure 2 (bottom) shows the separation of the valence band maximum at the K point of the Brillouin zone, due to the degeneracy break. This property has been considered for applications in the experimental area of valleytronics [26,27].

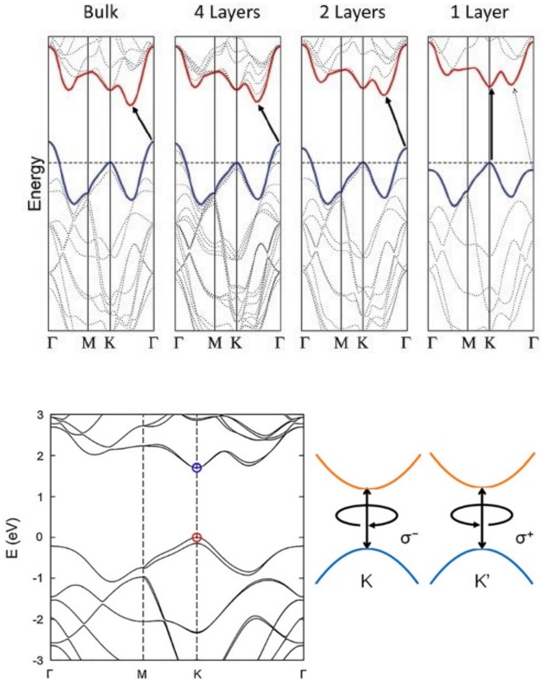

Figure 2: Energetic band structure of MoS_2. Top: transition from indirect to direct band gap moving from the bulk MoS_2 to the single layer of MoS_2. Reprinted with permission from ref. [20]. © 2010, American Chemical Society. Bottom: degeneracy at the K point in the valence band of a single MoS_2 layer. Reprinted with permission from ref. [14]. © 2017, AIP Publishing.

When MoS_2 is irradiated with photon energies larger than its bandgap, photons are absorbed and electrons are promoted to the conduction band, leaving holes in the valence band. The optical absorption of visible light by MoS_2 in the monolayer limit is dominated by the direct transition from the K and K' points of the valence band. However, light absorption experiments show also peculiar resonant features in mono- and few- layer MoS_2, associated with the excitonic energies [12,23]. Excitons are quasi bound states between electrons and holes, that interact via Coulomb forces. In Figure 3, typical absorption spectra of MoS_2, increasing the number of layers, are reported. The absorption peaks at specific energies (E_A = 1.88 eV, E_B = 2.03 eV in the monolayer limit) represent the excitonic energies of MoS_2. The relative positions of the A and B peaks are related both to an increase in the spin-orbit coupling and to an increase in the bandgap [28], approaching the bulk structure of MoS_2.

The strong light–matter interaction that characterizes MoS_2 is reflected in a high absorption coefficient that can reach about 10^6/cm [29], which is at least one order of

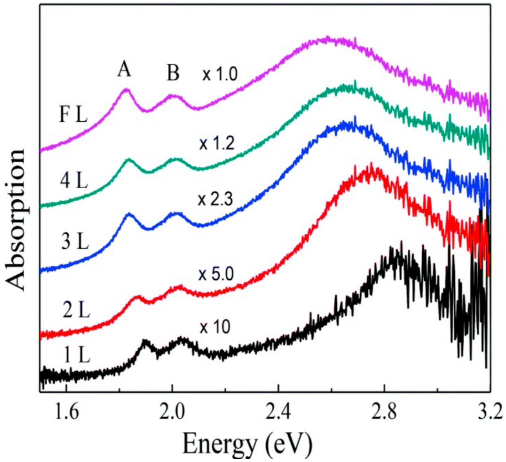

Figure 3: Absorption spectrum of MoS_2 varying the number of layers from 1 layer (1L) to few layers (FL), where A and B represent the excitonic peaks of MoS_2. Reprinted with permission from ref.[25]. 2014, Creative Commons Attribution 3.0 Unported Licence.

magnitude higher than standard semiconductors like Si and GaAs. Moreover, a single MoS_2 layer is reported to absorb up to 10% of the sunlight [13]. This superior light absorption makes MoS_2 suitable to build photodetectors based on very thin layers of material, still having high light conversion efficiency.

1.1.2 MoS_2 fabrication methods

To exploit the potentials of the MoS_2 properties mentioned above, research focused on the development of electronic devices based on 2D-MoS_2. Since Radisavljevic et al. [2] demonstrated the possibility to obtain transistors based on MoS_2 monolayers (1L-MoS_2) via mechanical exfoliation, significant amount of work has been published, demonstrating various devices such as transistors, photodetectors, LEDs, solar cells, hydrogen evolution reactors and photoelectrochemical converters [3,4]. Among these, development of photodetectors aroused great interest due to the exceptional light absorption of MoS_2, combined with its good charge carrier transport properties. Also, the superior light absorption makes possible to build photodetectors based on thin layers of MoS_2, still maintaining high light conversion efficiency and opening the way to develop ultrathin and flexible detectors. Accordingly, fabrication of thin MoS_2 structures became a central step of the device production and several strategies have been explored.

Exfoliation have been adopted in many studies [30-43], thanks to its simplicity and to the high-quality of the obtained crystals. In fact, due to the weak van der Waals interactions between MoS_2 layers, it is possible to obtain highly crystalline mono- or few-layered structures by a simple exfoliation of bulk MoS_2 with the help a scotch tape [44]. The MoS_2 layers need then to be transferred on a substrate to build a device. The method is generally versatile since it involves low temperatures. Although this method produces 2D crystals with superior quality, exfoliation suffers from low scalability of the process for large production and limited reproducibility of the crystal sizes [45]. Moreover, the dimensions of the exfoliated crystals are generally small (lateral size < 10 μm) [46], complicating the device fabrication process. Recently Heyl et al. reported thermally activated gold or silver assisted exfoliation method to produce large MoS_2 monolayers (82 mm^2), also demonstrating an effective method to transfer the large area monolayers on several substrates to build devices [47–49].

Bottom-up approaches are generally more scalable and reproducible processes that can be used to produce MoS_2. Chemical vapor deposition (CVD) is the method most compatible with the existing semiconductor technology and it is possible to deposit MoS_2 directly on wafer scale substrates [50]. To fabricate MoS_2 layers, precursor reagents such as Mo, $(NH_4)_2MoS_4$, or MoO_3, are deposited on supports as thin layers prior to the sulfurization at high temperature to favor MoS_2 formation and crystallization [4]. The process leads to mono to few layer MoS_2 flakes, though it is difficult to obtain a precise control of the number of layers, affecting the reproducibility of the process. Also, the interconnection of the flakes into a continuous film strongly depends on the temperature involved and on the atmosphere conditions [51]. Moreover, the flakes have micrometric lateral size affecting the electrical properties of the film, even though few reports indicate the possibility to obtain flakes larger than 500 μm [52–54]. Although the process is more scalable and controllable than exfoliation, CVD requires high temperatures (700–1000 °C), making the process less affordable and not suitable for direct deposition on flexible substrates. Finally, as a result of the sulfurization process, toxic byproducts such as H_2S are produced, that require proper disposal. As an alternative to standard CVD, plasma-enhanced CVD (PECVD) has been explored in order to reduce the temperature needed for the reaction (150–300° C), allowing film deposition also on plastic substrates [55].

Wet chemical syntheses have been considered lately as an alternative to the exfoliation and CVD methods, since they represent a facile, cheap and scalable method to fabricate MoS_2 thin films. The films can be obtained through hydrothermal [56] and solvothermal [57] synthesis. The syntheses are based on organic sulfur sources, generally thiourea or thioacetamide that react with ammonium salts and the solution is simply deposited on the substrate via spin- or dip-coating. This allows deposition on large area substrates (cm^2 size) and makes the process versatile for different substrate scalable for large production. Nevertheless, the material requires a thermal annealing step at temperatures (500–800°C) often combined with additional sulphurization, to convert the material and to enhance crystallinity, which limits the choice of the substrates, and requires toxic byproducts disposal. Nardi et al. [7] developed an aqueous sol-gel route al low temperature (60°C) to produce MoS_2 on different substrates, with low annealing temperatures (400°C) that promised to be suitable also for flexible devices. Solution processes gain in scalability and cost-effectiveness compared to other methods, though further studies need to produce superior crystal quality to compete with CVD or exfoliation methods.

From an electronic point of view,these MoS_2 production methods generally lead to n-type behavior of MoS_2. The n-type character of pristine MoS_2 is commonly associated to the electron donor nature of the sulfur vacancies [58]. The electronic character becomes particularly important when heterostructures between MoS_2 and other materials are built and a control of the MoS_2 doping might become critical. Doping control has been reported for MoS_2 and it can be achieved via substitutional doping [58–62] and surface doping methods [17,63].

1.1.3 MoS_2 based photodetectors

As stated above, one of the technological applications of MoS_2 layers that gain enormous interest in the last decade is photodetection. In fact, the possibility to fabricate very ultra-thin layers of MoS_2, with exceptional light absorption, combined with good mobility values, led to the production of a multitude of detectors that are reported in the literature. Aim of this section summarizes the different photodetector structures based on MoS_2 presented so far.

Figures of merit of photodetectors

In order to describe the photodetectors based on MoS_2 and compare their performance levels, it is advantageous to introduce some figures of merit that will be recalled in the following. The main figures of merit that are reported in the scientific literature relating to photodetectors, are defined below:

Responsivity (R): is the measure of how much photocurrent is generated in a detector per unit incident light power and it is measured in A/W. Responsivity generally depends on the wavelength of the incident light, due to different conversion efficiencies of the detectors to different lights, and it is also a function of the applied voltage bias.

External quantum efficiency (EQE): describes the photon-to-charge conversion efficiency of the detector, giving the ratio of the electron-hole pairs collected by the detector divided by the number of photons at a given energy shining on the detector.

On/Off ratio: represents the ratio between the current measured under illumination and the current measured in dark (dark or leakage current).

Detectivity (D): is the reciprocal of the noise-equivalent power (NEP), normalized per square root of the sensor's area and frequency bandwidth. It is measured in Jones (cm $Hz^{1/2}$ W^{-1})

Response time (τ_r and τ_d): refers to the time the detector needs to adapt to changes in the illumination power and, assuming an instant increase of light, rise time (τ_r) is defined as the time needed to move from 0% to 90% of the signal, while decay time (τ_d) is the time to drop from 100% to 10% of the signal, when the illumination power decreases.

In all photodetectors based on semiconductors, photons with energy larger than the material bandgap are absorbed and generate electron–hole pairs that can move under the action of an electric field. Devices may rely on different physical mechanisms for what concerns the charge drift and collection, giving rise to different photodetector categories. Most light detectors can be grouped into three classes: photoconductors, phototransistors and photodiodes.

In photoconductors, the radiation creates electron–hole (e–h) pairs, which are then separated by an external applied bias voltage (Figure 4) [64]. The charges drift towards the electrodes where they are collected, producing a photocurrent. The mechanism beneath the signal detection is the photoconduction, namely incident photons cause an increase in the charge density and thus in the conductivity of the material. Moreover, a mechanism called photoconductive gain can be exploited in photoconductors to enhance the signal level. The gain is defined as G = τ/t, where τ is the lifetime of one of the charge carriers (e.g., holes) and t is the transit time of

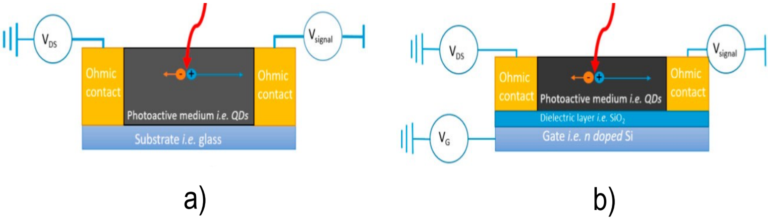

Figure 4: Photoconductor scheme (left) and phototransistor scheme (right). Adapted with permission from ref. [64]. Copyright 2020, Creative Commons Attribution 4.0 Unported Licence.

the opposite carriers (e.g., electrons). A gain arises when one of the charge carriers recirculate many times before it recombines with his opposite counter- part. Generally, energy states within the bandgap of the semiconductor, often induced by defects, are able to trap one of the two carriers, prolonging their lifetime and leading to multiple recirculation of the opposite carriers. The lifetime of the carriers strongly depends on the presence of trapping center within the material and can vary by several orders of magnitude, from few nanoseconds [30] to milliseconds [42]. In practice, trapping can be achieved by controlling the defects present in the material or by introducing sensitizing centers such as QDs or nanoparticles. Photoconductive gain affects the signal intensity but also its temporal response, which is governed by the carriers' lifetime. Generally, devices relying on the photoconductive gain reach very high values of responsivity, but present slower response and consequently a lower bandwidth compared to G=1 photoconductors. On the other hand, phototransistors are able to maximize the detector performance by reducing the noise rather than enhancing the signal intensity. In addition to the electrical contacts found in the photoconductors, here called “source” and “drain”, a third terminal (“gate”) electrically isolated from the semiconductor through a thin dielectric layer is present. Gate bias is generally exploited to deplete the semiconductor channel from carriers, in order to suppress dark current signals in the detector and thus maximize its signal-to-noise ratio (SNR). Moreover, the gate also modulates the mobility of the carriers, leading to high ON/OFF ratio values and higher values of the responsivity. Photoconductors and phototransistors unavoidably require an external power supply to sustain a voltage difference between the electrodes, which may become significant in large area detectors.

Photodiodes rely on the photovoltaic (PV) effect to collect charges. A built-in electric field is created at the junction between p- and n-sides of the semiconductor or by a Schottky barrier between a semiconductor and its metal contact. The built-in electric field can reach very high values in proximity of the junction, and thus the

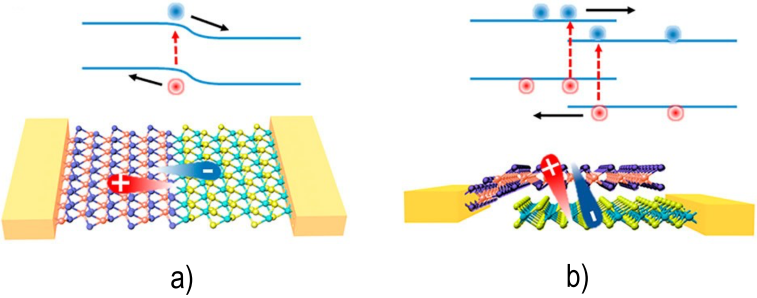
a)

b)

Figure 5: In-plane p–n junction (a) and out-of-plane p–n junction (b) of 2D materials, and their respective electronic band alignment. Reprinted with permission from ref.[14]. © 2017, AIP Publishing.

photogenerated carriers are driven to opposite contacts through an intrinsic voltage potential rather than an external power supply. Photodiodes can be composed of p–n junctions of the same material (homojunctions), of different materials (heterojunctions) or of metal–semiconductor junctions (Schottky diodes). Moreover, energy band alignment at the heterojunction can be exploited to suppress the drift of charges between the two sides of the junction, thus reducing the dark signals. Photodiodes can be arranged in a horizontal fashion, where two materials are put side by side (in-plane junctions), or vertically stacked, where they are put one on top of each other (out-of-plane junctions) (Figure 5). In the following we will discuss a selection of photodetectors based on MoS_2 reported in the literature, chosen from among the most meaningful ones.

Neat MoS_2-based photoconductors are the simplest photodetectors that will be discussed in this review. They are generally composed of an insulating substrate material (e.g., SiO_2, Al_2O_3, Si_3N_4) over which MoS_2 is deposited. The metal contacts can be created directly on the substrate or can be deposited on the MoS_2 surface by physical vapor deposition methods. The metal contacts can be designed properly to maximize the response and the speed of the device, as in the case of interdigitated finger contacts.

Gonzalez Marin et al. [34] fabricated a phototransistor, based on a mechanically exfoliated MoS_2 monolayer deposited on a Si/SiO_2 substrate, which reached a large photoresponsivity ($R = 10^3$ A/W) in the visible range. However, such a high response was obtained via a large photogain mechanism, arising from a very long carrier lifetime, which resulted in a response time of 13 s. Their device was also implemented into a nanophotonic circuit to test its applicability in nanophotonics (Figure 6). In fact, a single MoS_2 layer was successfully applied over a waveguide to detect the waveguide losses. A significantly faster device was produced by Tsai et al. [65], based on a few-layeredMoS_2 structure obtained through a wet-synthesis approach, and deposited on a Si/SiO_2 substrate. The Au electrodes were fabricated by photolithography in an interdigitated fashion (Figure 7) to produce a metal–semiconductor–metal (MSM) Schottky photodiode. The detector showed very fast response to visible light (t_rise = 70 μs, t_fall = 110 μs) and a responsivity of R = 0.57 A/W. The reason for this performance is the good compromise between modest photogain and smart geometry of the device which speeds up the carrier collection. In fact, Au electrodes produced via photolitograpy in an interdigitated fashion with 8 μm finger spacing (Figure 7b), play an important role in diminishing the time needed to collect the carriers. Yore et al. [66] built an array of photodetectors based on MoS_2 monolayers through a CVD deposition process and achieved a response extending towards the ultraviolet spectral region (λ~400 nm). The devices exhibited a photoresponsivity of about 1 mA/W, with a fast response of ~ 0.5 ms. Moreover, the detectors exhibited an extremely low dark current, $I_d \leq 10$ fA, attributable both to a bipolar Schottky barrier between the MoS_2

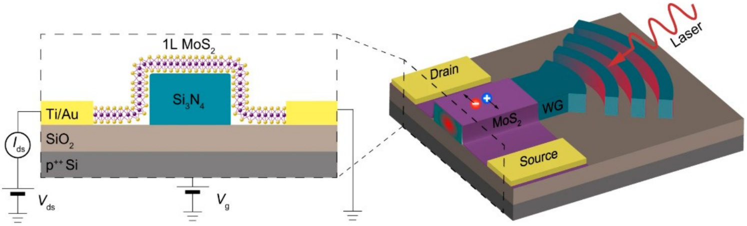

Figure 6: Scheme of a phototransistor and its implementation in a nanophotonic device. Reprinted with permission from ref. [34]. © 2019, Springer Nature.

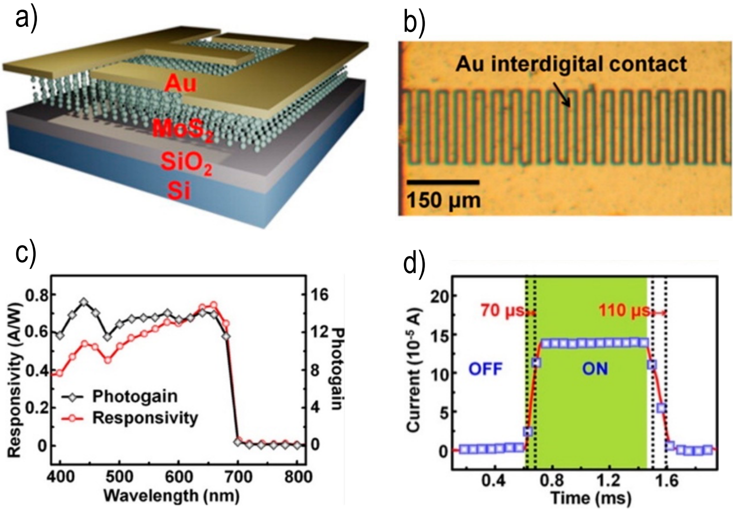

Figure 7: (a) Scheme of a photoconductor based on MoS_2; (b) optical microscope top view of the device, where Au interdigitated contacts are clearly visible; (c) responsivity and photogain for the device over the NUV-IR spectral range; (d) photoswitching time response of the detector. Reprinted with permission from ref. [65] . © 2013, American Chemical Society.

and the metal contacts, and to a negligible doping of the sample from charge impurities introduced by the substrate through an efficient deposition process. Lopez-Sanchez et al. [31] developed one of the first phototransistors based on MoS_2, obtained through a mechanically exfoliated single layer deposited on a Si/SiO_2 substrate. The device showed a responsivity of 880 A/W in the visible range, attributable also to a strong photogain mechanism, which also affected the photoswitching time of the detector, which was about 9 s. They reported a very low value of the dark current, $I_d = 2$ pA, although it was achieved with a strong negative bias of the gate, $V_g = 70$ V. A similar device was fabricated by A.R. Klots et al. [36] with faster response, in the order of 1 ms. The light response, although it was lower, reached 50 A/W, due to a photogain contribution of 10^3 times. Another low-noise device is described in [30], where a multilayer MoS_2 structure obtained through mechanical exfoliation was deposited on Al_2O_3 (Figure 8). The detector exhibited

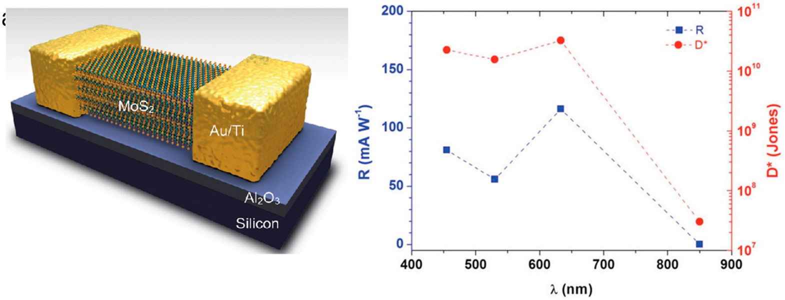

a)

b)

Figure 8: (a) Scheme of a phototransistor based on MoS$_2$. (b) Responsivity and detectivity of the phototransistor over the visible-NIR spectral range. Reprinted with permission from ref. [30]. © 2012, John Wiley and Sons.

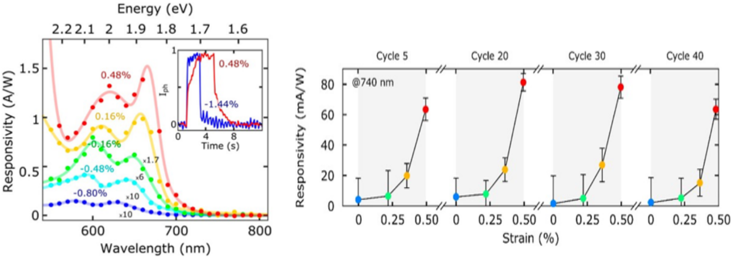

a)

b)

Figure 9: a) Responsivity values over the spectral range for a single layer MoS$_2$-based device when subject to various strains. In the inset the temporal response for different strain applications is shown. (b) Responsivity values against the applied strain increasing the bending cycle number. Reprinted with permission from ref. [33]. © 2019, Elsevier

in the visible region, which dropped to very low values for near infrared radiation, attributable to the weak absorption in the IR spectral region. The detector responsivity was also affected by a short carrier lifetime τ, which was determined to be 1.27 ns, limiting the photogain mechanism. Finally, the measured dark currents were as low as 10^{-11} A. The good response, combined with the very low noise contribution of the system, led to a good detectivity of the device that reached 10^{11} Jones in the visible region. Moreover, low dark currents were achieved with a low bias of the gate terminal (Vg = −3 V).

Gant et al. [33] demonstrated a strain tunable photodetector based on a single MoS_2 layer structure, obtained by mechanical exfoliation. Their device displayed two to three orders of magnitude of variation in the responsivity when subjected to a strain in the visible range (Figure 9a). The applied strain also caused a variation of the time response from 80 ms to 1.5 s. The variation of both magnitude and time response can be attributed to the creation of trap states in the material during strain. Moreover, the measurements showed a good reproducibility when the device was tested under multiple bending cycles, demonstrating the stability of the material under strain (Figure 9b).

Neat MoS_2 photoconductors can reach large values of responsivity when a sufficient voltage bias is applied, attributable to a large photogain contribution and can achieve relatively fast response times if the detector geometry is designed properly (e.g., with interdigitated electrodes). Most of the neat MoS_2 photodetectors are characterized in the visible range (400–700 nm) and only very few devices explore the response to the near ultraviolet (NUV) or near infrared (NIR) spectrum (Figure 10). The IR spectrum generally leads to limited response of the material, since the absorption edge of MoS_2 lays in the red (~ 660 nm) which act as a cutoff for the longer wavelength radiation. On the contrary, the UV response is expected to increase when decreasing the wavelength, as suggested by absorption experiments. To overcome limitations of MoS_2 photodetectors for what concerns with spectral range and response time, MoS_2 have been combined with quantum dots (QDs) or nanoparticles (NPs), or heterostructures between MoS_2 and other TMDCs have been fabricated. In the following some relevant examples of these types of detectors are reported.

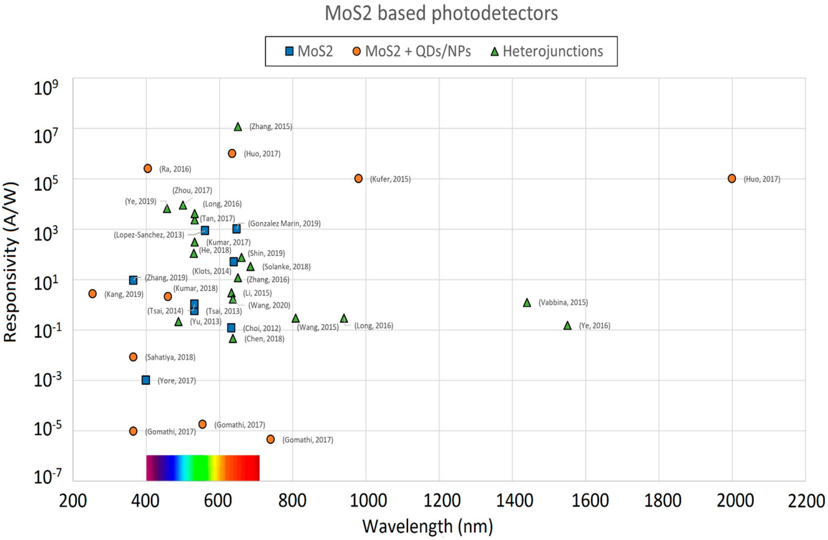

Figure 10: Responsivity values plotted against the wavelength for various MoS_2-based photodetectors.

A CdSe sensitized MoS_2 phototransistor is reported in [41], based on an exfoliated MoS_2 bilayer over a Si/SiO_2 substrate (Figure 11). The device showed a responsivity of 2.5×10^5 A/W at 405 nm of incident light, which is the highest light response of a MoS_2-based photodetector in the NUV spectral range to the best of our knowledge. Although the responsivity reached very high values, the time response remained as small as 60 ms. The reasons for such performance have to be attributed to the n–n heterojunction formed by the MoS_2 bilayer and the CdSe nanocrystals as depicted in Figure 11(b). In fact, when the UV radiation hits the interface region, the electrons formed in the CdSe nanocrystals are driven to the MoS_2 side, while the holes remained confined in the CdSe nanoparticles. When the light was switched off, the electrons accumulated in the valley easily recombined and the n–n barrier prevented the transfer of carriers between the two regions. Some efforts have been done to reduce the required gate bias, as in MoS_2 phototransistor sensitized with HgTe nanoparticles reported by [42]. The detector (Figure 12) showed an extremely high responsivity (10^5–10^6 A/W) over a very broad light spectrum,

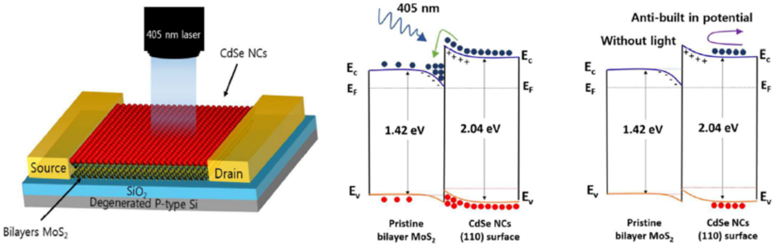

a) b)

Figure 11: (a) Structure of a phototransistor sensitized with CdSe nanoparticles. (b) Band alignment between MoS_2 andCdSe nanoparticles and their carrier representation when light in ON or OFF. Reprinted with permission from ref. [41]. ©2009, Royal Society of Chemistry.

ranging from visible to mid infrared (2000 nm), with a fast response time in the order of milliseconds. Such high responsivity was achieved through a high photogain mechanism, originated from a large hole lifetime ($\tau = 4$ ms) induced by the presence of QDs, which was six orders of magnitude larger than the transit time of the electrons ($t = 9$ ns). The detectivity measurements showed values of about 10^{12} - 10^{13} Jones over the same spectral range, also due to the low measured value of the dark current (10 pA). In this device, a toxic element (Hg) is still present, but the detector was operated at a gate bias of 15 V in depletion regime, which is much lower than in previous devices. The gain in gate modulation can be attributed to the presence of a TiO_2 buffer layer that reduces the interaction between MoS_2 and HgTe. A more recent work [67] has explored the deep UV spectral region reporting a phototransistor based on a thin MoS_2 film deposited on a flexible PET substrate, sensitized with ZnO nanoparticles (Figure 13(a)). The device showed a remarkable responsivity of 2.7 A/W to a 254 nm UV light source. Moreover, the performance was stable under multiple bending cycles. However, the response was slow, reaching tens of seconds, and the bias voltage required to obtain such a high response was set to 40 V.

These results make clear that more efforts have to be undertaken to produce more efficient photodetectors, especially in the deep UV light region, to broaden the possible applications of MoS_2 at short photon wavelengths. Devices belonging to this category generally show high responsivity values also in regions outside the visible spectrum, due to increased absorption those wavelengths.

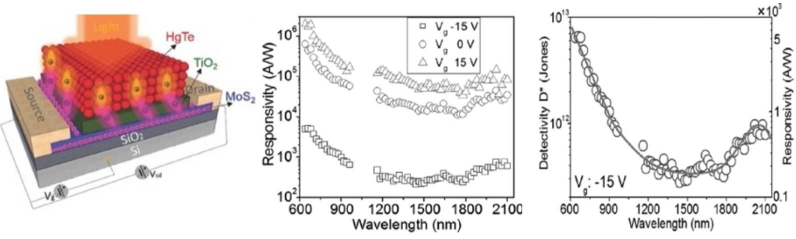

a) b) c)

Figure 12: (a) Photodetector based on MoS_2 + HgTe; (b,c): responsivity and detectivity values over the vis-IR spectral range, respectively, for the same phototransistor. Reprinted with permission from ref. [42]. © 2017, John Wiley and Sons.

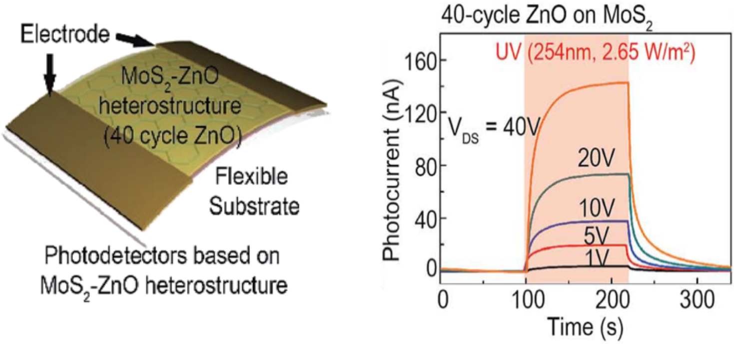

a) b)

Figure 13: (a) Scheme of a phototransistor based on a MoS_2-ZnO structure and developed on a flexible PET substrate; (b) response of the phototransistor to an incident UV (254 nm) light over time. Reprinted with permission from ref. [67]. Copyright 2019, Creative Commons Attribution 3.0 Unported Licence.

Several studies have reported photodetectors based on heterostructures composed by different TMDCs. In these devices, the different electronic band structure forms a built-in electric field at the interface between the materials that speeds up the photogenerated carrier separation. Moreover, the spectral range response of these photodetectors is widened since it involves different semiconductor materials. Chen et al. [43] proposed a photodiode based on a vertical van der Waals heterojunction between MoS_2 and $MoTe_2$, obtained through mechanical exfoliation (Figure 14). With respect to MoS_2, $MoTe_2$ presents a smaller bandgap, which varies from 0.9 to 1.1 eV moving from bulk structure to monolayer. The structure exploits a type II band alignment, which favors the injection of electrons into MoS_2 and the injection of holes into $MoTe_2$ (Figure 14(b)). The device displayed a responsivity of 0.046 A/W to a 637 nm light, with no voltage bias applied. Moreover, the authors measured a response time of about 60 μs, due to the fast separation of carriers that occurs at the junction. In fact, the space charge region near the junction is characterized by a very strong built-in electric field, which becomes stronger as the length of the junction is scaled down, as it happens for vertical heterojunctions. The strong interlayer built-in potential provided also a barrier for the dark current, which was measured to be about 3 pA. Long et al. [40] reported a phototransistor based on stacked MoS_2–Graphene–WSe_2 layers, obtained by mechanical exfoliation (Figure 15). This device was tested over a broadlight spectrum (400–2400 nm). The detector exhibited a responsivity up to 10^4 A/W in the visible region, which decayed to 300 mA/W approaching the IR region (940 nm), with no gate bias applied. The calculated specific detectivity was 10^{15} Jones in the visible region, while decayed to 10^{11} Jones in the IR region. Finally, the detector showed a time response to visible light of 54 μs, which indicates a fast response of the system, typical in a detector based on a vertical heterojunction. Many other MoS_2-based devices have been reported in the literature; the performance of a few other devices [37-39, 68-84], together with the photodetectors we have described so far,are reported in the graph of Figure 10 .

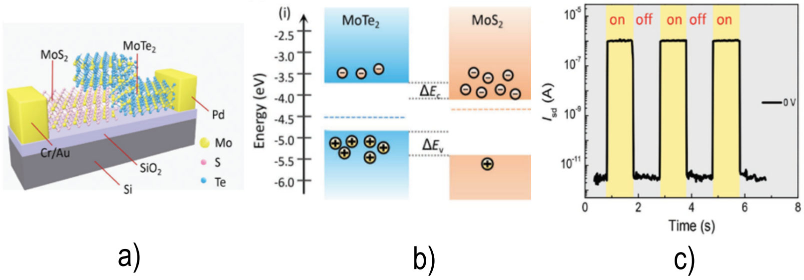

Figure 14: (a) Scheme of a photodetector based on an heterojunction between MoS_2 and $MoTe_2$. (b) Type II band alignment between $MoTe_2$ and MoS_2; (c) Photoswitching behaviour of the photodetector at V = 0 V. Reprinted with permission from ref. [43]. © 2018, John Wiley and Sons.

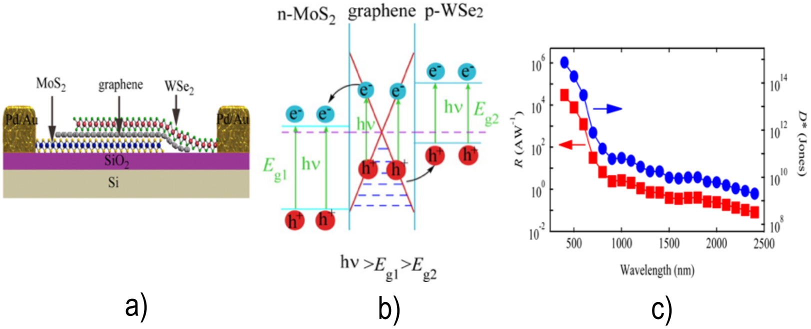

Figure 15: (a) Scheme of a phototransistor based on the vertical heterostructure between MoS_2, graphene and WSe_2. (a) Band alignment at the heterojunction between TMDCs and graphene; (c) responsivity and detectivity values plotted against the incident wavelength for the phototransistor over the vis-IR spectrum. Reprinted with permission from ref. [40]. © 2016, American Chemical Society.

Both the responsivity and the response time have been plotted in Figure 16 for several MoS_2-based photodetectors, in order to compare their performance. Since, through the photoconductive gain, the responsivity is directly proportional to the lifetime τ_r [10,70], a reference line representing the points for which $R/\tau_r = 1$ A/(W us) has also been included in the graph. As can be observed, only three devices are represented by a point above this line. In Long et al. [40] the separation of the carriers is performed by the built in electric field at the vertical junction between the TMDCs, while the transport is performed laterally by graphene, resulting in the best combination for fast carrier transport. Otherwise, devices where TMDCs are responsible both for the separation of carriers and for the carrier transport may suffer from a slower response. Building heterojunctions with TMDCs is a valuable solution to increase device performance, in terms of response time and spectral range with respect to neat MoS_2 photodetectors. However, the spectral range of the detector is still limited by the bandgaps of the TMDCs involved. On the other hand, MoS_2-based photodetectors sensitized with QDs or NPs described in Ra et al. [41] and Huo et al. [42], despite their slower response compared to heterojunction based structures, reached high performance due to an efficient carrier transfer and a remarkable photogain. Many photodetectors based on MoS_2 have been developed in the last decade, and the most representative have been analyzed in this review. The main characteristics of the devices discussed so far are summarized in Table 1.

Photoconductors based on MoS_2 are the simplest structure of photodetectors and they are able to reach very high responsivity values. On the contrary they generally suffer from slow response, due to absence of a built-in electric field, and from high dark currents that limit the sensitivity of the device. Phototransistors based on MoS_2 represent a more mature architecture for detecting light, due to the possibility to suppress dark current signals with an appropriate voltage bias applied at the gate terminal. Although so far very few works report the response of the MoS_2 device to the UV and IR spectral regions, they clearly show that there is room for improvement if this material is coupled with other TMDCs, graphene or quantum dots. These properties, combined with the thin structures of MoS_2 that can be fabricated, allow us to build wide-spectrum bendable detectors.

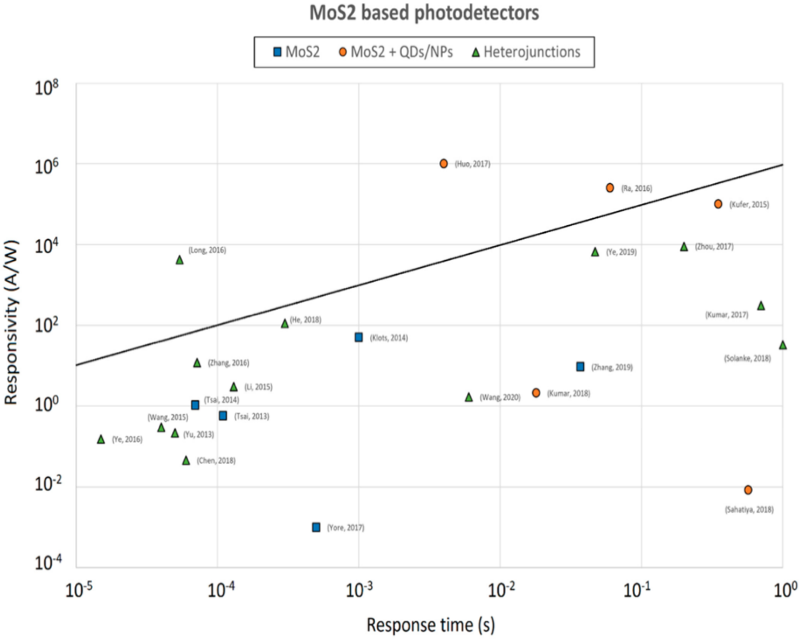

Figure 16: Responsivity values plotted against the response time for various MoS2-based photodetectors. The solid line represents the points for which R/τ_r = 1 A / (W μs).

In this direction, devices based on MoS_2 sensitized with NPs or QDs are able to boost the response of the detectors both in the NIR-MIR and in the NUV spectrum, and are often characterized by very high responsivity values. However, the defects induced on MoS_2 in consequence of the introduction of sensitizing centers, cause large dark current and slow response.

Heterostructures between MoS_2 and other materials (e.g., TMDCs and graphene) are able to extend the response to a wider spectral range as well, and have been demonstrated to be suitable for the fabrication of fast photodiodes, exploiting the built-in electric field that forms at the heterointerface. Moreover, these devices are able to work also at zero-bias mode, without requiring an external power supply. The main drawback for photodiodes is instead represented by the lower responsivity that they can reach, due to the absence of the photogain mechanism.

Table 1: MoS_2 -based photodetector performance. FL = few layers, ML = multilayer, TF = thin film, t_r = rise time, t_d = decay time.

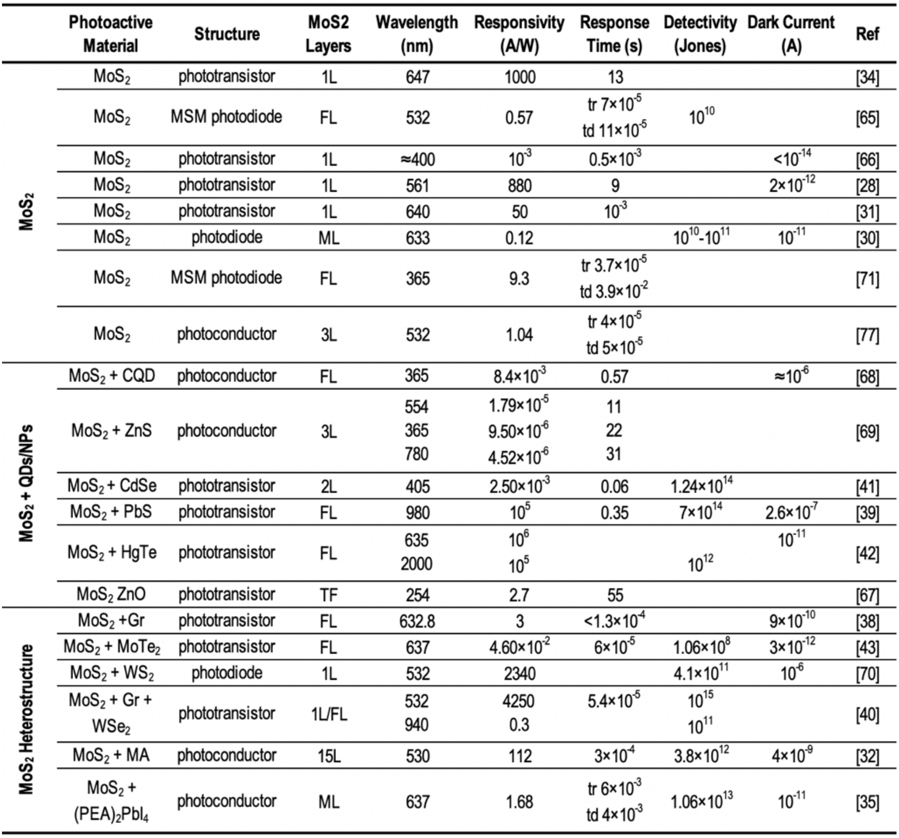

	Photoactive Material	Structure	MoS2 Layers	Wavelength (nm)	Responsivity (A/W)	Response Time (s)	Detectivity (Jones)	Dark Current (A)	Ref
MoS_2	MoS_2	phototransistor	1L	647	1000	13			[34]
	MoS_2	MSM photodiode	FL	532	0.57	tr 7×10^{-5} td 11×10^{-5}	10^{10}		[65]
	MoS_2	phototransistor	1L	≈400	10^{-3}	0.5×10^{-3}		$<10^{-14}$	[66]
	MoS_2	phototransistor	1L	561	880	9		2×10^{-12}	[28]
	MoS_2	phototransistor	1L	640	50	10^{-3}			[31]
	MoS_2	photodiode	ML	633	0.12		10^{10}-10^{11}	10^{-11}	[30]
	MoS_2	MSM photodiode	FL	365	9.3	tr 3.7×10^{-5} td 3.9×10^{-2}			[71]
	MoS_2	photoconductor	3L	532	1.04	tr 4×10^{-5} td 5×10^{-5}			[77]
MoS_2 + QDs/NPs	MoS_2 + CQD	photoconductor	FL	365	8.4×10^{-3}	0.57		$\approx10^{-6}$	[68]
	MoS_2 + ZnS	photoconductor	3L	554 365 780	1.79×10^{-5} 9.50×10^{-6} 4.52×10^{-6}	11 22 31			[69]
	MoS_2 + CdSe	phototransistor	2L	405	2.50×10^{-3}	0.06	1.24×10^{14}		[41]
	MoS_2 + PbS	phototransistor	FL	980	10^{5}	0.35	7×10^{14}	2.6×10^{-7}	[39]
	MoS_2 + HgTe	phototransistor	FL	635 2000	10^{6} 10^{5}		10^{12}	10^{-11}	[42]
	MoS_2 ZnO	phototransistor	TF	254	2.7	55			[67]
MoS_2 Heterostructure	MoS_2 +Gr	phototransistor	FL	632.8	3	$<1.3\times10^{-4}$		9×10^{-10}	[38]
	MoS_2 + $MoTe_2$	phototransistor	FL	637	4.60×10^{-2}	6×10^{-5}	1.06×10^{8}	3×10^{-12}	[43]
	MoS_2 + WS_2	photodiode	1L	532	2340		4.1×10^{11}	10^{-6}	[70]
	MoS_2 + Gr + WSe_2	phototransistor	1L/FL	532 940	4250 0.3	5.4×10^{-5}	10^{15} 10^{11}		[40]
	MoS_2 + MA	photoconductor	15L	530	112	3×10^{-4}	3.8×10^{12}	4×10^{-9}	[32]
	MoS_2 + $(PEA)_2PbI_4$	photoconductor	ML	637	1.68	tr 6×10^{-3} td 4×10^{-3}	1.06×10^{13}	10^{-11}	[35]

Reused and adapted from the open access paper: Taffelli, A.; Dirè, S.; Quaranta, A.; Pancheri, L. MoS_2 Based Photodetectors: A Review. Sensors 2021, 21, 2758. https://doi.org/10.3390/s21082758.

1.2 Photodetectors for ionizing radiations

Ionizing radiation was discovered long ago, when in 1895 Röentgen observed a glow on a screen in the proximity of the Crookes tube he was working with, caused by rays not visible to the human eye, which he called X-rays. The medical implications of X-rays were immediately understood, when Röentgen, studying the penetrating ability of X-rays, produced a “radiography” of his wife’s hand that presented to the scientific community. Although the advantages of the discovery were immediately recognized, it took several years to acknowledge the negative effects of radiation on living tissues and materials. Today is clear that when dealing with X-rays, the photon energy may be sufficiently high to damage living tissues via cell killing, or to induce material degradation through the creation of defects in the lattice structure. Therefore, detection and monitoring of ionizing radiations has become a fundamental tool in several application, such as medical diagnostics and therapy, nuclear energy production, space exploration, radiation shielding, etc. Diverse devices have indeed been developed for the detection of ionizing radiations, e.g. radiochromic films, ionization chambers and semiconductor-based detectors to cite the most used ones. Nevertheless, there is still demand for materials that can be employed in wearable detectors for real-time monitoring of radiation in the field of in-vivo applications. Interestingly, although TMDCs have been vastly investigated as photodetectors for UV-VIS-NIR radiations (as described in the section above), they have never been considered for applications regarding the detection of ionizing radiation. The advantage of using TMDCs for ionizing radiation detection are diverse, and the reasons will become clear in the following section.

Below we will present an overview of the basics of the fundamental principles of X-ray detection. We will then present the main solutions available and currently under study for X-ray detection, highlighting their advantages and limits. A particular focus will be given to a specific application, namely in vivo dosimetry, which is the application that will be discussed in chapter 3 in the case of a MoS_2 based photodetector.

1.2.1 Interaction of radiation with matter

Radiation is defined as ionizing when its energy exceeds the ionization energy of the hydrogen atom (E = 13.8 eV). Ionizing radiations comprise not only photons, but also other radiation types able to ionize matter, such as charged particles, neutrons, etc. In this section we will mainly describe ionizing photons, which are the most widespread radiations used in applications and the type of radiation used in this work. Ionizing photons can be classified into two types: X-rays and γ-rays, and their difference lies in the process involved in their production. X-rays are produced via the collision of accelerated electrons on a metal anode in a high-voltage vacuum tube, while γ-rays are the product of atomic nuclei decay (see subsection below).

The physical processes X- or γ-ray photons undergo when they interact with matter result in the production of high energy electrons. The electrons are then thermalized via successive interactions in the material lattice, resulting in multiple charge carriers per incident photon. These types of interactions are mainly of three types: photoelectric absorption, Compton scattering and pair production. In the photoelectric absorption the incident photon is absorbed by an atomic electron (generally from a K- or innermost shell) which is emitted from the atom (Figure 17(a)). In the detection process, the generated photoelectrons lose energy via multiple electron-lattice collisions, and they are eventually collected. In Compton scattering the incident photon is scattered by an outer shell atomic electron. In this process part of the energy of the photon is transferred to the electron. The electron is easily absorbed in the material with the same process described above for the photoelectron, but the scattered photon might escape the detector, not contributing to the signal. Finally, In the pair production process the incident photons interact with the atomic nuclei and can be converted into an e^-/e^+ (electron/positron) couple. The phenomenon occurs only for photon energies larger than 1.022 MeV (sum of the energies of electron and positron at rest), and thus is not considered for low energy applications. The electron is easily absorbed in the detector, while the positron undergo annihilation with an electron via emission of two photons at 511 keV. Unless the photons are reabsorbed, a fraction of the initial photon energy does not contribute to the signal.

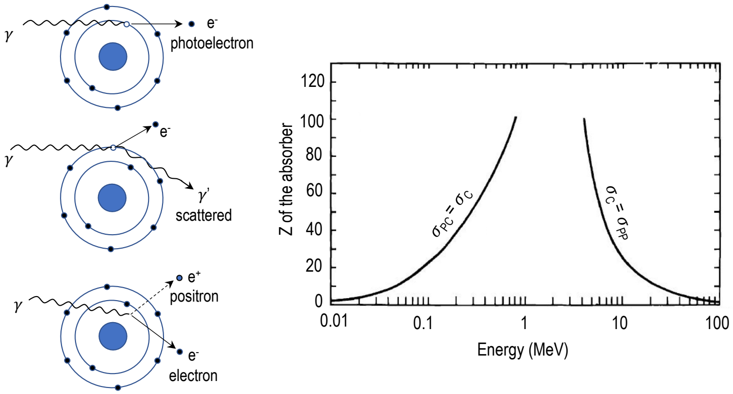

a) b)

Figure 17: (a) ionizing photons interaction with matter with production of electrons. (b) comparison of the cross-section of the X-ray interaction processes varying Z of the absorber and energy of the photon.

The total interaction cross section can thus be written as the sum of these different processes:

$$\sigma_{\mathrm{TOT}} = \sigma_{\mathrm{PE}} + \sigma_{\mathrm{C}} + \sigma_{\mathrm{PP}}$$

Where PE = photoelectric effect, C = Compton and PP = pair production. Figure 17(b) shows the contribution of the cross section of these processes depending on the radiation energy and on the atomic number Z of the absorber. The photoelectric absorption occurs predominantly for photons at energies below few hundred of keV. Photoelectric cross section increases rapidly increasing the Z of the absorber ($\sigma_{PE} \sim Z^5$). This favors high Z materials (e.g. metals) in detectors, since they have higher detection efficiency and lead to significant absorption in relatively small detector volumes. Compton scattering occurs instead in all the energy spectrum and becomes the dominant process for photons approaching energies of 1MeV. Ultimately, pair production becomes the predominant process at high energies (~10 MeV).
Macroscopically, these atomic interactions in the absorber lead to attenuation of the radiation beam that can be described by an attenuation law:

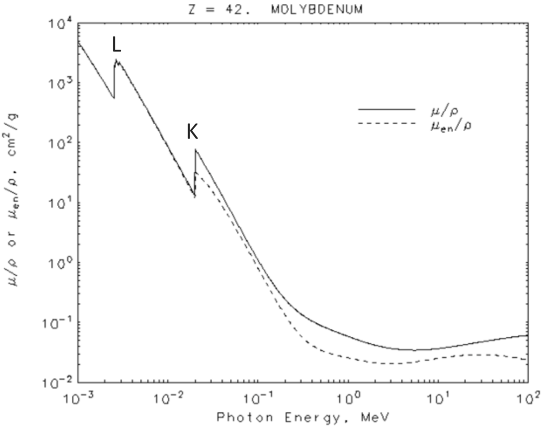

Figure 18: mass attenuation coefficient for a Mo absorber. The sharp edges are associated to the energies of the L and K electronic transitions [85]

$$I(x) = I_0\, e^{-(\mu/\rho)\cdot x}$$

Where I represents the photon flux in $cm^{-2} \cdot s^{-1}$, μ is the attenuation coefficient, ρ is the density of the absorber, and x is the absorber mass thickness (defined as the thickness t of the absorber multiplied by its density $x = \rho \cdot t$). The coefficient μ/ρ is called mass attenuation coefficient and it is generally calculated from experiments. The attenuation coefficient is related to the cross section of the photon interactions via the following equivalence:

$$\mu/\rho = \sigma_{TOT}/uA$$

Where u is the atomic mass unit and A is relative atomic mass of the absorber [85]. An example of how the mass attenuation coefficient varies varying the incident photon energy is reported in Figure 18 for an absorber made of molybdenum (Z=42). The sharp edges represent the characteristic edge absorption associated with the photoelectric emission of L- and K- shell electrons. When dealing with homogeneous compounds and mixtures, it is possible to calculate the absorption coefficient via the superposition of the single mass absorption coefficients:

$$\mu/\rho = \sum_i w_i(\mu/\rho)_i$$

where w_i is the fraction weight of the i^{th} component. Since the attenuation strongly depends on the atomic number Z, for mixture and compounds an effective atomic number Z_{eff} can defined [85] to qualitatively describe the different interaction of radiation with matter.

In the attenuation process, a fraction of the radiation energy is absorbed by the medium. Radiation dosimetry aims to determine how much energy is deposited by radiations in a medium. The energy deposited per unit mass is called absorbed dose (often referred as dose) and it is measured in Gray (1 Gy = 1 J/1 Kg). The dose depends on the material that is irradiated, due to the different attenuation coefficients. Therefore, to determine doses in a specific medium with detectors, a calibration that considers the different Z_{eff} of the detecting material with respect to the target medium is required [8].The interest of dosimetry is often the determination of the dose deposited in human tissues, and water is generally used as a reference measure due to the very similar effective atomic numbers (Z_{eff} = 7.4)[85].

1.2.2 Production of X-rays and γ-rays

In the fields of medical diagnostics and medical treatments as well as material characterization, the production of X-rays and γ -rays is of fundamental importance. X-rays are generally produced with an X-ray tube. An X-ray tube is a vacuum tube

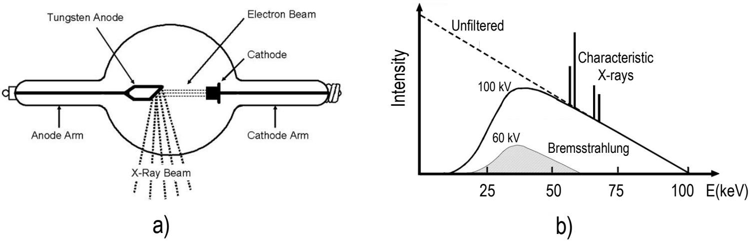

Figure 19: (a) scheme of an X-ray tube, showing the production of X-ray from the anode (target) [86] ; (b) typical X-ray spectra of a tungsten anode at 60 kV and 100 kV. Dashed line represents the spectrum obtained not considering the filtering of low energy X-rays.

where electrons are emitted by a hot filament (cathode) by thermal emission and accelerated thanks to an applied high voltage bias (10 – 10^2 kV) towards a target (anode), as depicted in Figure 19(a) [86] . When the electrons hit the anode, their deceleration is so intense that they emit X-rays. This process is called *bremsstrahlung* (i.e. braking) and the resulting radiation is called bremsstrahlung radiation. Due to the stochastic nature of the process, bremsstrahlung radiation has a continuous spectrum with a maximum energy which equals the maximum energy of the accelerated electrons (conservation of energy). The choice of the target plays then a crucial role in the production of radiation since it determines the shape of the resulting radiation spectrum. A typical X-ray radiation spectrum is shown in Figure 19(b) for an X-ray tube with a tungsten target. The spectrum is a superposition of a continuous bell-shaped line and characteristic X-ray peaks. The bell-shape of the spectrum is due to filtering of the lower energy X-rays, which is performed by the target itself or by additional filters applied at the tube exit (e.g. Cu, Al filters). The energy of the characteristic X-rays is determined by the choice of the target (e.g. for tungsten, $E_{k\alpha}$ (W) = 59 keV, for copper $E_{k\alpha}$ (Cu) = 8 keV). Characteristic X-rays are produced when an electron from an inner atomic shell is ejected due to photoelectric effect or due to collision with an incoming electron as in the X-ray tube. The electrons in the outer shell reorganize to fill the inner and more stable atomic shells, while the extra energy is released as X-rays. The energy of characteristic X-rays depends on the atomic configuration of the elements, which varies from atom to atom. The X-ray production process is very inefficient though, with electron to X-ray energy conversion of roughly 1%. Most of the energy used in the process is released as heat and requires a continuous cooling of the metal target.

γ-rays are instead the result of decay processes of atomic nuclei. Decays happen at specific energies, resulting in monochromatic radiation, ranging from few keV to several MeV. Moreover, nuclei decay is a stochastic process and, although it can be stimulated, makes γ-rays intrinsically less tunable than X-rays, and thus hard to exploit in applications where a certain amount of radiation is needed. Nevertheless, the detection of γ-rays is an important tool for several applications like nuclear medicine, astrophysics, nuclear physics, nuclear energy production and security.

1.2.3 X-rays detectors

To monitor unwanted radiation exposure or to guarantee reliable radiation delivery in medical treatments, the technology has provided many detector solutions that are commercially used as standards.

Radiochromic films are the most widely spread commercial product used to monitor ionizing radiation exposure [87] . The films contain a dye which is radiation sensitive and change color when irradiated [88]. These films show mechanical flexibility and exhibit tissue-equivalent response to radiation in a wide energy range. They are widely used as absolute dosimeters, since they can measure with good accuracy the total absorbed dose [89]. Nevertheless, they are not real-time detectors, setting a limitation dose measurements that require an immediate response [8].

Apart from radiochromic films, ionizing radiation detectors are based on an electronic readout system that acquires a signal associated to the radiation passage. Such detectors are divided in *direct* and *indirect* radiation detectors. In direct radiation detectors, radiation is directly converted in electrical charges that are collected by electrodes. Direct radiation detection is performed by semiconductor-based detectors and ionization chambers. Indirect radiation detection means that the ionizing radiation is first converted into non-ionizing radiation (UV or visible photons) before being converted to electrical charge and being collected. Indirect radiation detection is

Table 2: Main properties of the scintillators used in radiation detection. Data taken from [90]

Phosphor	**Density ($g\ cm^{-3}$)**	**Decay time (ns)**	**Efficiency (%)**	**Em. wavelength (nm)**	**Afterglow**
ZnS:Ag	3.9	≈1000	17-20	450	Very high
$CaWO_4$	6.1	6×10^3	5	420	Very low
Gd_2O_2S:Tb	7.3	6×10^5	13-16	540	Very low
Gd_2O_2S:Pr, Ce, Fe	7.3	4000	8-10	490	Very low
LaOBr:Tb	6.3	$\approx 10^6$	19-20	425	Low
$YTaO_4$:Nb	7.5	≈2000	11	410	Low
Lu_2O_3:Eu	9.4	$\approx 10^6$	≈8	611	Medium
$SrHfO_3$:Ce	7.7	40	2-4	390	Not reportred

performed by scintillators. An insight into the main properties of these detectors is given below:

Scintillators are indirect detectors, since the radiation is not directly converted in electrical signal, but the ionizing photons are first converted to non-ionizing photons (often visible photons) due to the scintillation mechanism. Scintillation is a luminescence phenomenon, in which the electrons and holes produced by ionizing radiation recombine radiatively emitting visible photons [90]. The scintillator is then coupled with a photodetector to detect the visible photons produced by the scintillator. Scintillator materials show different properties and have different use depending on the application. Some important features to consider in the choice of a scintillators are efficiency (or yield), emission spectrum and decay time. A list of the most common scintillators with their properties is reported in Table 2 [90]. The efficiency represents the ability of a scintillator to convert ionizing radiations into visible photons. Since a fraction of the energy of the incident radiation is lost non-radiatively before a radiative emission occurs, the efficiency of scintillator is often way less than 100%. The emission spectrum is of particular importance when the scintillator is coupled with a photodetector since the photodetector responds differently to different wavelengths. The decay time plays a crucial role when high frequency operation is needed. Scintillators can be fabricated in different shapes and structures (crystalline, amorphous, plastic) and can be also fabricated in flexible thin films, allowing to exploit them in wearable devices. Scintillator detectors are preferable to obtain wide energy range detection and large active area, because they are cheap and can be fabricated in large sizes. However, the indirect conversion yield of scintillators is much lower than the direct one of semiconductors or ionization chambers. Moreover, their energy resolution is reduced.

Ionization chambers are gas-filled detectors that measure the charge produced by the ionizing radiation fluxes. They are composed of a chamber filled with gas with a cathode and an anode biased at high voltage to generate a strong electric field. When ionizing radiations pass through the chamber they ionize the gas, generating electron-ion pairs. The electron-ion pairs drift towards the electrodes thanks to the electric field and are collected by an electrometer. Ionization chambers are real time detectors, since the response signal is proportional to the radiation flux and it is immediately recorded as it depends mainly on the drift time (μs for e^- and ms for ions [91]) of the generated charges to the electrodes. Nevertheless, they require voltages of few hundred volts to operate and they are cumbersome and not suitable as flexible devices.

Semiconductors offer advantageous properties for radiation detection such as high cross section, linear response with deposited energy, great energy resolution, fast response, good radiation hardness, and small detector sizes. Radiation detection has indeed focused for decades on inorganic semiconductors, especially on silicon (Si) and germanium (Ge). Similarly to ionization chambers, radiations generate charges (electrons e^- and holes h^+ in this case) in the semiconductor that drift towards the electrodes where they are collected (Figure 20). The electron-hole pairs produced can be calculated diving the energy of the incoming radiation by the hole-pair production energy of the semiconductor (e.g. 3.62 eV for Si, 2.96 eV for Ge), assuming all the energy of the radiation to be released in the active area of the detector. Si and Ge also present high carrier mobility μ and carrier lifetime τ ($\mu\tau > 1$ cm^2 V^{-1}) [92], facilitating the charge collection and improving collection time. Nevertheless, these elemental semiconductors are bulky and hardly compatible with flexible structures, missing the requirements of the new generation of wearable detectors. Further limitations are related to the low bandgap of the materials (1.12 eV for Si, 0.67 eV for Ge), which requires the detectors to be operated at low temperatures, and to their limited X-ray absorption associated to relatively low Z (Si = 14, Ge = 32). Such limitations led to the study of several inorganic semiconductors as radiation detector materials alternatives. Group II-VI compound semiconductors such as cadmium telluride, sulfide and selenide (CdTe, CdS, CdSe) and zinc telluride, sulfide, selenide and oxide (ZnTe, ZnS, ZnSe, ZnO) has been extensively investigated [93]. They benefit from higher atomic number with respect to Si and Ge, leading to higher X-ray attenuation.

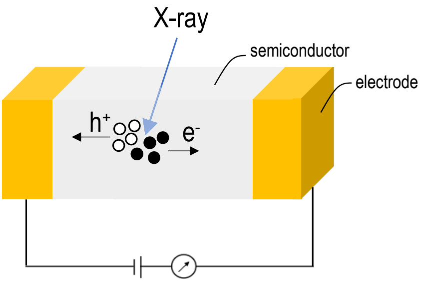

Figure 20: scheme of the semiconductor detection mechanism.

Also, they possess higher bandgap and thus can be operated at room temperature maintaining low dark currents. The main properties of the semiconductors used for radiation detection are reported in Table 3 [94]. Among Group II-VI compound semiconductors CdTe has been the most studied for radiation detection applications, due to high quantum yield, low dark current, small size, flexibility and low-cost production process. Unfortunately, compound semiconductors suffer from poor carrier mobility and lifetime ($\mu\tau$ = 10^{-5} – 10^{-3} cm^2 V^{-1}), with respect to elemental semiconductors.

The detectors mentioned above are used in diverse dosimetric applications, providing reliable radiation measurements. However, there is still a vast technological demand for detectors to be used for in-vivo applications. With in-vivo dosimetry we refer to real-time measurements of the dose on a target during the exposure. In-vivo dosimetry is of particular interest for medical applications (i.e. radiotherapy, diagnostic), where the amount of the delivered dose plays a critical role, and avoiding unwanted excess dose on the body is of major importance. In-vivo dosimetry requires to use real-time detectors that produce an immediate output. Also, a crucial requirement for the detector is not to perturbate significantly the radiation beam. This allows to put the detector between the source and the target during irradiation without affecting the radiation delivery. Human tissue equivalent composition of the detector

Table 3: Main properties of the semiconductor used for radiation detection. Data taken from [94]

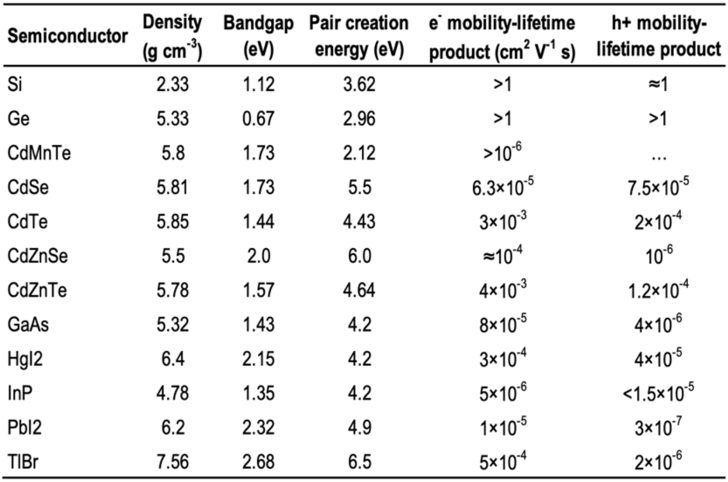

Semiconductor	Density ($g\ cm^{-3}$)	Bandgap (eV)	Pair creation energy (eV)	e^- mobility-lifetime product ($cm^2\ V^{-1}\ s$)	h+ mobility-lifetime product
Si	2.33	1.12	3.62	>1	≈1
Ge	5.33	0.67	2.96	>1	>1
CdMnTe	5.8	1.73	2.12	$>10^{-6}$	…
CdSe	5.81	1.73	5.5	6.3×10^{-5}	7.5×10^{-5}
CdTe	5.85	1.44	4.43	3×10^{-3}	2×10^{-4}
CdZnSe	5.5	2.0	6.0	$\approx10^{-4}$	10^{-6}
CdZnTe	5.78	1.57	4.64	4×10^{-3}	1.2×10^{-4}
GaAs	5.32	1.43	4.2	8×10^{-5}	4×10^{-6}
HgI2	6.4	2.15	4.2	3×10^{-4}	4×10^{-5}
InP	4.78	1.35	4.2	5×10^{-6}	$<1.5\times10^{-5}$
PbI2	6.2	2.32	4.9	1×10^{-5}	3×10^{-7}
TlBr	7.56	2.68	6.5	5×10^{-4}	2×10^{-6}

materials would be beneficial since it would not require cumbersome energy calibration procedures typical of the inorganic semiconductors. Ultimately, to adapt to the target, the materials must be compatible with flexible devices that can eventually be worn. Considered the mentioned requirements, the current commercial detectors are not particularly suitable for in-vivo dosimetry. Although radiochromic films are flexible and might allow low radiation perturbation, they are intrinsically not real-time detectors, and their development might require several hours. Ionization chambers are cumbersome devices that are not suitable to adapt to the target. As for standard semiconductors, it is instead difficult to fabricate them onto flexible substrates and they cannot be fabricated in a way that avoids perturbating the radiation field, especially in the low energies regime used for diagnostic purposes (< 10^2 keV). Finally, the scintillators are generally fabricated as bulk crystals, but, even in the case of thin plastic scintillators, the electronics related to the visible photon detection remains a limiting factor.

Posar et al. [8] recently published a review addressing the issue of in-vivo dosimetry and reporting different solutions that have been subject of the recent research. This introductory section takes inspiration from that work.

To overcome these limitations, in the last years research has focused on the study of thin semiconducting films. Thin films indeed display lower absorption compared to thicker semiconductors and are often compatible with flexible structures. Several solutions have gained attention lately, based on organic, and hybrid organic-inorganic materials, reporting good detection efficiencies (see below).

A convenient way to compare detector efficiencies, often used to describe the performance of direct thin photodetectors, is to define the so-called X-ray sensitivity. X-ray sensitivity refers to the ability of the detector to generate charge when irradiated with X-rays. This depends intrinsically on the material conversion efficiency and extrinsically on the dose delivered and the volume of the active material. In fact, larger doses are expected to generate more charge in the active material and the larger material volumes are associated with larger radiation absorption. Therefore, sensitivity can be defined as the amount of photogenerated charge collected by a detector, (given by the time integral of the photogenerated current) for unit dose and volume. This can be expressed according to the equation [95]:

$$S = \frac{\int (I_X - I_D)dt}{D \cdot V} \tag{1}$$

where I_X, I_D, D and V represent the current recorded under X-rays, the current recorded in dark conditions, the dose, and the active volume of the material, respectively. When interested in the response of the detector per unit area, we can calculate the area sensitivity, by dividing the collected charge by the area of the active material, instead of its volume.

Organic based materials have been investigated as solutions for in vivo dosimetry applications. Beside the possibility to build thin films out of them, organic materials show limited attenuation due to their low atomic number Z, they have tissue equivalent composition, compatibility with flexible substrates and low-cost production methods. Several works have been reported on organic based thin films for radiation detection, displaying remarkable X-ray response to X-rays.

Different works reported radiation detectors based on organic semiconducting single crystals (OSSCs). OSSCs are highly ordered lattices composed of aromatic molecules and kept together by van der Waals forces [96]. The high order is responsible for a good charge carrier mobility (1-100 $cm^2\ V^{-1}\ s^{-1}$) [97–99], leading to high radiation sensitivity. However, OSSCs fabrication is far from easy and requires a fine control of the solution-based growth processes. Nevertheless, by varying the process parameters it is possible to grow crystals with thickness from few mm to as thin as 150 µm [100] adaptable on flexible substrates. 4-Hydrocyanobenzene (4HCB) has been used as direct X-ray detector active material showing sensitivities up to 292 $\mu C\ Gy^{-1}\ cm^{-3}$ at 500 V for 400 µm thick 4HBC under a 35 kVp X-ray beam [8,101]. However, to be used in wearable structures, the thickness must be kept as low as 5 µm. Also, to achieve such sensitivity values, the operating voltage is kept at hundreds of volts, threatening the safety of the patient when used in its closed proximity.

Polycrystalline films have also been considered recently as radiation sensitive materials. The pentacene derivative 6,13-bis(triisopropylsilylethnyl) pentacene (TIPS-pentacene) has been used as direct radiation detector. Basiricò et al. [102] fabricated an OFET based on a microcrystalline 100 nm thick TIPS-pentacene film obtained by drop casting. The detector reported high sensitivity of 77 μC Gy^{-1} cm^{-3} to 35 kVp X-rays at operating voltages below 1 V. The detector was fabricated on flexible PET substrate and maintained good sensitivity after bending. Therefore, microcrystalline materials as TIPS-pentacene might be a better solution for direct X-ray detection to be operated at low voltages, compared to OSSCs.

Perovskites have also been reported as materials for radiation detection. Perovskites are organometallic crystalline materials having ABX_3 structure, with A being an organic or inorganic cation (e.g. $MA^+ = CH_3 NH_3^+$ or Cs^+ , respectively), B a metal ion, and X a negative ion (typically halides) [8]. Perovskites can be fabricated in thin films with solution evaporation methods and vapor assisted methods [103] making their fabrication easily scalable for large production. Perovskites have been largely studied for solar cell applications and they achieved startling optical-to-electrical power conversion efficiency (∼25%) [104], demonstrating to be a valid alternative to silicon solar cells. Their performance is due to remarkable electronic properties such as carrier mobility (60 cm^2 V^{-1} s^{-1}) [105] and long carrier lifetime that allow large charge collection in small volumes. This is desirable also for ionizing radiation detection and thus they have been recently considered for this application. The highest sensitivity for a single crystal perovskite was obtained with a 800 um thick wafer of $MAPbI_3$ which reported 1.53×10^6 μC Gy^{-1} cm^{-3} at 10 V bias with a 40kV X-ray source [106]. A flexible quantum dots (QDs) lead halide perovskite based detector was reported by [107] and showed exceptional sensitivity to synchrotron X-rays (8.85×10^6 μC Gy^{-1} cm^{-3}) with a voltage bias as low as 0.1 V. The film was extremely thin (∼20 nm) and it was deposited by inkjet printing on a flexible PET substrate, showing a reduction in sensitivity of 12 % only after 200 bending cycles. However, perovskite detectors require calibration to obtain tissue equivalent doses, because of the high Z especially of Pb (Z= 82), which is also highly toxic. Detector based on lead-free perovskites have been reported [108,109], reducing the toxicity of the material, but replacing Pb with other high Z elements (Z of Br = 35, Ag = 47, and Bi = 83). Moreover, perovskite stability in air is still an issue, and degradation of the crystalline film is far from being solved. Furthermore, perovskites showed in some cases degradation also at very low radiation fluences, during material characterization experiments [110, 111] and more radiation tolerance experiments still have to be performed to define if they might be suitable for radiation detectors.

Organic semiconductors based on conjugated polymers have been studied alone or in combination with small molecules for direct radiation detection. They are electrically conductive thanks to the delocalized π-electrons arising from the $2p_z$ orbitals overlap in sp^2 hybridization of carbon atoms. Combination of polymers and small molecules can be used to build donor/acceptor systems, to favor charge transport. They are generally fabricated via solution-based techniques (mainly spin coating and drop casting), enabling versatility and scalability of the process [8]. Poly (3-hexylthiophene-2,5-diyl) (P3HT) has been the most used semiconducting polymer for X-ray detection so far. It is common to blend P3HT with phenyl - C_{61} - butyric acid methyl ester (PCBM), which works as acceptor molecule. P3HT:PCBM has been used in combination with Bi_2O_3 nanoparticles [95] and Gd_2O_2S:Tb nanoparticles [112] achieving sensitivities in the order of 10^6 μC Gy^{-1} cm^{-3}. Temiño et al. [113] reported a three-terminal device based on a thick TIPS-pentacene film of 90 nm, in which the addition of polystyrene (PS) improved the sensitivity to X-rays up to 3.2×10^9 μC Gy^{-1} cm^{-3}, which is up to date the best performance ever recorded among organic and inorganic solid state detectors [95].

Despite the great potential of organic- and hybrid-based radiation detectors, something that must be considered carefully is the radiation hardness of these materials. Radiation hardness is the term used to describe the tolerance or resistance of materials to radiation exposure. Exposure to ionizing radiation might indeed affect performance and lifespan of devices, mainly because the active material may degrade being exposed to radiation. The actual behavior depends on a complex interplay of different parameters, such as total dose, dose rate and type of radiation (photons, charged or neutral particles). Thus, radiation hardness experiments are fundamental since they indicate the applications the detectors can be used for.

While radiation hardness of inorganic semiconductors has been vastly explored and both Si and Ge and group II-VI compound semiconductors generally exhibit high radiation tolerance [93], for organic materials the answer is not straightforward. Semiconducting polymers demonstrated low radiation resistance. Therefore, they have been initially considered mostly for low exposure applications (e.g. diagnostic purposes). Degradation of semiconducting polymers under radiations is associated to the breaking of C-H and C-C bonds by energetic secondary electrons produced during X-ray photoelectric absorption. This phenomenon is especially observed in conjugated polymers, because of the abundance of C-H bonds, leading to chain scissions and cross-linking, strongly reducing conductivity of the polymers [114]. Another damage mechanism in semiconducting polymers was found to be associated to the doping resulting from the irradiation and affecting the optoelectronic properties of the materials. P-type doping is considered responsible for narrowing the HOMO-LUMO energy gap, resulting in higher conductivity, as observed for P3HT and pentacene based FETs [115,116]. Oppositely n-type doping is associated to an increase of the energy gap limiting hole injection, as reported for rubrene based FET irradiated with electrons [117].

It has been observed that highly ordered organic crystals such as OSSCs show much higher tolerance to radiation compared to semiconducting polymers [118]. This has been associated to the more densely packed crystalline structure of molecular crystals, inhibiting the diffusion of free radicals. 4HCB detectors demonstrated stability and hardness after 2.1 kGy [119]. Although further studies need to be conducted on radiation hardness of OSSCs, they promisingly exhibit excellent radiation resistance compared to other organic semiconductors.

Radiation damage in perovskite has been initially observed in characterization techniques using ionization radiation sources. $MAPbI_3$ exhibited degradation to PbI_2 during electron microscopy experiments [110]. Damages on perovskites has been observed with electrons down to energies of 1.5 keV [120], arising questions about their use even with low energy radiation and low exposure. The degradation mechanism in perovskites from electron irradiation has been associated to the formation of Frenkel-type defects, i.e. the ionized atoms migrate to interstitial site of the lattice. Radiation damage on perovskites has been reported with γ-rays. Perovskite based solar cells exhibit a 20% drop of the optical to electrical conversion efficiency after being exposed to 75 Gy γ-rays, while no further degradation was observed up to 2.3 kGy [121]. Nevertheless, the radiation damage on perovskites has been considered only relatively to the effect it has on the sensitivity in the visible spectrum and thus requires a deeper understanding on how it affects ionizing radiation detectors performance.

In this framework, TMDCs might represent a valid alternative material for in-vivo dosimetry. Although they have been widely considered in the production of opto-electronic devices, to the best of our knowledge, they have never been proposed as ionizing radiation detector materials yet. TMDCs will indeed benefit from high atomic number Z of the transition metal atoms (Mo (Z=42), W (Z=74)), which will result in high cross-section for X-ray interaction. Also, the ultra-thin structure of TMDCs will result into minimal perturbation of the radiation beam, allowing to put a detector between source and target and real time monitoring of radiation quantities during target irradiation. These features, combined with remarkable carrier transport properties already discussed above, will allow efficient collection of photogenerated charges. TMDCs have also demonstrated to be suitable to be employed in flexible detectors, opening the way to fabricate wearable devices required for in vivo applications. Ultimately, TMDCs demonstrated high radiation resistance to protons (10^{16} /cm^2) and alpha particles (10^{15} /cm^2) [77,122] and showed good stability in ambient air [123]. In chapter 3 the first example of an X-ray detector based on 1L-MoS_2 will be presented, demonstrating its use for dosimetry. This indicates a promising pathway towards the use of TMDCs detectors for in-vivo applications.

Chapter 2: Large area MoS_2 based detectors used for photodetectors

As discussed in the introductory section, the development of an industrially scalable process to fabricate 2D-MoS_2 would be of enormous help to move into a widespread use of electronic devices based on 2D-MoS_2. Therefore, in this chapter we present the development of a method to fabricate large area MoS_2 films to be used in photodetectors. The method is based on a facile sol-gel process that is intended to be versatile, cheap, and it is intrinsically scalable for large production. Also, the synthesis process has a low environmental impact, being performed in a hydroalcoholic medium, and not requiring additional sulfurization or hydrogenation steps. This method represents an important step towards the production of MoS_2 at the industrial level.

The section “materials and methods” begins with a quick introduction on sol-gel processes, which are the basis of the fabrication method proposed here. The section continues describing the experimental setup and the methodological strategies adopted in the study. Afterwards, the results are presented and analyzed in the “result and discussion” section. The fabricated MoS_2 films display large area and good morphology, as well as modest crystallinity. The obtained photodetectors showed light detection in a wide spectral range, from the near ultraviolet to near infrared. The results also show critical points in terms of detector performance, associated with defectivity of the material in the presented method. In the last experimental section “towards high quality MoS_2 films for flexible photodetectors” a strategy to achieve higher quality MoS_2 films and overcome the current limitations of the method to the production of films on flexible substrates is proposed. Finally, conclusions on the work are provided, summarizing novelties and limits of the presented method, and suggesting ideas for further works.

A significant part of the work presented in this chapter has been recently published as a research paper entitled: *Large area MoS_2 films fabricated via sol-gel used for photodetectors*, on the journal *Optical Materials, Elsevier*. The paper can be found at:

A. Taffelli, G.Ligorio, L. Pancheri, A. Quaranta, R.Ceccato, A. Chiappini, M. V.Nardi, E.J.W. List-Kratochvil, S. Dirè, Large area MoS2 films fabricated via sol-gel used for photodetectors, Optical Materials, Volume 135, 2023, 113257, ISSN 0925-3467, https://doi.org/10.1016/j.optmat.2022.113257. [9]

2.1 Materials and methods

2.1.1 Sol-gel process

The physics and chemistry of sol-gel processes is extensively described in the book *Brinker and Schrerer 1990* [124]. Here we report a brief introduction summarizing the main features of the process, which has been widely applied since 1980s to the production of glass and ceramics.

A *sol* is defined as a colloidal suspension of solid particles in a liquid. The term *colloid* refers to a suspension in which the dispersed phase dimensions are in the range ~ 1-1000 nm and are so small that the interactions are dominated by short-range forces (e.g. van der Waals and surface charges), while gravitational forces are negligible. Sols can be used to produce particles from which ceramic materials are made. This can be achieved by a sol-gel process. In a sol-gel process, a sol is obtained starting from inorganic or organic compounds (*precursors*), containing a metal or metalloid element, which react with water through *hydrolysis* and *condensation* reactions.

When dealing with inorganic compounds containing transition metals, as in the case of study, the precursors are generally introduced as salts in an aqueous medium, and are solvated by water molecules. Depending on the water pH, hydrolysis proceeds forming *aquo*-, *hydroxo*-, or *oxo*-ligands with the transition metals. Depending on the amount of water, precursor concentration and catalyst, hydrolysis may go to completion, hydrolyzing all the precursor molecules. Two partially hydrolyzed molecules can link together through condensation reactions. This happens via two mechanisms, namely *nucleophilic substitution*, and *nucleophilic addition*, depending on the coordination number of the metal. In nucleophilic substitution, one ligand group (nucleophile) coordinates the two transition metal atoms, substituting the second ligand group which is released. In nucleophilic addition the second ligand group is instead added to the nucleophile group which coordinates both the transition metals.

The progress of the condensation (*polymerization*) leads to the sol-gel transition: when the molecules connections extend through the whole solution volume, we speak of a *gel*. A dried gel is generally obtained through solvent evaporation at ambient pressure, (named *xerogel* from xero, meaning dry), with associated network shrinkage. To fabricate a dense ceramic, a heating step is often required to convert the amorphous xerogel in a crystalline dense material (Figure 21, branch 1).

One of the most technologically relevant aspects of the sol-gel process is that the sol can be used to obtain thin films via dip-coating or spin-coating deposition onto suitable substrates. During the deposition, solvent evaporation along with condensation reactions lead to the formation of a xerogel thin film [125]. The xerogel film, similarly to the bulk case, requires a heating step to obtain a dense ceramic thin film (Figure 21, branch 2).

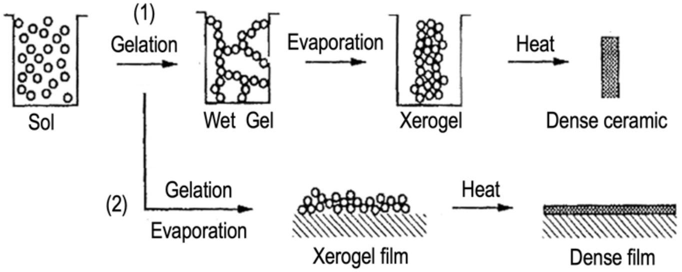

Figure 21: Scheme of the sol-gel process to obtain ceramic materials. Adapted from [124].

2.1.2 Aqueous sol synthesis

MoS_2 was obtained by adapting a previously reported sol-gel synthesis [7]. Ammonium molybdate tetrahydrate [$(NH_4)_6Mo_7O_{24}\cdot 4H_2O$] was used as molybdenum precursors and thioacetamide (CH_3CSNH_2) as sulfur precursor. Diethylene-triaminepentaacetic acid (DTPA) ($C_{14}H_{23}N_3O_{10}$) was used as chelating agent. The reagents were purchased from Sigma Aldrich (Sigma-Aldrich, USA). As illustrated in Figure 22, in the reaction the sulfur atoms of thioacetamide substitute the terminal oxygen atoms of the $[Mo_7O_{24}]^{6-}$ group. Polymerization of the new formed $[Mo_7O_{12}S_{12}]^{6-}$ groups is accomplished with the addition of DTPA. The chelating agent can indeed coordinate up to three $[Mo_7O_{12}S_{12}]^{6-}$ groups, promoting the formation of a network. The synthesis procedure followed the following steps: i) Ammonium molybdate (400 mg) powder was added to deionized water (16 ml) and stirred at RT until complete dissolution. ii) Thioacetamide (1.2 g) powder was dissolved in the solution and left stirring at room temperature until the solution color turned into light blue (~20 min). iii) DPTA (0.1 g)

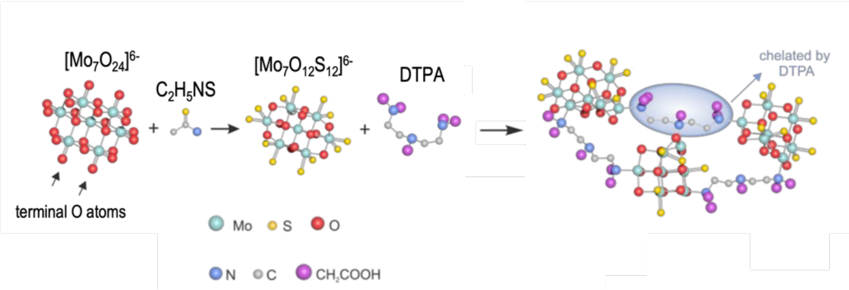

Figure 22: Scheme of the reactions taking place in the sol-gel process. Adapted from [7].

After dissolution of the ammonium molybdate and thioacetamide

After 1 hour from DTPA addition

After 4 hours from DTPA addition

Figure 23: Stages of the MoS_2 sol-gel synthesis at different reaction times. Reprinted with permission from [9]. © 2022, Elsevier B.V. All rights reserved.

was added to light blue solution and stirred first at room temperature for 1h and then for 3h at 60 °C. In this last stage the system was connected to a condenser to avoid solvent evaporation. This resulted into a dark brown viscous solution. Stages of the synthesis are illustrated in Figure 23.

2.1.3 Sol dilution

The aqueous solution was diluted with three common alcohols, namely 2-butanol, 2-propanol and ethanol, in a volume ratio of 80% water : 20% alcohol to improve the substrate wettability. The main properties of the alcohol listed above are reported in Table 4. Three diluted solutions were obtained, one for each of the alcohol listed above. The addition of the alcohols is the key for the fabrication of films with higher uniformity as it improves substrate wettability (see below). Therefore, the employment of an alcoholic medium in the synthesis process was considered. However, the precursors (DTPA especially) were found to be insoluble in standard alcohols. For this reason, the synthesis was subsequently performed in a hydroalcoholic medium, namely a mixture of 13 ml of deionized H_2O and 3 ml of 2-butanol, following the procedure described in 2.1.2. The solutions obtained with and without the addition of the alcohols were used for the fabrication of the xerogel films.

Table 4: main properties of the solvent used to dilute the aqueous solution. Data taken from [126].

Solvent	Density at 25°C (g cm^{-3})	T boiling (°C)	Surface tension at 25 °C (g/s^2)	Dipole moment (D)	Viscosity at 25 °C (Pa s)
water	1	100	72.7	1.85	8.9×10^{-4}
2-butanol	0.805	99	22.6	1.66	31.0×10^{-4}
2-propanol	0.783	82	23.3	1.66	20.4×10^{-4}
ethanol	0.787	78	22.0	1.69	10.7×10^{-4}

2.1.4 Coatings deposition

The xerogel films were obtained via spin-coating of the obtained solutions. Different substrates were employed in the process, namely silica, silicon, gold, soda-lime glass, indium-tin oxide (ITO). The substrates were cleaned prior to the deposition via ultrasonic bath first in acetone and then in 2-propanol for 15 min each and dried under N_2 flux. Finally, the substrates were kept under O_2 plasma for 5 min to clean them from organic residuals and to activate their surface for the deposition.

Films obtained from the aqueous solution suffered from low spreading on the surface and poor homogeneity (see section Results and discussion). To improve the film quality different parameters were varied in the deposition process (spin-coating velocity, volume deposited, number of layers deposited) with no significant improvement. Eventually, for the films obtained through the hydroalcoholic synthesis a single deposition was enough to obtain a continuous film spread all over the substrate. These films were obtained through the deposition of 50µL using the following six steps spin-coating procedure: (i) acceleration from 0 to 1300 rpm in 2 s, (ii) 2 s at 1300 rpm, (iii) acceleration from 1300 to 2000 rpm in 2 s (iv) 2 s at 2000 rpm, (v) acceleration from 2000 to 3000 rpm in 1 s, and finally (vi) 3000 rpm for 49 s. The obtained films were then dried on a hot plate at 100 °C for 5 min.

2.1.5 Coatings thermal annealing

As discussed above, to convert the xerogel films into MoS_2 films a thermal annealing treatment is required. This treatment was performed in a tubular silica furnace. To avoid oxidation processes during the conversion, the furnace was constantly flushed with argon (flux 200 sccm) for the whole treatment. The latter consisted in 2 hours at room temperature to clean the furnace from residual oxygen, followed by a heating ramp of 4 °C/min to reach the temperature desired for the treatment. The temperature was kept for 5 hours. Different temperatures were investigated (400 °C, 500 °C, 600 °C). Eventually the furnace was brought to room temperature by free cooling. The treatment does not require additional sulfurization/hydrogenation step, avoiding the disposal of toxic byproducts such as hydrogen sulfide (H_2S).

2.1.6 Device fabrication

To produce the photodetectors based on MoS_2 films we used substrate made of soda-lime glass. To engineer the substrates, electrodes were fabricated via the thermal evaporation of 100 nm of gold using shadow masks. The schematical representation of the device is reported in Figure 24. The electrode layout consists of five equal and independent couples of finger-shaped anodes and cathodes. Each anode/cathode couple is separated by a channel of the size of 1 mm × 30 µm (channel area of 0.03 mm^2). The lateral pads serve as electrical contact points for the test board used for

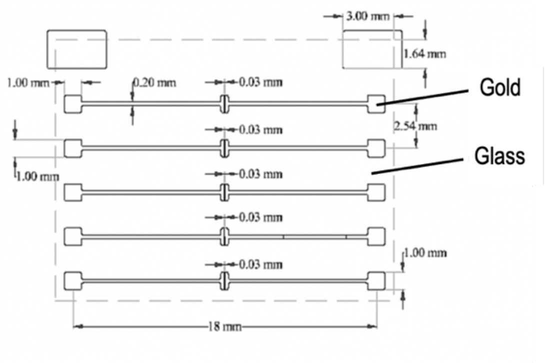

Figure 24:Schematical representation of the engineered substrates used to fabricate the photodetectors.

the measurement (see below in Appendix A for further details). We obtained a yield of 4 out 5 working devices per sample, for a total of 16 out 20 working devices. Among these, a device was characterized in the spectrum UV-VIS-NIR spectrum as representative of the batch.

2.1.7 Characterization techniques

For the basis on the main characterization techniques used here, we refer to Appendix A. Optical images of the surface of the film were acquired with a Nikon SMZ25 optical microscope. Non-resonant microRaman spectra were acquired on the films with a LabRAM Aramis (Horiba Jobin-Yvon, Japan), equipped with an optical microscope mounting a 100 × objective employing a 532 nm pumped diode laser to excite the non-resonant Raman signal. XPS was performed with a Joel JPS- 9030 (Joel Ltd., Japan) using a monochromatic Al K_α source (E = 1486.7 eV). The films analyzed with XPS were fabricated on ITO coated glass substrates. The samples were exposed to ambient air for the time needed to transfer them on the XPS holder (few minutes), before bringing them to UHV for the analysis. Scanning electron microscopy (SEM) images of the surface and cross-section of the films were acquired with a Carl Zeiss Gemini Supra 40 (Zeiss, Germany). Thermogravimetric analysis and differential thermal analysis were performed on the xerogel powders obtained via drying the gel for 48 hours at 60 °C. The analysis was performed with a Netzsch STA 409 thermobalance (Netzsch-Gerätebau GmbH, Germany), in the range between 20 °C and 900 °C, at heating rate of 10 °C/ min in flowing argon gas. XRD spectroscopy was performed with a Rigaku D/III max diffractometer (Rigaku, Japan), using Cu K_α radiation (λ = 1.54056 Å) and a curved graphite monochromator for the diffracted beam to be analyzed. Glancing incident configuration was used, with incidence angle of 1°. Scans were performed in the range 2θ = 10°-70°, with sampling interval of 0.05°, and counting time of 5 s. Crystallite size was estimated with the Scherrer equation [127] for the films treated at 500 °C and 600 °C, assuming the shape factor equal to 0.9. AFM measurements were performed in ambient conditions with a Bruker Dimension Icon using PeakForce Tapping with a ScanAsyst-Air tip (Bruker, USA). Optical absorbance spectra were calculated from transmittance spectra acquired in the spectral range 190 nm < λ < 1200 nm with a JASCO V-570 spectrometer (Jasco, Japan). Electrical and electro-optical characterization of the photodetector were performed with a three-terminal test board (Ossilla, UK) connected to a Keithley 2450 source measurement unit (Tektronic, USA). A device was chosen to be representative of the batch and its photoresponse was measured, as a proof of concept of the material use in a photodetector application. The photoresponse of the device was measured under illumination with different LEDs (Thorlabs, USA). A list of the LEDs with their main properties is reported in Table 5. Responsivity was calculated by measuring the photogenerated current and normalizing it with the light power impinging on the channel of the detector. The light power on the detector channel was estimated starting from the nominal irradiance of the LEDs reported in Table 5, normalized for the distance between the source and the detector (20 mm), and multiplied by the area of the channel (0.03 mm^2). In the calculation, the irradiation of the channel area was assumed to be uniform.

Table 5: Thorlabs LEDs models, nominal wavelength, and irradiance on the detector.

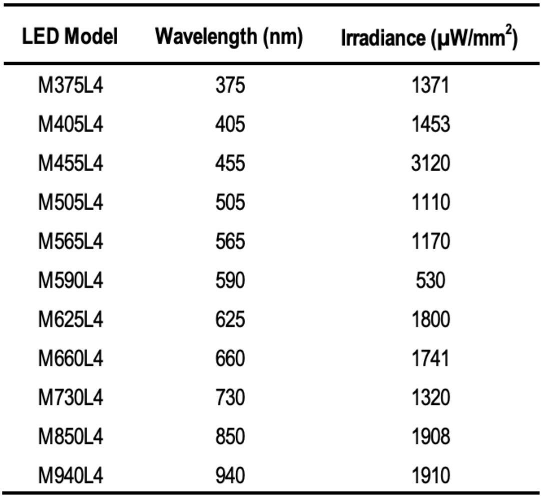

LED Model	Wavelength (nm)	Irradiance (μW/mm^2)
M375L4	375	1371
M405L4	405	1453
M455L4	455	3120
M505L4	505	1110
M565L4	565	1170
M590L4	590	530
M625L4	625	1800
M660L4	660	1741
M730L4	730	1320
M850L4	850	1908
M940L4	940	1910

2.2 Results and discussion

2.2.1 Aqueous sol synthesis

The films fabricated through the aqueous sol-gel synthesis described in 2.1.2 and thermally treated at 500 °C covered the substrate in a non-continuous way. This is shown in Figure 25, reporting an image acquired with the optical microscope. The Si substrate is clearly visible (in light grey), while the film appears to cover only small substrate portions (dark spots). Raman spectra acquired in different regions of the sample confirmed the presence of MoS_2 only on the optically dark regions (Figure 25(b)). The peaks centered at 380 cm^{-1} and 402 cm^{-1} are attributed to the typical in-plane (E^2_{1g}) and out-of-plane (A_{1g}) vibration of MoS_2, respectively (topmost spectral line of Figure 25(b)). The peak distance is 22.3 cm^{-1}, compatible with the value expected for thin MoS_2 films, as previously reported in the literature [128]. In the rest of the substrate the Raman spectrum resulted in a flat line, excluding the presence of MoS_2 (bottommost spectral line of Figure 25(b)). Increasing the solution volume deposited or depositing a second layer on top of the first one, did not improve significantly the substrate covering (Figure 26). Although the presence of MoS_2 was proven and the reproducibility of the previous synthesis confirmed, the non-continuity of the films prevents the fabrication of devices based on this process. The low uniformity of the film was attributed to a very poor wettability of the substrate during the deposition.

2.2.2 Sol dilutions

A simple way to improve the coverage of the substrate is to dilute the solution with standard alcohols. The lower surface tension of alcohols compared to water results in higher wettability of the substrate surface, due to weaker cohesive forces. All dilutions with the alcohols (2-butanol, 2-propanol and ethanol) showed an improved wettability, resulting in films with larger area (~ cm^2) and higher uniformity, with respect to the films obtained with the aqueous solution. This is shown in Figure 27, where optical images of the films obtained through alcohol dilutions are compared.

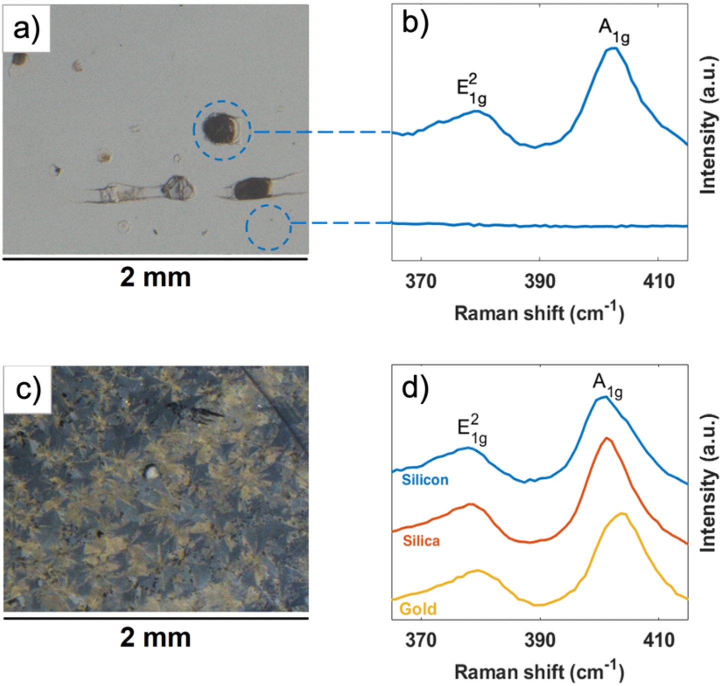

Figure 25: a) Optical microscope image of a sol-gel derived MoS_2 film on a silicon substrate treated at 500 °C, obtained through the recipe described in [7]. b) Raman spectra acquired on different regions of the sample shown in Figure 25(a). c) Optical microscope image of a MoS_2 film treated at the 500 °C deposited on a silicon substrate, obtained through the hydroalcoholic sol-gel synthesis. d) Comparison of Raman spectra acquired on the film shown in Figure 25(c), and on films fabricated on silica and gold substrates obtained with the same recipe. Reprinted from [9]. © 2022, Elsevier B.V. All rights reserved.

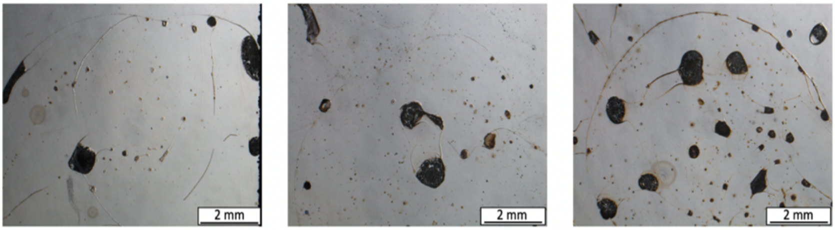

1 drop, 2 layers 2 drops, 2 layers 3 drops, 2 layers

Figure 26: Optical microscope images of the sol-gel films fabricated on silicon substrates derived from the aqueous synthesis, increasing the volume of the sol deposited and depositing a second layer on top of the first one. The drops were deposited through a Pasteur pipette. Reprinted with permission from [9]. 2022, Elsevier B.V. All rights reserved.

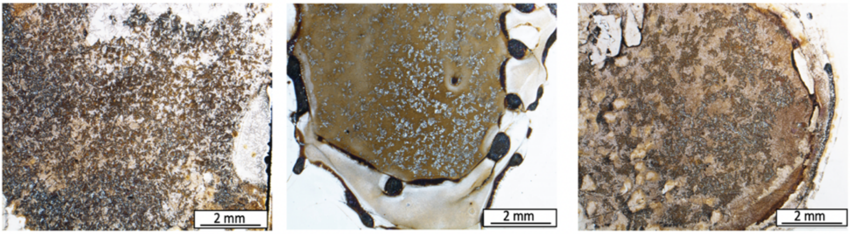

2-butanol 2-propanol ethanol

Figure 27: Optical microscope images of the sol-gel films fabricated on silicon substrates, derived from the aqueous synthesis and diluted in 2-butanol, 2-propanol and ethanol (dilution ratio 80%:20%). The deposition procedure was repeated to obtain a second layer on top of the first one. Reprinted with permission from [9]. 2022, Elsevier B.V. All rights reserved.

2.2.3 Hydroalcoholic sol synthesis

Considered the positive effect of the alcohol addition to the aqueous solution, the sol-gel synthesis was performed in a hydroalcoholic medium. The synthesis was not performed in an alcoholic medium, because the precursors are not all soluble in the mentioned alcohols. Among the alcohols mentioned above, 2-butanol was chosen for the purpose, because of its vapor pressure similar to the one of water, determining similar evaporation rates during the sol-gel synthesis and in the film formation process. The hydroalcoholic medium was obtained adding 3 ml of 2-butanol to 13 ml of deionized H_2O.

In Figure 25(c) a film (thermally treated at 500 °C) obtained on a silicon substrate through the hydroalcoholic synthesis is shown. Comparison with Figure 25(a) makes clear that the introduction of 2-butanol in the synthesis medium has a positive effect in improving the solution spreading on the substrate surface. Similar outcomes were achieved depositing the hydroalcoholic solution on silica and gold substrates, as demonstrated by the optical image reported in Figure 28. The different optical contrasts appearing in the images is attributed to the different grain orientation of the film. The presence of MoS_2 was confirmed on the films deposited on the different substrates thanks to Raman spectroscopy as reported in Figure 25(d). The E^2_{1g} and A_{1g} peaks of MoS_2 are comparable for the different substrates, displaying a distance of 22.3 cm^{-1}. The position of the peaks displays a shift when the substrate varies, as observed in previous studies [129]. Moreover, the Raman spectra acquired in different regions of the samples displayed similar behavior, as shown in Figure 29 in the case of the silica substrate, demonstrating the uniformity of the film. Also, no regions showing the Raman signal of the substrate only were recorded, suggesting continuity of the film.

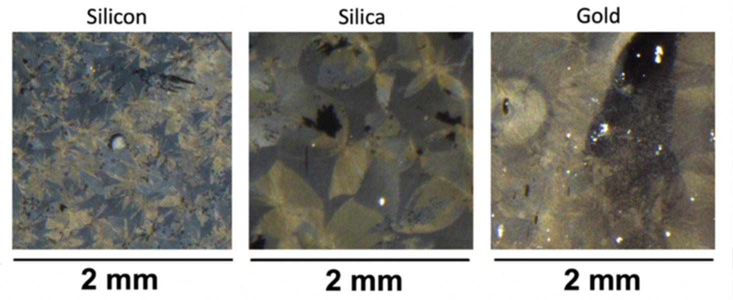

Figure 28: Optical microscope images of the MoS_2 films obtained through the hydroalcoholic synthesis, fabricated on different substrates, namely silicon, silica and gold. The films were thermally treated at 500 °C. Reprinted with permission from [9]. 2022, Elsevier B.V. All rights reserved.

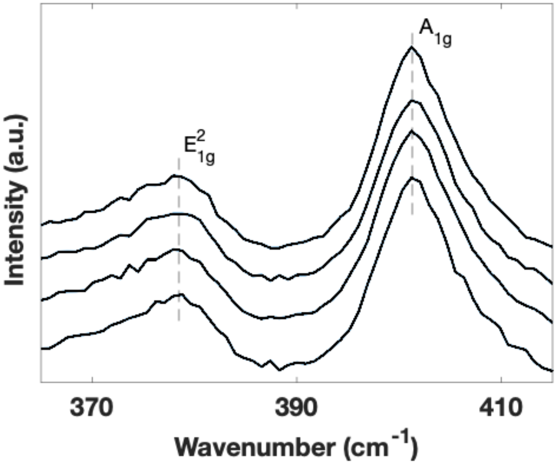

Figure 29: Raman spectra acquired in different regions of a MoS_2 film obtained through the hydroalcoholic synthesis fabricated on silica and treated at 500 °C. Reprinted with permission from [9]. 2022, Elsevier B.V. All rights reserved.

MoS_2 films obtained via the hydroalcoholic synthesis (and treated at 500 °C) were investigated via XPS analysis, to access the chemical composition of the material surface. Figure 30(a) reports the signal from the sulfur S 2p core levels. S $2p_{1/2}$ and S $2p_{3/2}$ peaks are centered at binding energy of 163.3 eV and 162.1 eV, respectively. Figure 30(b) shows instead the sulfur S 2s and the molybdenum Mo 3d core level spectra. S 2s is a single peak is centered at 226.4 eV. Mo 3d is instead represented by a doublet with Mo $3d_{3/2}$ and Mo $3d_{5/2}$ peaks centered at 229.3 eV and 232.5 eV, respectively. The XPS signal is in accordance with the spectrum expected for MoS_2 and reported in the XPS handbook [130].

The survey spectrum is also reported in Figure 30(c), showing binding energies of core levels electrons up to 600 eV. The survey reports carbon species, evidenced by the C 1s peak centered at 284.9 eV. Carbon signal is associated to impurities related to the organic precursors employed in the wet synthesis, due to a non-complete decomposition of the organics during the thermal annealing treatment. Carbon contamination is also possible in the transfer of the sample to the XPS chamber, but we believe that the exposition time was too short with respect to the signal magnitude found in the survey. Silicon is also present in small amounts that is attributed to contamination in the thermal annealing step performed in the quartz furnace. Indium and tin signal are also present, due to the ITO-coated glass substrate adopted for the samples used for the XPS analysis. This is due to cracks in the film area investigated. The relatively high magnitude of the indium signal with respect to molybdenum is also related to the higher photoelectric cross section of indium. Oxide species are also present in the survey spectrum. The O 1s signal peaked at 532.7 eV is associated to the partial oxidation of MoS_2 during the thermal treatment, as well as to oxygen diffusion from the substrate, as observed in previous studies [7]. Using oxide-free substrates will reduce the oxidation of the film, but it will dramatically limit the choice of the possible substrates to be used for the device fabrication. Oxygen contained in the ITO-coated glass substrate partially contribute to the O 1s peak. Finally, a minor contribution may arise also from adsorption of species during air exposition.

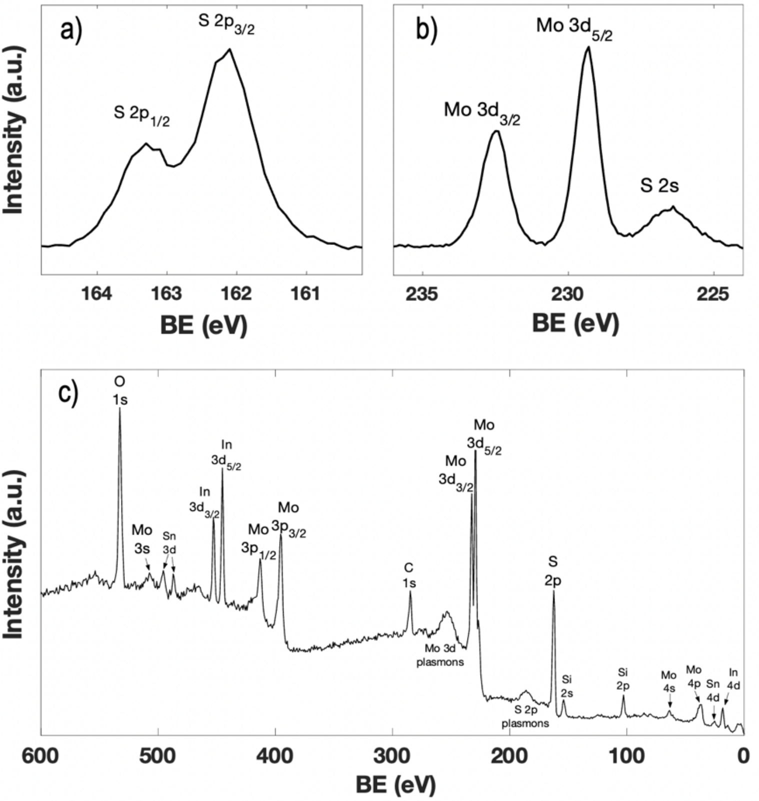

Figure 30 S 2p (a) and Mo 3d and S 2s (b) core level XPS spectra and survey XPS spectrum (c) acquired on MoS_2 films fabricated on ITO-coated-glass treated at 500°C. Reprinted and adapted with permission from [9]. 2022, Elsevier B.V. All rights reserved.

Sputtering of the MoS_2 film surface has been carried out to evaluate the composition of layers below the outer surface but resulted in alteration of the film surface stoichiometry. As reported in Figure 31, the S 2s signal intensity has a drastic reduction while the Mo 3d has a shift of 0.5 eV after sputtering, meaning a loss of bonded with S atoms. This is attributed to a preferential removal by the Ar ions of S atoms compared to Mo. For this reason, sputtering has not been considered as a reliable technique to access the MoS_2 structure beneath the film surface. Nevertheless, sputtering was useful to confirm the presence of carbon also beneath the surface. Therefore, carbon can be associated to a residual of the synthesis process. Silicon is instead attributable to a contamination in the annealing process, since it was not found beneath the surface.

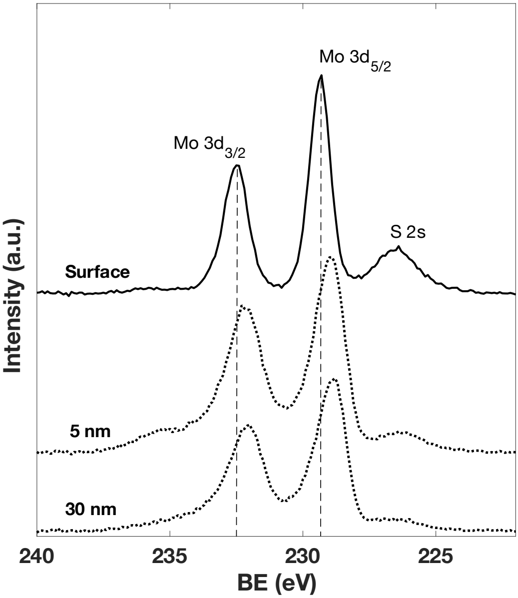

Figure 31: Mo 3d and S 2s core level XPS spectra acquired on the surface of a MoS_2 film treated at 500 °C (topmost solid line) and after removal of the first 5 and 30 nm of the film via argon sputtering.

Morphological investigation of the samples has been performed via scanning electron microscopy (SEM). SEM was used to study the morphology of both the surface and the cross-section of MoS_2 film. To look at the cross section of the film the sample was cut in half and mounted in the SEM chamber exposing the cross-section in the field of view of the microscope. SEM images of the surface and of the cross-section of a MoS_2 sample (after thermal treatment at 500 °C) is reported in Figure 32. In figure a) the surface of the film is shown, displaying a uniform area at low magnification, demonstrating smooth surfaces in areas of several mm^2. The cross-section is reported in Figure 32(b) for a film fabricated on a silica substrate. This evidenced a compact film with thickness around 200 nm.

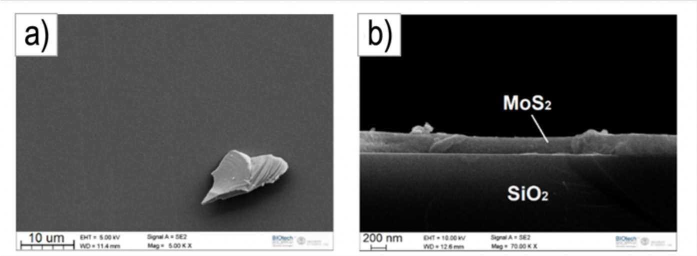

Figure 32: SEM images of the surface (a) and of the cross-section of a MoS_2 fabricated on a silica substrate and annealed at 500 °C. Reprinted with permission from [9]. 2022, Elsevier B.V. All rights reserved.

The thermal evolution of the material was studied by means of thermogravimetric analysis (TG) and differential thermal analysis (DTA). The analyses were performed in argon atmosphere on powders obtained drying the hydroalcoholic solution at 60 °C for 48 h. TG and differential TG (DTG) curves are shown in Figure 33(a). The TG curve (dashed line) shows a significant weight loss up to 500 °C. The weight loss from 500°C to 900°C is less than 5% of the initial weight. The loss below 200 °C is mostly associated with the evaporation of the absorbed solvent molecules. The reactions occurring in the heating process are better understood looking at DTG and DTA curves, compared in Figure 33(b). Between 150 °C and 240 °C the weight loss is associated with the endothermic reduction of Mo^{6+} to Mo^{5+} and to loss of entrapped H_2S, as reported in a previous study [131]. At higher temperatures the weight loss is attributed to endothermic reduction of Mo^{5+} to Mo^{4+} species of MoS_2, and exothermic crystallization of MoS_2, resulting in an overall exothermic behavior of the DTA. Finally, a weight loss of 5% is evidenced by a peak at 425 °C in the DTG curve and it is associated with the exothermic decomposition of the chelating agent (DTPA) showed in the DTA curve [7]. No other reactions are observed in the analysis. Nevertheless, it has been demonstrated [131] that in presence of oxygen species, at temperature above 430°C, it is likely to have oxidation reactions of MoS_2. It is thus recommended to work in oxygen free atmosphere. The thermal analysis also suggests that a treatment at temperatures higher than 425°C are needed to obtain MoS_2 and to decompose the chelating agent. This excludes the use of flexible substrates (PET, Kapton) for the film fabrication, limiting the versatility of the method.

The crystalline structure of the films obtained using the hydroalcoholic solution was investigated via XRD experiment for samples thermally treated at 400°C, 500°C and 600°C. Figure 34(a) reports the XRD spectra for films fabricated on silica substrates at different temperatures. For the sake of clarity, only the 2θ range between 10° and 30° is shown. Thermal treatment at 400°C results in very low crystallinity of the MoS_2 film (blue line). The crystallinity is significantly improved with a 500°C treatment, and it is evidenced by the broad peak centered at $2\theta = 13.6°$ (orange line). The position of the peak is shifted with respect to the (002) crystallographic plane expected for 2H-MoS_2 ($2\theta = 14.378°$, according to PDF card n° 37-1492) and it has been already observed for sol-gel derived samples. The value is associated with a distance between the planes of 6.5 Å, instead of 6.1554 Å, highlighting an expansion of the c-axis of the unit cell of 2H-MoS_2, probably induced by the presence of organic residues not fully decomposed with the thermal treatment. A treatment at 600 °C is shown to increase both crystallinity and crystallite dimensions, as indicated by a sharp peak centered at $2\theta = 14.3°$ (yellow line). The crystallite size was estimated with the Scherrer equation on the (002) peak of the XRD spectra, showing an increase of the crystallite size from 1.7 nm to 13.6 nm, when the temperature increases from 500 °C to 600 °C. However, the calculation might be subject to significant fluctuations since the broadening from the instrumentation was not considered and an average on multiple peaks was not performed. Nevertheless, it qualitatively indicates the improvement of the film crystallinity. No signals have been detected outside the 2θ 10°- 30° range, apart from a shoulder observed at $2\theta \approx 20°$, associated to the silica substrate. The absence of further MoS_2 peaks in the XRD spectrum is due to a preferential crystal growth in the [002] direction, probably induced by the substrate.

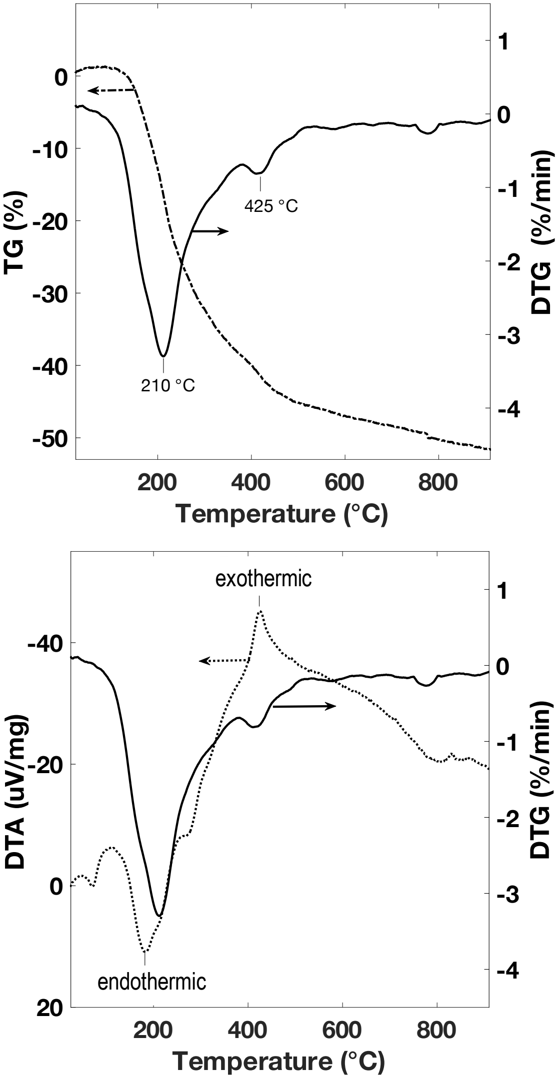

Figure 33: TG (dashed line) and DTG (solid line) curves (top) and DTG (solid line) vs DTA (dotted line) curves (bottom) acquired on the xerogel powders obtained via drying the hydroalcoholic solution for 48h at 60 °C. Reprinted and adapted with permission from [9]. 2022, Elsevier B.V. All rights reserved.

AFM measurements were performed on the surface of MoS_2 films annealed at 500°C and 600°C. The structures observed for the MoS_2 film treated at 600°C have a mean size of 35.6 nm, ascribable to crystalline features grown in the thermal treatment. The root-mean-square surface roughness is 4.8 nm for the films treated at 600°C and 0.8 nm for the films treated at 500°C.

The films displaying crystalline 2H-MoS_2 phase (treated at 500 °C and 600 °C) were optically characterized via UV-VIS-NIR absorption experiments. In the absorbance spectrum of the MoS_2 film treated at 600 °C (yellow line, Figure 34(b)), the A and B peaks represent the typical A and B excitons associated to the MoS_2 phase, centered at 1.83 eV and 1.98 eV respectively, in accordance with previously reported values [28]. The distance between A and B excitons represents the valence band energy splitting and it is about 150 meV, compatible with the value expected for 2D-MoS_2 film [25]. The C peak represents the band edge energy at the K-point of the Brillouin zone and it was observed to vary depending on the thickness of the MoS_2 film. The C peak is centered at 2.74 eV, value in agreement with 2D-MoS_2 [28].

MoS_2 films treated at 500 °C display an absorbance trend similar to the one obtained for the films treated at 600 °C, but A and B excitons are represented by shoulder rather than two separated peaks (orange line, Figure 34(b)). The difference may arise from the lower crystallinity of the sample treated at 500 °C, as reported above in the XRD analysis. This indicates that crystallinity might be an indicator for the optical properties of the material and high-crystallinity may be required to achieve the energy band distribution expected for 2D-MoS_2.

Independently from the thermal treatment temperature, the absorbance spectrum shows a non-negligible absorption tail in the IR. The tail is more pronounced for the film treated at 500°C, while for the sample treated at 600°C the transition between IR and VIS absorption is steeper. The tail of absorption in the IR is attributed to energy states populating the bandgap, ascribable to defects of the materials in form of residual organic impurities and oxide species, as observed in the XPS survey spectrum (see above). A higher temperature treatment will improve the optical properties of the material (as already observed for films treated at 600 °C), due to a more efficient decomposition of the organic species. Nevertheless, temperatures higher than 450-500°C demonstrated to induce further oxidation of the MoS_2 films either from the substrate or from the environment and will drastically limit the choice of the substrates to be used for the device fabrication.

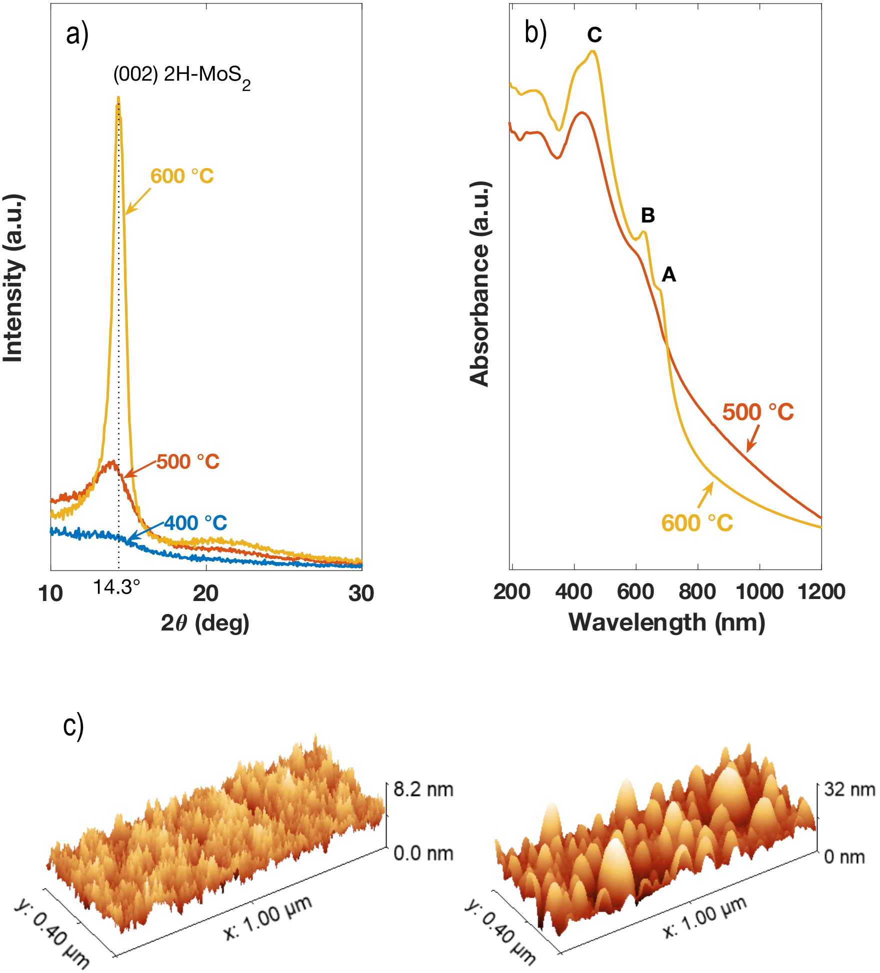

Figure 34: a) XRD patterns and b) UV-VIS-NIR absorbance spectra of MoS$_2$ films fabricated on silica substrates and treated at different temperatures. Reprinted with permission from [9]. 2022, Elsevier B.V. All rights reserved. c) AFM measurement performed on MoS$_2$ films treated at 500°C (left) and at 600°C (right).

2.2.4 Device characterization

Photodetectors based on the fabricated MoS_2 films were fabricated to demonstrate the employment of the described method for optoelectronic applications. The device was fabricated on a soda-lime glass substrate, engineered with gold electrodes as described in 2.1.6. Although it has been observed that a 600°C thermal treatment would improve the material quality (see above), the devices were treated at 500°C not to exceed the maximum temperature for the glass substrate. The selected temperature allows to achieve MoS_2 films with low impurity residuals and discrete optical properties.

Figure 35 (left) shows a device based on a MoS_2 film fabricated on a glass engineered substrate as described above. The film is spread all over the substrate covering a ~ cm^2 area. J-V characterization under dark of the different channels shown in the optical image are reported in Figure 35 (right). The currents show an ohmic behavior and report values of tens of mA/cm^2 at low voltages, indicating high dark currents, attributable to the impurities affecting the expected semiconducting behavior. The values are comparable for the different channels, demonstrating uniformity of the electric film properties across the extent of the engineered substrate.

One of the channels of the device was chosen to be representative for the batch and its photoresponse was characterized in the NUV-VIS-NIR spectrum. A comparison between the J-V curves recorded under dark and under illumination with a 455nm LED (Optical irradiance 3120 $\mu W/mm^2$) is reported in Figure 36(a). The curve acquired under illumination shows an increase of conductivity of a factor ~1.5, demonstrating the photodetection of the MoS_2 film.

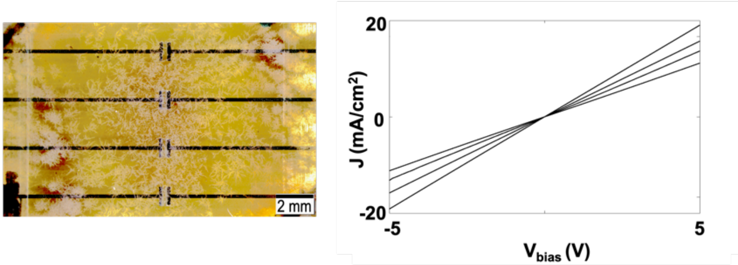

Figure 35: Optical microscope image of a photodetector based on MoS_2 film(right). J-V curves for four channels out of five channels of the device (left). Reprinted with permission from [9]. 2022, Elsevier B.V. All rights reserved.

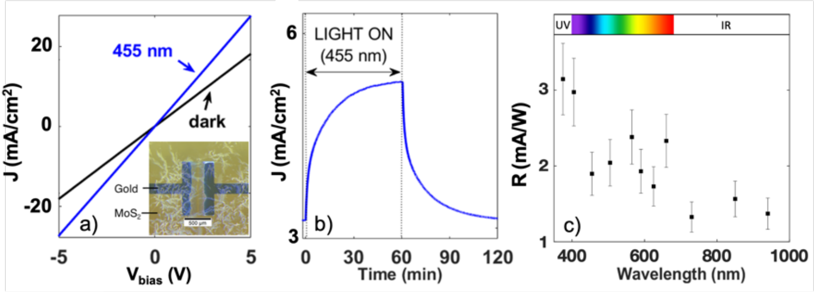

Figure 36: a) J–V curves in dark conditions and under 455 nm light irradiation (power = 94 µW) of a photodetector based on a MoS_2 film obtained with the sol-gel process proposed. In the inset, the channel of the fabricated device is shown. b) Time response of the detector under a switching light at 455 nm with applied bias voltage of 1 V. c) Responsivity of the detector to different wavelength radiations with an applied voltage bias of 1 V. Reprinted with permission from [9]. 2022, Elsevier B.V. All rights reserved.

The temporal response of the photodetector is reported in Figure 36(b) for the same irradiation (455 nm, 3120 µW/mm^2) and applied voltage bias of 1V. The curve is characterized by a slow rise and decrease time, with the device taking around 1h to reach a stable signal. After switching off the light the signal eventually returns to the dark state in few hours and the behavior can be reproduced. This behavior can be explained by a considerable carrier trapping effect, as already observed in previous works [132]. This is associated with defects of the materials, as discussed above. This feature puts a limitation of the use to low frequency applications. A potential improvement of the device speed may be obtained with a smarter choice of the device architecture, preferring interdigitated geometries of the electrodes to maximize the active area, as well as vertical structures, to reduce the channel length. No significant aging effect was noticed in six months of use, keeping the samples in dark and exposed to ambient air.

Eventually the device response was characterized in terms of responsivity in the NUV-VIS-NIR spectrum. Figure 36(c) shows the responsivity values of few mA/W at V_b of 1V in all the spectrum considered. The spectral response displays an increased response in the NUV spectrum and shows a tail of response to the NIR region, in accordance with the absorbance spectra shown in Figure 34(b). This extends the range of response that is expected for MoS_2-based detectors, generally limited to the UV-VIS spectrum. Detection of IR radiation is associated with the defects present in the material allowing population of forbidden energy states, and photogeneration from longer wavelength radiations. The responsivity value around 660 nm is attributed to an increased absorption due to the proximity to the excitonic energies of MoS_2, as shown in the absorbance spectrum. Preliminary tests were performed with X-rays in a similar way as described below for the device fabricated via MoS_2 exfoliation (see Chapter 3), but no response was detected. This is attributed to the large dark currents exhibited by the device (see Figure 36(a)) which result in a low light to dark ratio when the device is irradiated.

These results demonstrate a method to obtain large area MoS_2 films and a photodetector is here shown as a proof of concept of the use of these films for optoelectronic applications. Alongside with these novelties, the presented device still suffers from low performance, attributed to a certain degree of impurity and oxidation of the film, driving the detector response. Ameliorations of the material must be achieved in order to build a prototype of a commercial device. Material improvement may be achieved by modifying the synthesis substituting the current chelating agent (DTPA) in favor of one which is more easily removable at low temperatures. Without modifying the synthesis precursors, higher quality films can be obtained with thermal annealing at higher temperatures. Higher temperatures will indeed reduce the organic impurity content, promote crystallinity, and improve the optoelectronic properties of the film (see above). Nevertheless, the devices must be fabricated only on substrates stable at high temperatures. The choice of the substrate will be further limited considering that oxide containing substrates are prone to oxygen diffusion and may induce oxidation of the MoS_2 film, as discussed above. For these reasons, fabrication of pure and highly crystalline MoS_2 films directly on the final substrate severely limits the versatility of the proposed method.

2.3 Towards high quality MoS_2 films for flexible photodetectors

As discussed above, a possible solution to this problem might rely in fabricating the MoS_2 films on oxide free substrate performing higher temperature thermal treatments. To overcome the drawback of the process deriving from the limited choice of the substrates, a subsequent transfer of the film can be performed. Figure 37 depicts the steps of the strategy we propose. The strategy takes inspiration from the transfer method described below in section 3.1.2 that showed successful results in the case of the transfer of a MoS_2 monolayer.

The MoS_2 film is fabricated on a sacrificial oxide-free substrate (e.g., native Si) via a thermal treatment at high temperatures (900-1000°C). A polymethyl methacrylate (PMMA) solution (5% wt. in toluene) is spin-coated on top of the sample (3000 rpm for 1 min) to embed the MoS_2 film and add mechanical stability for the following transfer. Afterwards, the substrate onto which the MoS_2 has been fabricated is etched

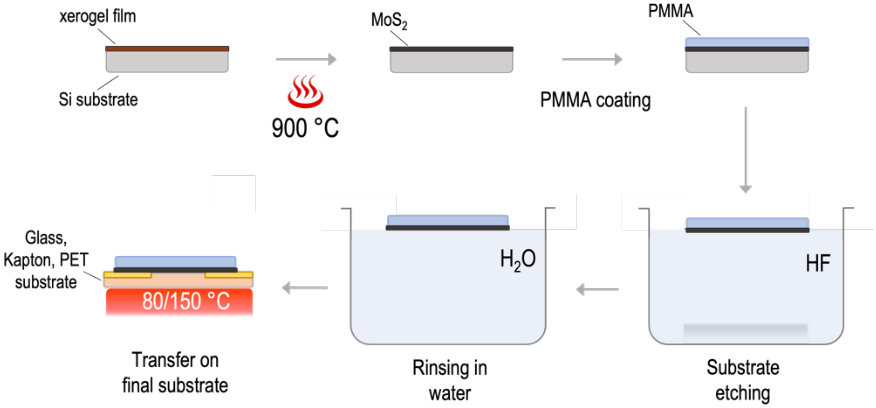

Figure 37: Strategy to obtain flexible detectors based on high quality MoS_2 films, via high temperature treatment on oxide free substrates and subsequent transfer of the film on a final substrate.

leaving a MoS_2 film embedded in PMMA. Etching can be performed in a solution of hydrofluoric acid (HF), and PMMA is chosen because of its resistance to the HF acid. Once the substrate is etched, the MoS_2 film can be transferred a few times in beakers containing deionized water to clean it from acid residuals. Eventually the film is transferred on the desired engineered substrate, being it based on glass, Kapton, PET, etc., and low temperature treatments (1h at 80°C and 30 min at 150°C) are applied to evaporate the residual water and make the PMMA to adhere to the substrate, keeping the MoS_2 film in contact with the electrodes. If removal of the PMMA layer is needed, cleaning with toluene is used. This approach might lead to higher quality MoS_2 films on the desired substrate, keeping the fabrication versatile on a vast choice of substrates, including flexible ones.

The method was applied to a MoS_2 film previously fabricated on silica and we succeeded in etching the former substrate and transfer the MoS_2 film on a flexible substrate. This is depicted in Figure 38, where a MoS_2 film treated at 500°C, previously fabricated on silica, is shown embedded in PMMA after the transfer on a PET substrate. The MoS_2 film tolerated the etching and transfer procedure and sticked to the PET substrate. This thanks to the PMMA layer protecting it from to too long acid exposure and adding mechanical stability to the film.

This result, although preliminary, is promising since it paves the way to a more versatile fabrication method that might overcome the drawbacks related to the limited quality of the obtained MoS_2 films. Further studies must indeed be performed to demonstrate the maintenance of the MoS_2 structural and chemical properties during the process and the operability of the so fabricated devices. Eventually, optimization

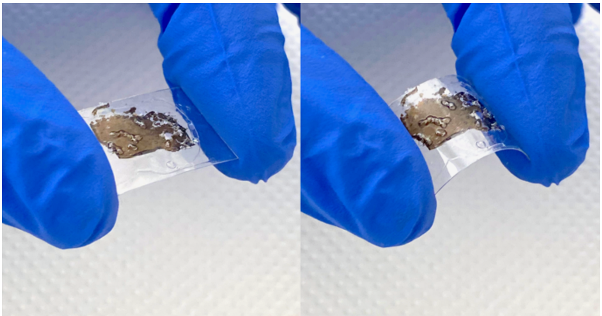

Figure 38: MoS_2 film embedded in PMMA after the transfer on a PET flexible substrate

of the device might be obtained by choosing a smarter geometry for the electrode layout in the engineered substrate. Solutions might rely in the use of interdigitated electrodes with large active area and small distance between the electrodes.

2.4 Conclusions

This chapter described the work performed regarding the production of large area MoS_2 films via a facile, scalable and environmentally sustainable sol-gel process and their use in photodetector for the UV-VIS-NIR spectral range.

Starting from a previously reported sol-gel recipe for the production of MoS_2 [7], the study optimized the recipe to obtain large and uniform MoS_2 films to be exploited in actual devices. With the original recipe it was not possible to cover uniformly the substrates, due to a poor spreading of the solution. With the addition of 2-butanol in the synthesis medium, the uniformity and the area of the film were drastically improved, thanks to a better wetting of the substrate. The hydroalcoholic solution allows to fabricate ~cm^2 size MoS_2 films on several substrates (silicon, silica, gold, glass), and this was confirmed by optical images and Raman spectroscopy measurements. The films morphology was investigated with SEM microscopy techniques, showing uniform film areas of mm^2 and thickness about 200 nm. The film stoichiometry was analyzed by means of XPS spectroscopy, confirming the MoS_2 structure. Besides, the survey spectrum revealed carbon residues, attributed to a non-complete decomposition of the organic residues, and traces of oxide species, associated to partial oxidation of the MoS_2 film. XRD spectroscopy revealed a poor level of crystallinity of the MoS_2 films treated at 400°C, ascribable to presence of a significant amount of DTPA, as suggested by thermogravimetric analysis. The crystalline structure is improved at temperatures of 500°C or higher. Optical absorption spectroscopy in the NUV-VIS-NIR spectrum elucidated the optoelectronic properties of the film, demonstrating a behavior compatible with the one expected for two-dimensional MoS_2. However, the film showed absorption that extends also in the NIR spectral range, that are associated to the impurities previously observed, narrowing the bandgap of the material.

The films treated at 500°C were employed in photodetectors as a proof of concept of their use in actual devices. The detector showed a responsivity in the mA/W range in a wide spectrum, from NUV to NIR, demonstrating the applicability of the method in optoelectronics. The response of the detector in the NIR spectrum agreed with the optical absorption experiment. The detector showed a slower response to light, compared to previously reported MoS_2-based photodetectors, attributable to charge carrier trapping centers, originating from the residual material impurities. The device performance will benefit from the optimization of the device electrode architecture, in favor of designs with closer electrodes and larger active areas, but the quality of the material must be improved to produce sufficiently high-quality devices.

A potential solution to increase the material quality without distorting the synthesis process relies in the use of thermal treatment of the films at higher temperatures to remove the impurities and improve the film crystallinity, prior to transfer the obtained MoS_2 film on the desired final substrate. This might open the way towards the production of flexible devices with this method.

Although in the work presented here the material shows some critical points that require further optimization, interesting steps have been performed towards the production of MoS_2 films with a simple and scalable sol-gel method. The produced films are indeed characterized by large areas, good morphology, and uniformity, thanks to the addition of 2-butanol in the synthesis medium. Moreover, this method demonstrated then its applicability in the field of optoelectronics with the production of working, though improvable, photodetectors. Eventually, it was observed that the temperature required to obtain higher quality MoS_2 films severely limits the choice of the substrates. Preliminary results suggest that an intermediate transfer of the film on the final substrate may help in making the process more versatile, opening the way for future work related to this topic.

Chapter 3: MoS_2 photodetectors fabricated via exfoliation for X-ray detection

A second observation raised in the introduction, is that the photodetectors based on 2D-MoS_2 reported so far have focused on the detection of the UV-VIS-NIR electromagnetic spectral range. Interesting, although MoS_2 possess a high cross section for X-rays, due to the high atomic number Z of Mo, and the exploration of the higher energy electromagnetic spectrum is still missing. Aim of this chapter is to present the experimental activity performed during the project to explore the X-ray detecting capabilities of 2D-MoS_2. For the purpose a photodetector based on a MoS_2 monolayer (1L-MoS_2) was fabricated via mechanical exfoliation and characterized in a wide range of the electromagnetic spectrum, from the NIR to X-rays up to 10^2 keV. This demonstrated for the first time the use of MoS_2 as material for direct ionizing radiation detection and opens the way to the study of 2D-MoS_2 and TMDCs for applications related to X-ray detection, such as in-vivo dosimetry.

In the “materials and methods” section we outline the procedure of exfoliation of 1L-MoS_2 from the bulk MoS_2 crystal and we describe the detector fabrication. Afterwards, the experimental results are discussed in the “results and discussion” section. The experimental results confirmed the good response of 1L-MoS_2 in the UV-VIS spectrum. The characterization of the device under X-rays in the 10-10^2 keV is then reported, demonstrating for the first time a response of 1L-MoS_2 associated to a direct conversion of X-rays into charge carriers and showing the great potential of MoS_2 for X-ray detection applications. Eventually the photodetector was combined with a thin scintillator film, which resulted in an increase of the response of the device to X-rays up to three times, showing a possible strategy to improve the device response to X-rays. The chapter concludes with a section presenting a preliminary characterization of the detector irradiated with a 100 MeV proton beam, showing encouraging results. Conclusions on this work are finally presented leaving room for potential future works that may take inspiration from this study.

3.1 Materials and methods

3.1.1 Exfoliation from bulk MoS_2

The exfoliation from MoS_2 bulk crystal was accomplished via a thermally activated metal mediated process. A full description of the exfoliation process can be extracted from our previous reports [47–49].

The process is illustrated in Figure 39. i) An ultraflat clean gold surface is obtained over which the parent MoS_2 crystal will be joined. This is obtained via thermal evaporation of ≈100 nm of gold on top of a previously cleaned polished Si wafer (<100>, Siegert Wafer, Germany). Subsequently, a thicker layer of Cu (≈ 1 μm) is deposited on top of gold via the same process. Glass slides were finally glued onto the copper layer (Encapsulation Epoxy S132, Ossilla, UK) and UV cured for 1.5 h. From this stage the process is performed in a flow hood to reduce surface contamination. After that, the glued glass slides are flipped with the help of a razor blade revealing a fresh and ultraflat gold surface. ii) The parent MoS_2 crystal is sticked to the gold surface and make it to adhere by simple mechanical pressure of the operator on the Kapton tape. iii) A heating step at 200 °C for 60 s on a hotplate is performed to promote the adhesion of MoS_2 to gold. iv) The parent MoS_2 crystal is easily removed by pulling the Kapton tape, leaving a monolayer attached to gold thanks to weak van der Waals interactions between MoS_2 layers.

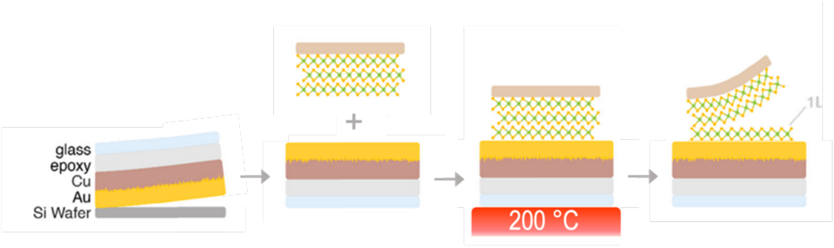

i) ii) iii) iv)

Figure 39: thermally activated metal-assisted exfoliation procedure steps. Adapted from [47]. Creative Commons Attribution CC BY.

3.1.2 Transfer of the exfoliated 1L-MoS_2 and device fabrication

After 1L-MoS_2 is obtained on top of gold, it needs to be transferred a target substrate. The transfer was achieved via a wet polystyrene assisted procedure that is extensively described in a previous report [48]. The procedure is illustrated in Figure 40. i) 1L-MoS_2 on top of gold is covered with polystyrene via spin-coating (average Mw ≈ 280.000, Sigma–Aldrich, USA, 90 mg mL^{-1} in toluol, 3000 rpm 60 s) and the sample was cured at 80 °C for 10 min. ii) The sample was left floating on a metal-etching solution (KI/I_2, Sigma Aldrich, USA) for 12 to 24 h, until the polystyrene foil floats on top of the solution. iii) The foil was scooped with a piece of silicon wafer and transferred in deionized water. The procedure was repeated 4 times to remove the etchant residuals. iv) The foil was finally scooped from water with the target substrate and let dry overnight, before baking it first at 80 °C for 1h and at 150 °C for 30 min, obtaining 1L-MoS_2 on top of the substrate embedded in polystyrene. The polystyrene layer was left on top of MoS_2 as protective layer.

We obtained an average yield of 2.5 out 5 working devices per substrate, for a total of 10 out 20 working devices. The yield is associated with the dimensions of the exfoliated crystals that could not cover the entire glass sample and to the uneasy handling of the exfoliated layers in the transfer process which might lead to material damage.

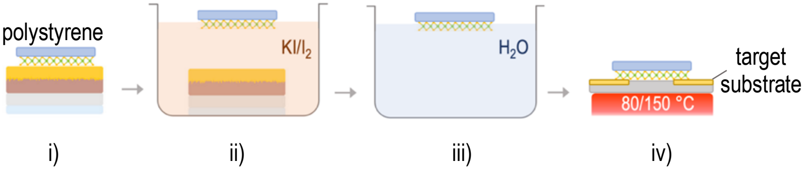

Figure 40: wet polystyrene assisted 1L-MoS_2 transfer steps. Adapted from [48]. Creative Commons Attribution CC BY.

The fabrication of the device followed the exfoliation/transfer technique that is reported above. The target substrate used for the transfer was the engineered glass substrate with gold electrodes reported in section 2.1.6. The transfer was finalized with the help of an optical microscope to align the monolayer area of the exfoliated MoS_2 layer with the channel of the engineered substrate.

3.1.3 Gd_2O_2S:Tb based scintillator synthesis

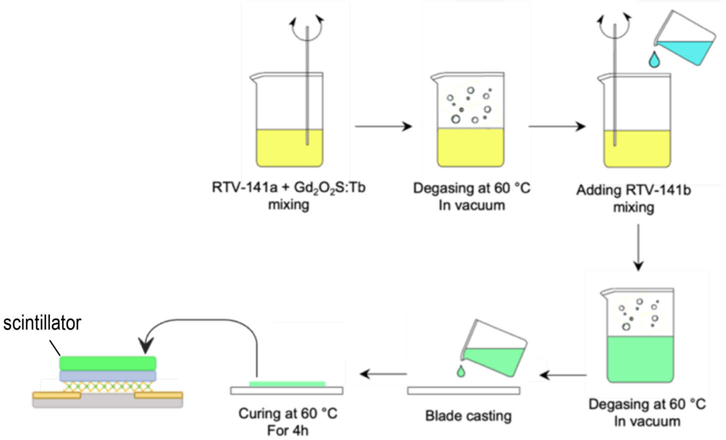

Figure 41: scheme of the steps of the fabrication of scintillator films based on PDMS loaded with Gd_2O_2S:Tb.

To increase the response of the device to X-rays, a plastic scintillator based on gadolinium oxysulfide doped with terbium (Gd_2O_2S:Tb) was fabricated and applied on top of the MoS_2 based photodetector described in section 3.1.2.

The scintillator was fabricated following the procedure illustrated in Figure 41. Gd_2O_2S:Tb powder (UKL65/F-R1, Phosphor Technology Ltd., UK) was added (0.5% wt) to the base PDMS component (Bluesil^{TM} RTV 141-a, Elkem Silicones, Norway), mixed and degassed in a vacuum oven at 60 °C. The reactive PDMS component

(Bluesil™ RTV 141-b, Elkem Silicones, Norway) was added in a 10:1 mass ratio with respect to the base component, followed by degassing in a vacuum oven at 60 °C. Finally, the mixture was casted via blade casting and cured at 60°C for 4 hours. A film (0.2 mm thick), flexible and almost transparent was obtained, from which the portion needed was cut and applied on top of the 1L-MoS_2 based photodetector.

3.1.4 Characterization techniques

For the properties of the exfoliated 1L-MoS_2 we refer to the previously reported reports [47,48]. The functioning of the fabricated devices was initially checked by acquiring their temporal photoresponse to illumination with a 455 nm LED light (Thorlabs, USA). This was measured with a device selector board (Ossilla, UK) connected to a Keithley 2450 source measurement unit (Tektronic, USA). After checking for the correct functioning of the detectors, a device was chosen to be characterized in electromagnetic spectrum. The 1L-MoS_2 based photodetector chosen for the purpose was characterized in the NUV-VIS-NIR spectrum in a similar way to what it has been described in Chapter 2 for the device fabricated via sol-gel synthesis (section 2.1.7). Current density-voltage curves (J-V), temporal response to illumination, and photoresponse were measured with the device selector board. Illumination in the NUV-VIS-NIR spectrum was provided with different LEDs (Thorlabs, USA) placed at 200 mm from the detector. The list of the LEDs employed for this experiment with their main properties is reported in Table 6. The light power on the detector channel was estimated multiplying the nominal irradiance of the LEDs at 200 mm (reported in the datasheet) by the area of the channel (0.03 mm^2). The irradiation of the channel area was assumed to be uniform in the experiment. The J-V curves were acquired between -5 V to 5 V in dark and under constant illumination of a 455 nm LED with optical power of 0.94 µW on the channel. The temporal response of the device was evaluated by measuring the current density as a function of time while the channel was exposed to a square wave 455 nm light (10 s at 0.094 µW, 10 s in dark). To calculate the response as a function of the optical power, neutral-density filters (Thorlabs, USA) were used. Responsivity was calculated by normalizing the photoresponse by the optical power illuminating the channel, applying a voltage bias of 1 V. The device was also characterized under illumination of X-rays to prove the use of 1L-MoS_2 as material for direct radiation detection. Uniform irradiation of the detector was obtained in a RS225 Xstrahl irradiation cabinet (Xstrahl, UK). X-rays were generated with a tungsten anode (W_{K_α} = 59 keV) operated at voltages of 40 kV, 100 kV, 150 kV, 195 kV, using emission currents from 2 mA to 18 mA. The X-ray spectrum was filtered with a slab of 3 mm of copper. The X-ray source was operated at different voltages as a strategy to achieve dose rates varying on three orders of magnitude. Doses and dose rates to water were measured thanks to a 30010/12 Farmer© ionization chamber connected to a PTW UNIDOS E electrometer (PTW, Germany), and adopted as dose references for the subsequent irradiating the detector, which was placed in the same position of the ionization chamber. X-ray response was measured for both the photodetector based on MoS_2 only and adding the scintillator on top of the detector channel. In the measurement, the background arising from the irradiation of the electronic equipment was subtracted. The polystyrene layer thickness was measured with a DektatXT profilometer (Bruker, USA) to be ≈ 1 µm and it was estimated to absorb less than 0.01% of the x-rays used. The scintillator based on PDMS and mixed with Gd_2O_2S:Tb (0.2 mm thick) can absorb up to 4% of the radiation (based on NIST database[85]). Radiation sensitivity of 1L-MoS_2 was calculated via equation (1).

The detector was tested under 100 MeV proton irradiation to demonstrate its use with other types of ionizing radiation. Proton irradiation was performed in the experimental room of the Trento (Italy) proton therapy facility. Protons were produced with a cyclotron (Proteus 235, IBA, Belgium) installed at the facility. Protons at 100 MeV were selected at the exit of the cyclotron thanks to an energy selection system (ESS). The extraction currents were 1nA, 10nA and 100 nA, which resulted in proton rates in the range 10^7-10^9 protons/s. The proton flux was measured with a MINI-Q (DE.TEC.TOR), composed of a stack of ionization chambers. The proton beam has a beam spot with a gaussian distribution (σ_x = 5.6 mm, σ_y = 5.7 mm) at 1.25 m from the beam exit (isocenter). The detector was placed perpendicular to the beam at the isocenter position [133]. The gaussian profile of the beam was used to estimate the effective proton rate irradiating the active area of the detector.

Table 6: Thorlabs LEDs models, nominal wavelength, and irradiance on the detector.

LED Model	Wavelength (nm)	Irradiance (μW/mm^2)
M340	340	2.22
M375L4	375	13.71
M405L4	405	14.53
M455L4	455	31.20
M505L4	505	11.10
M565L4	565	11.70
M590L4	590	5.30
M625L4	625	18.00
M660L4	660	17.41
M730L4	730	13.20
M850L4	850	19.08
M940L4	940	19.10

3.2 Results and discussion

3.2.1 Device fabrication

In Figure 42(a) a top-view of a device acquired with an optical microscope is reported. The picture shows a MoS_2 flake lying on a glass substrate. The two black branches separated in the middle of the picture are the thermally evaporated gold anode and cathodes. The MoS_2 monolayer area corresponds to the yellowish region that has been delimited by a dashed line to facilitate the recognition. The darker features in the flake represent instead multi-layer MoS_2, as already observed in previous reports [47,48]. We can observe that the monolayer area of the flake entirely covers the channel area. Therefore, the active area of the detector was assumed to equal the area of the

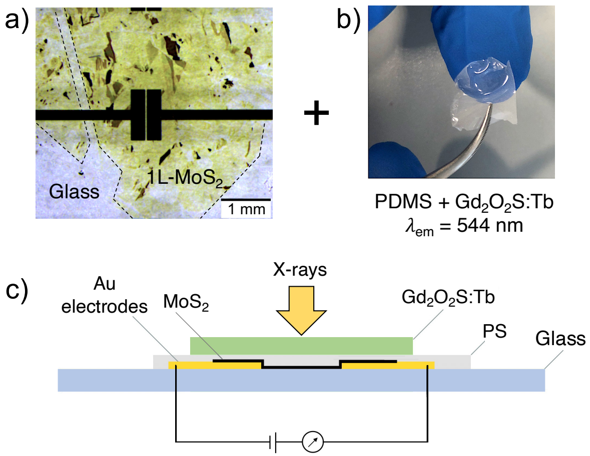

Figure 42: a) Optical image acquired with a microscope of the top-view of the X-ray detector device based on 1L-MoS_2. The dashed line delimiting the yellow area is a guide for the eye to identify the MoS_2 monolayer. The two black features in the middle are the electrodes defining the active area in the channel between them. b) Image of the scintillator film based on PDMS and loaded with Gd_2O_2S:Tb that is applied on top of the device. c) Schematic cross-section of the final device.

channel (0.03 mm^2). The thickness of the active region was assumed to be 0.9 nm, as previously observed for 1L-MoS_2 fabricated with this method [47]. It is worth noticing that this thickness is larger than the thickness reported for 1L-MoS_2 (0.65 nm) [134]. This is attributed to the van der Waals interaction between the 1L-MoS_2 and the substrate.

3.2.2 UV-VIS-NIR characterization

The photodetector based on 1L-MoS_2 was initially characterized in the NUV-VIS-NIR spectrum. Figure 43 (a) reports the J-V curves acquired in dark and under illumination of a 455 nm LED light (Optical power 940 nW). The device displays dark current densities as low as ~10^{-1} μA/cm^2 at voltage bias V_{bias} < 1V. The currents show an increase of a factor 10^2 when the LED light is illuminating the channel, confirming the strong response of the 1L-MoS_2 to visible light, leading to a remarkable ON-OFF ratio of the device. The asymmetric behavior near zero voltage bias of the J-V curve acquired in dark is attributed to a measurement offset that become noticeable at very low currents. The curve acquired under illumination is instead rather symmetrical, as expected for a symmetric device.

The photoresponse of the device as a function of the optical power of the of the 455 nm LED is reported in Figure 43(b). The response follows a power law behavior with the optical power illuminating the active area of the detector, with $R \sim P^n$, n = 0.6. This is attributed to a photoconductive gain mechanism that lowers the response when the illumination power increases [135]. This behavior can be explained by a higher probability of carrier recombination when the number of the electron-hole pairs increases. Moreover, the response was measured down to optical powers of 10^{-4} μW, showing the high sensitivity of the device to visible light.

The temporal response of the detector illuminated by 455 nm light (optical power 94 nW, V_{bias} = 1 V) is reported in Figure 43(c). The device response is slower than previously reported devices, with rise and decay times in the order of the seconds (τ_r ~10s). This can be attributed to defects of the 1L-MoS_2, probably due to strains induced on the flake during the exfoliation and transfer procedure. Also, strains can be induced by the free-standing monolayer on the electrodes. The dynamic is expected to improve using smoother substrates and using extra care during the fabrication process.

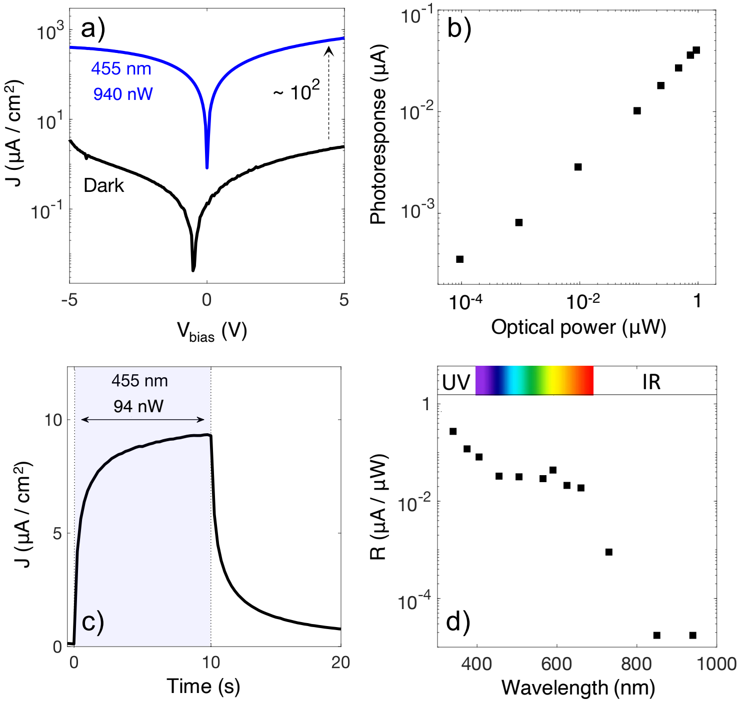

Figure 43: Response of the detector based on 1L-MoS$_2$ in the near visible spectrum: a) the J-V curves was measured in the dark and upon illumination with a 455 nm LED are shown. b) Photoresponse of the detector operated ad 1 V as a function of the LED optical power. c) Time evolution of the photocurrent while operating the device at 1 V by switching the LED on (0 s – 10 s) and off (10 s to 20 s). d) Spectral responsivity in the NUV-VIS-NIR spectrum with the device operated at 1 V.

The responsivity of the photodetector in the NUV-VIS-NIR spectral range is shown in Figure 43(d), when applying a voltage bias of 1 V. The responsivity in the NUV spectrum reaches values as high as fractions of A/W, while it decreases to 10^{-2}-10^{-1} A/W in the visible and drops to negligible values in the NIR spectrum. The higher responsivity value observed about 600 nm is associated with the increased absorption of 1L-MoS_2 around its exitonic energy. The spectral response shown here demonstrates the strong response of the photodetector in the NUV-VIS spectral range and agrees with the absorption spectrum expected for 1L-MoS_2. [28]

The device showed no degradation after testing with UV-VIS light, and the dark current eventually returned to the pre-irradiation values. No significant aging effects were observed after tests performed over a year of use. This can be associated also to the polystyrene layer acting as a protective layer.

Comparing these results with similar experiments described in Chapter 2 in the case of a photodetector based on MoS_2 thin films obtained with a wet chemical synthesis, points out the superior performance of the device based on exfoliated 1L-MoS_2. The device described in this chapter shows performance in terms of ON-OFF ratio, response time and spectral responsivity which are orders of magnitude higher. This is associated with the superior quality of the crystal obtained by exfoliation, suggesting that further optimization needs to be carried out in the wet chemical synthesis approach.

As mentioned earlier, the exfoliation/transfer procedure described in this chapter is suitable to be applied also for the fabrication of detectors on flexible substrates. An example of a device fabricated on an engineered substrate based on Kapton with the described method is reported in Figure 44. The temporal response shown, although it is a preliminary result, demonstrates that the response to light is similar to the one obtained on glass substrate and suggest the use of this method to develop flexible detectors. Further characterization of the device, from both an optoelectronic and mechanical point of view might demonstrate the feasibility of the method for flexible and wearable applications.

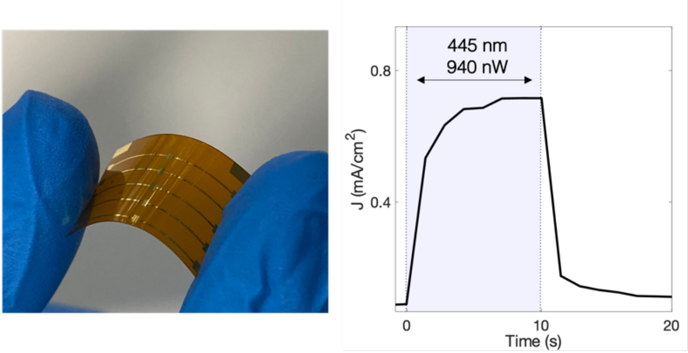

Figure 44:Flexible engineered substrate based on Kapton with gold electrodes (left).Temporal response curve of the device when illuminated with a 455 nm light (Optical power 94 μW) and voltage bias of 1 V (right).

3.2.3 X-ray characterization

The detector based on 1L-MoS_2 fabricated on the engineered glass substrate shown in Figure 42(a) was characterized under X-rays to demonstrate the use of 1L-MoS_2 as material for direct X-ray detection. Figure 45 compares the response of the device based on 1L-MoS_2 (black markers) and of the same device after the addition of the thin scintillator based on PDMS blended with Gd_2O_2S:Tb (green markers), for different X-rays energies used. The contribution to the signal arising from the irradiation of the bare substrate with the electrodes (see Figure 46(d)) was subtracted in the following to obtain the response of the active materials only. For all the energies used, the detector based on 1L-MoS_2 shows a response that increases almost linearly with the delivered X-ray dose rate. This demonstrated for the first time the direct X-ray conversion acted by MoS_2, showing current densities in the order of the μA/cm^2. With the experimental setup it was possible to measure dose rates as low as 0.08 mGy/s. The two-dimensional nature of the 1L-MoS_2 also leads to negligible perturbation of the X-ray radiation field, fundamental requirement to move to in-vivo applications.

The addition of the scintillator film on top of MoS_2 is found to boost the signal for all the energies used, with a photocurrent increase of up to three times. The increase of the response is associated with the production of visible photons (centered at λ=533 nm) via indirect X-ray conversion mechanism acted by the scintillator that illuminate the underlying 1L-MoS_2. The recorded signal is therefore the result of the collection of charges generated in the MoS_2 by direct conversion of X-rays and by visible photons generated by the scintillator. The scintillator is estimated to absorb from 1 to 4% of the X-ray radiation, depending on the X-ray energy used, based on the attenuation coefficients reported in the NIST database [85]. The increase of the detector response is significant even if the absorption of radiation in the scintillator is almost negligible. This is due to the strong response of the 1L-MoS_2 in the visible spectrum, as seen above (Figure 43(d)).This result shows a possible strategy to increase the detector response, while keeping the absorption of X-rays very low and thus with minimal perturbation of the radiation field. Further engineering of the scintillator to maximize the detector conversion efficiency will lead to even larger response. The non-linearity of the detector response with the dose rate is attributed to the non-linear output of the scintillator, ascribable to the quenching of the scintillation mechanism increasing the dose rate. The highest photocurrents are observed with radiation generated at 100 kV.

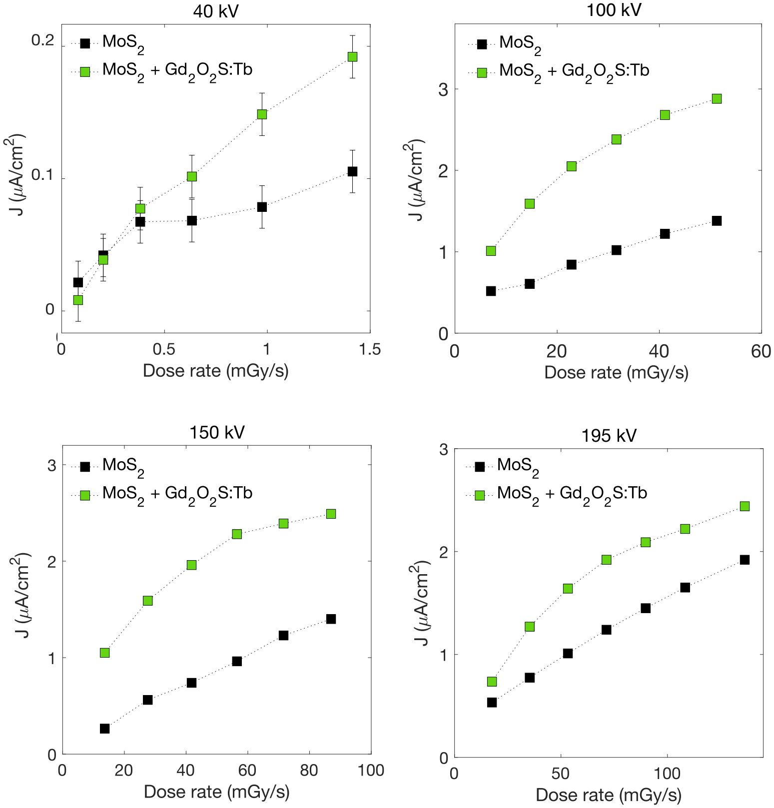

Figure 45: Photocurrent density as a function of the X-ray dose rate operating the source at different voltages, namely 40 kV, 100 kV, 150 kV, 195 kV. The black markers correspond to the 1L-MoS$_2$ based device while the green markers correspond to the device incorporating the scintillator film based on Gd$_2$O$_2$S:Tb. The contribution to the signal from the bare substrate with the electrodes was subtracted in the calculation. The error bars are displayed on the graph relative to the 40kV irradiation only, where the fluctuations of the measure are not negligible compared to the recorded signal. For the higher energy irradiations, the uncertainty is included in the marker chosen for the representation and the error bars are not displayed for graphical purposed. The detector was operated at 5 V during these acquisitions.

This is more clearly depicted in Figure 46(a), where the J-V curves obtained with different X-ray energies for the device based on 1L-MoS_2 incorporating the scintillator are plotted in the same graph.

Although the dose rates achievable with X-rays produced at 40 kV are too low for a direct comparison with higher energies, it is possible to compare the response obtained at similar dose rates changing the X-ray generating voltage from 100 kV to 195 kV. The graph shows that the highest photoresponse is obtained with 100 kV and decreases when the X-ray energy increases. This is due to a combination of direct response acted by 1L-MoS_2 and indirect conversion acted by the scintillator. The contributions of the 1L-MoS_2 and of the scintillator are plotted in Figure 46(b) and (c), respectively. The contribution of the scintillator was obtained by subtraction of the response from 1L-MoS_2 based device from the response of the device incorporating the 1L-MoS_2 plus the scintillator, considered the minimal absorption of X-rays in the scintillator. The response is found to increase for lower X-ray energies, due to higher absorption from both MoS_2 and Gd_2O_2S:Tb (based on data reported in the NIST database [85]). Figure 46(c) shows the saturation of the response when increasing the dose rate for the device incorporating the scintillator. The saturation is associated to quenching of luminescence centers increasing the dose rate and therefore a saturation of the light emission from the scintillator. Oppositely, the contribution of 1L-MoS_2 to the response is linear with the dose rate. The contribution to the signal arising from the irradiation of the bare substrate with the electrodes is reported in Figure 46(d) and it is associated to charge generation in the insulating channel acted by X-rays.

Figure 47 shows the temporal response of the detector incorporating the scintillator when it is subject to subsequent short (20s) irradiations (topmost figure) and when it is subject to a longer irradiation (15 min) (bottommost figure). The test demonstrated good consistency of the signal during subsequent irradiations. However, the response speed of the detector when it is irradiated needs to improve (τ_r ~20s). The time needed to return to the initial current values is even higher since it might be affected by prolonged phosphorescence mechanisms. Also, the stability of the signal is good when the detector is subject to constant irradiation over time. No degradation of the device was observed after irradiating the device with total doses in the in the 10-10^2 Gy range. Further experiments are required to check for the stability of the device when irradiated with and higher total doses (10^2-10^3 Gy) and understand the radiation tolerance of the device. No significant aging effects were observed until now for the device after the last year of use. This can be also attributed to the presence of the polystyrene film, acting as a protective layer for the 1L-MoS_2.

These results prove direct X-ray detection from 1L-MoS_2 in an actual device, demonstrating for the first time the use of TMDCs for direct X-ray detection.

Furthermore, the work suggests a strategy to improve the detector response through the application of a thin scintillating film based on PDMS loaded with Gd_2O_2S:Tb. The addition of the scintillator can boost the response of the device up to three times with minimal absorption of X-rays, necessary requirement to move to in-vivo applications. Finally, the versatility of the fabrication method on flexible substrate can lead to the production of such detectors on Kapton substrates, achieving ultra-thin and flexible X-ray detectors that might be used for in-vivo applications. Further work in this direction must be performed to realize an in-vivo dosimeter prototype.

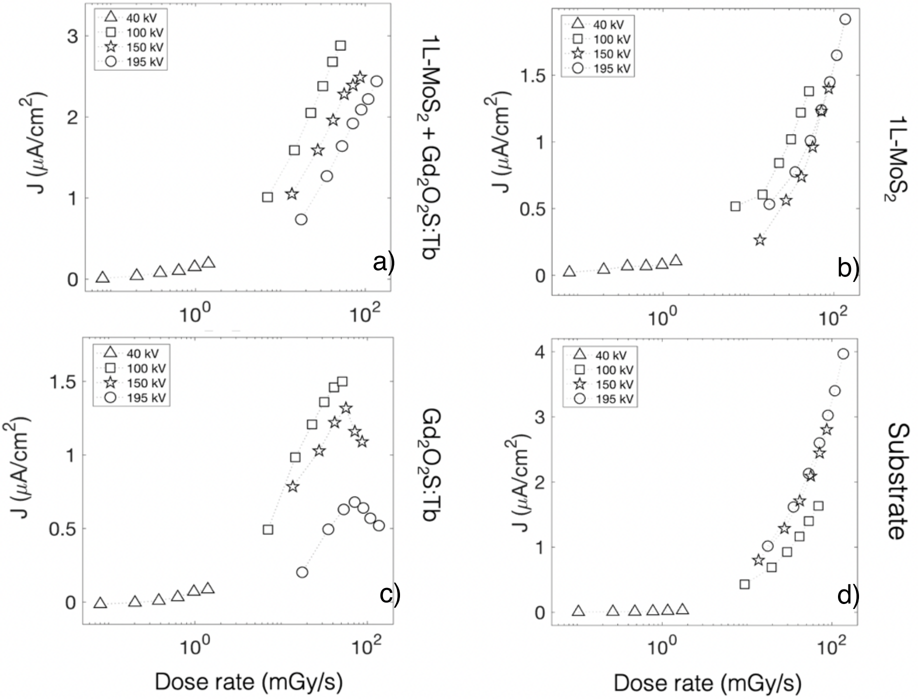

Figure 46: a) Photocurrent densities plotted against the dose rate for the detector based on 1L-MoS$_2$ with the addition of the scintillator film based on Gd$_2$O$_2$S:Tb, for different X-ray energies. b) and c) Contributions to the photocurrents from the 1L-MoS$_2$ and from the scintillator, respectively. The detector was operated at 5 V during these measurements. In these graphs, the contribution to the measure from the irradiation of the substrate was subtracted. d) Contribution to the signal from the irradiation of the substrate.

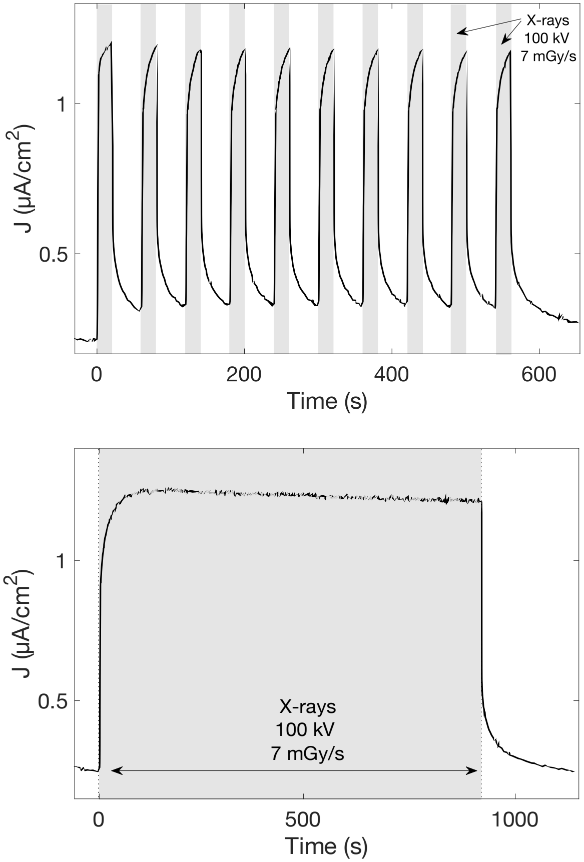

Figure 47: top: Output of the detector incorporating the scintillator when subject to subsequent irradiations of 20 s (top) and to a 900 s single irradiation (bottom) of X-rays at 100 kV (dose rate 7 mGy/s). The total dose delivered during the long irradiation figure is 6.4 Gy.

3.2.4 X-ray Sensitivity

As described in section 1.2.3, an important feature used to compare materials performance under X-rays is the X-ray sensitivity. X-ray sensitivity is indeed used to characterize the material's efficiency in converting directly X-rays to electrical signal and represents the total photogenerated charge normalized for the material's active volume and for the dose delivered. We calculated the sensitivity using equation (1) reported in section 1.2.3.

The X-ray sensitivity plotted against the dose rate for the different X-ray energies used is shown in Figure 48. The calculated values are in the range 10^8-10^9 $\mu C \cdot Gy^{-1} \cdot cm^{-3}$ (area sensitivities vary from 10 to 10^2 $\mu C \cdot Gy^{-1} \cdot cm^{-2}$) with a maximum of $(2.3 \pm 1.7) \times 10^9$ $\mu C \cdot Gy^{-1} \cdot cm^{-3}$. The reported values might have been underestimated by up to 30%, due to the considered 1L-MoS_2 thickness, which is larger than the values reported in the literature, because it includes the van der Waals interaction distance between the monolayer and the substrate. Nevertheless, these values are comparable with the recently reported record for an organic based direct X-ray detector [113]. Also the X-ray sensitivities found here are 2-3 orders of magnitude larger than the values reported so far for most of the direct organic and inorganic detectors [8,95]. X-ray sensitivity is found to depend on the dose rate, with values that decrease when increasing the dose rate. This can be attributed to a photoconductive gain mechanism at low dose rates. As mentioned above, the larger is the number of photogenerated carrier, the higher is probability to have recombination. Besides, at similar dose rates the highest sensitivity has been recorded to X-rays produced at 100kV, due to the higher X-ray absorption of MoS_2, compared to X-rays with higher energy components in the spectral distribution.

The sensitivity here reported highlights an extraordinary efficiency of 1L-MoS_2 in converting X-rays to photogenerated charges. This feature combined with the infinitesimal thickness of the MoS_2 monolayer suggests that the use of 1L-MoS_2 for in-vivo dosimetry applications is a convincing alternative to the current organic and inorganic materials employed for similar applications. This is a first successful example of the use of TMDCs in direct X-ray detection and paves the way towards the study of such materials in actual in-vivo applications.

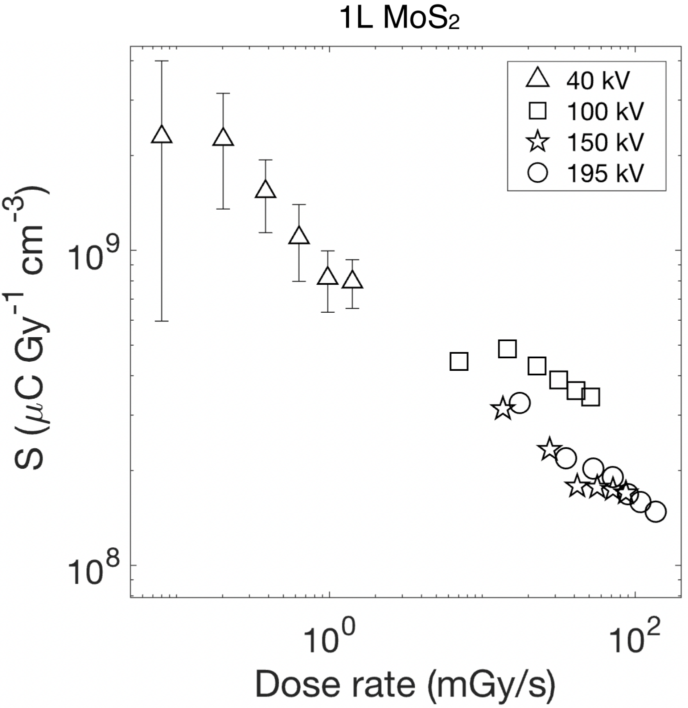

Figure 48: X-ray sensitivity of 1L-MoS_2 varying the dose rate to X-rays produced at different voltages. The detector was operated at 5 V during these measurements. The error bars are displayed for the 40kV irradiation only, where the uncertainty is comparable with the calculated sensitivity value, due to significant fluctuations in the photocurrent measurement (see Figure 45). For the higher energy irradiations, the uncertainty is included in the marker chosen for the representation and the error bars are not displayed for graphical purposed. In the calculation, the contribution to the signal from the irradiation of the substrate was subtracted.

3.2.5 Characterization with charged particles (preliminary results)

The presented work has mostly focused on X-rays for the characterization of the device in the ionizing radiation spectrum. However, other types of radiation are gaining increasing attention in several applications domains. Today, protons are widely employed in experimental facilities as well as in clinic and also the number of facilities dealing with heavy ions (e.g., carbon ions) is growing. Therefore, the device was also characterized under a proton flux as a preliminary test to demonstrate the feasibility of the detector for in-vivo dosimetry applications using other ionizing radiation types. In Figure 49 the response of the device based on 1L-MoS_2 and of the same device incorporating the scintillator based on Gd_2O_2S:Tb to a beam of 100 MeV

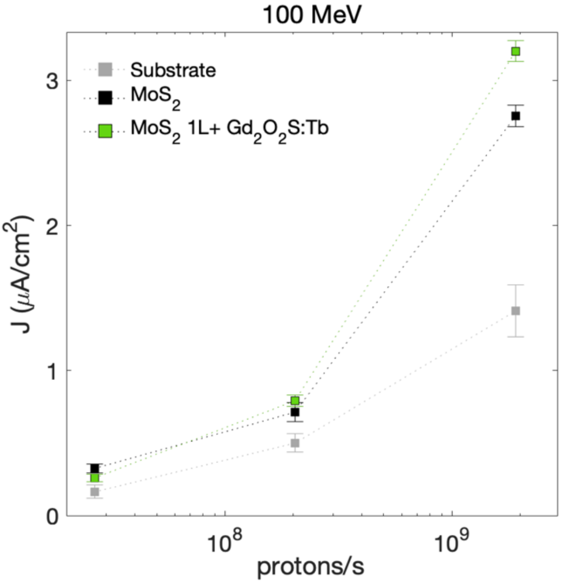

Figure 49: Photocurrent density as a function of the proton rate on the active area of the detector when it is irradiated with 100 MeV protons. The black markers correspond to the 1L-MoS_2 based device while the green markers correspond to the device incorporating the scintillator film based on Gd_2O_2S:Tb. The grey markers represent the contribution to the signal of the bare substrate with the electrodes. The detector was operated at 5 V during these acquisitions.

protons are compared. The response is observed to increase with the proton flux and it is associated to a direct conversion of the proton energy into charge carriers happening in 1L-MoS_2. The photocurrent density recorded reaches values of few μA/cm^2 at the highest proton flux. The scintillator is observed to enhance the signal with respect to the 1L-MoS_2 only of about 35%, due to conversion into visible photons of the energy released by protons in Gd_2O_2S:Tb. This indicates the beneficial role that even a very thin scintillator can have in improving the device response. Further tests must be performed, also varying the proton energy, to confirm the preliminary results shown here.

3.3 Conclusions

This chapter described the fabrication and the characterization of a device based on exfoliated 1L-MoS_2 for the detection of radiations in a wide spectrum, from the visible to X-rays in the 10^2 keV energy range.

The exfoliation procedure was used to fabricate a device consisting of a MoS_2 monolayer lying on top of an engineered glass substrate with gold electrodes and covered with a thin film of polystyrene. The so obtained device was tested as photodetector in the UV-VIS-NIR spectral range. The photodetector showed a strong response to ultraviolet and visible light, in accordance with the spectral response expected for 1L-MoS_2 based devices. The detector showed a light/dark ratio of up to 10^2, and dark currents below μA/cm^2 at low voltages (< 5 V) demonstrating good performance. The dynamics of the detector is still limited and shows response time in the order of the seconds (τ_r ~10s), which might be improved via further engineering of the process. Furthermore, the method was also applied to fabricate a detector on a flexible Kapton substrate, showing promising results for future study in the field of flexible electronics.

The detector fabricated on the engineered glass substrate was characterized under X-rays in the 10-10^2 keV range to prove the use of 1L-MoS_2 as direct X-ray detector material. The detector showed a response to dose rates as low as 0.08 mGy/s that increased linearly with the dose rate, demonstrating direct X-ray detection from 1L-MoS_2. The addition of a thin scintillator based on PDMS mixed with Gd_2O_2S:Tb was found to increase the response up to three times thanks to the conversion of the X-ray energy to visible photons. This indicated an easy strategy to improve the device performance, while keeping the attenuation of X-rays minimal.

The X-ray sensitivity of 1L-MoS_2 was calculated to be in the range 10^8-10^9 $\mu C \cdot Gy^{-1} \cdot cm^{-3}$, outperforming most of the organic and inorganic materials. This represents convincing evidence of the efficiency of 1L-MoS_2 in X-ray detection and suggests further study on TMDCs for this application.

Further experiments must be performed to study the response of 1L-MoS_2 to other radiation types, although a preliminary test with protons gave encouraging results. Finally, the demonstration of the versatility of the method on Kapton substrates is a promising signal for future development of such device on flexible and thin substrates, which is necessary to realize an actual prototype of an in-vivo dosimeter.

Chapter 4: General conclusions

This thesis condensed the work performed during the doctoral project on the fabrication of 2D-MoS_2 and on the potential of this material in the field of optoelectronics. The work focused both on the current issues related to the industrial production of 2D-MoS_2 and aimed to explore applications in which MoS_2 can give a significant contribution. This work led to the publication on scientific journals of two articles [6,9] and to the submission of a third one, which is at the current date (01.07.23) under review.

Chapter 1 aimed to give the reader the framework and the background of the research. It presented an overview on 2D-MoS_2 and on the state of the art of MoS_2-based photodetectors. The chapter continued giving the reader the basis on detection of X-rays and an overview of the X-ray detectors used for in-vivo dosimetry.

Aim of the experiments presented in Chapter 2 was to develop a fabrication strategy for 2D-MoS_2 that could overcome the current limitations in terms of versatility and scalability affecting the current material production processes and wanted to demonstrate the applicability of the method to produce photodetectors.

To recall the questions raised in the introductory chapter, the approach described in Chapter 2 wanted to address the following issue regarding the production of MoS_2 films:

Q1. It is possible to fabricate large area 2D-MoS_2 via a facile, reproducible, and scalable process, that can be used to produce photodetectors?

The following answer can be given:

A1. The production of such films is possible through a wet chemical synthesis. The method we propose exploits a facile hydroalcoholic sol-gel synthesis and films can be obtained by simple spin-coating of the solution on the substrates. Moreover, the process requires a thermal annealing step at low temperatures (500°C), compared to previously reported methods and do not involve sulfurization or hydrogenation steps. This makes the fabrication more affordable, versatile on different substrates and scalable for large production. The fabrication method can be exploited to produce optoelectronic devices, as demonstrated in the case of a photodetector. However, the device shows only moderate performance, ascribable to the still limited quality of the films obtained, suggesting that the method requires further optimization to build competitive photodetectors.

This has been evidenced by the experimental results of Chapter 2 that are here summarized:

As shown in section 2.2.3, the proposed hydroalcoholic synthesis resulted indeed in the fabrication of ~cm^2 size MoS_2 films on different technologically relevant substrates, such as Si, SiO_2, Au and ITO-coated glass. The MoS_2 films showed continuous and uniform areas of several mm^2, and thickness of about 200 nm, as evidenced by SEM microscopy. However, the MoS_2 films revealed traces of carbon species, ascribable to organic residues, and oxide species, attributed to a partial oxidation of the films. This seems to affect both the crystallinity and the optoelectronic properties of the films. To achieve a higher material quality and to improve crystallinity temperatures of 500°C or higher are required.

To demonstrate the applicability of the presented method to produce optoelectronic devices, photoconductors were fabricated via the deposition the MoS_2 films onto engineered glass substrates and by thermal annealing at 500 °C. As discussed in section 2.2.4, the detector showed a responsivity in the mA/W range in a wide spectrum, from NUV to NIR, demonstrating a viable option to build MoS_2-based detectors with a facile, versatile, and scalable method. However, the performance of the detector was affected by material's impurities and poor crystallinity which require further material optimization. A potential solution was indeed proposed in section 2.3 and relies in the fabrication of MoS_2 films on oxide-free substrates, and in the thermal annealing of the film at higher temperatures prior to transfer the obtained films on the desired final substrate. Based on this approach, promising preliminary results were obtained for the fabrication of films on flexible substrates, leaving room for further studies on this subject.

The focus of the experiments reported in Chapter 3 was to demonstrate the use of 2D-MoS_2 in less explored application fields such as radiation detection and in-vivo dosimetry. Aim of the chapter can be summarized by the question:

Q2. Can MoS_2 be used as a direct radiation detection material, and can it be considered as an alternative for in-vivo dosimetry applications?

It is now possible to give the following answer:

A2. 1L-MoS_2 fabricated via exfoliation directly detect X-rays when used in a photodetector and possess outstanding X-ray sensitivity, outperforming most of reported organic and inorganic materials. Also, the 2D nature of the material and the versatility of the proposed method makes the material a convincing alternative to the current materials considered for in-vivo dosimetry applications. Moreover, to boost the response of the device, the direct radiation detection of MoS_2 can be combined with an indirect detection acted by a thin scintillator. Issues regarding the scalability and reproducibility of the fabrication method still need to be addressed, but the results might represent first important steps towards the use of 2D-MoS_2 for radiation detection applications.

The experimental results and the discussion of Chapter 3 supports the answer and they are here recapped:

As described in section 3.2.2, the photodetector based on 1L-MoS_2 fabricated via exfoliation showed a strong response to ultraviolet and visible light, in accordance with the spectral response expected for 1L-MoS_2 based devices. The detector displayed good performance, showing a light/dark ratio of up to 10^2, and dark currents below $\mu A/cm^2$ at low voltages (< 5 V). The fabrication method was also exploited to fabricate a detector on a flexible Kapton substrate and showed promising results for future study in the field of flexible electronics.
The response of the detector to X-rays was instead discussed in section 3.2.3. The detector showed a response to X-rays in the 10-10^2 keV range, increasing linearly with the dose rate, demonstrating direct X-ray detection from 1L-MoS_2, even to dose rates as low as 0.08 mGy/s. The addition of a thin scintillator based on PDMS mixed with Gd_2O_2S:Tb boosted the response up to three times thanks to the conversion of the X-ray energy to visible photons, indicating an easy strategy to improve the device performance. As discussed in section 3.2.4, the X-ray sensitivity of 1L-MoS_2 resulted in the range 10^8-10^9 $\mu C \cdot Gy^{-1} \cdot cm^{-3}$, outperforming most of the organic and inorganic materials. This proved the excellent efficiency of 1L-MoS_2 in the detection of X-rays and suggests further study on the use of TMDCs for this application. Further experiments must be performed to study the response of 1L-MoS_2 to other radiation types, although the preliminary test with MeV protons reported at the end of Chapter 3 gave encouraging results.

In conclusion, the doctoral project addressed two aspects related to 2D-MoS_2, the first that deals with its production and the second regarding a new field of application. This work can represent a step forward for both the aspects, firstly with the proposal of a fabrication method that encounters the needs for scalability and versatility, and secondly by expanding the spectrum of applications of 2D-MoS_2 and TMDCs, thanks to a study on the use of 1L-MoS2 for the detection of X-rays. Moreover, this work gives suggestion for future studies related to the mentioned topics that may overcome the current limitations highlighted in the manuscript. With this work I believe that important advances have been made towards a more comprehensive understanding of the potential of 2D-MoS_2 and that it may help in establishing electronic devices based on TMDCs as concrete reality in the future.

Appendix A: Characterization techniques

This section illustrates the basis of the main characterization techniques adopted in this work that are recalled in the chapters 2 and 3.

A.1 Raman spectroscopy

Raman spectroscopy is a valuable tool used to determine the vibrational modes of molecules. In an unknown compound it provides a structural fingerprint from which molecules can be identified. Raman spectroscopy relies on a type of inelastic scattering of light known as Raman scattering. In this process a laser (visible, near infrared or near ultraviolet) is used as a source of photons that are scattered by the target molecules. The scattered photons, being the Raman scattering inelastic,

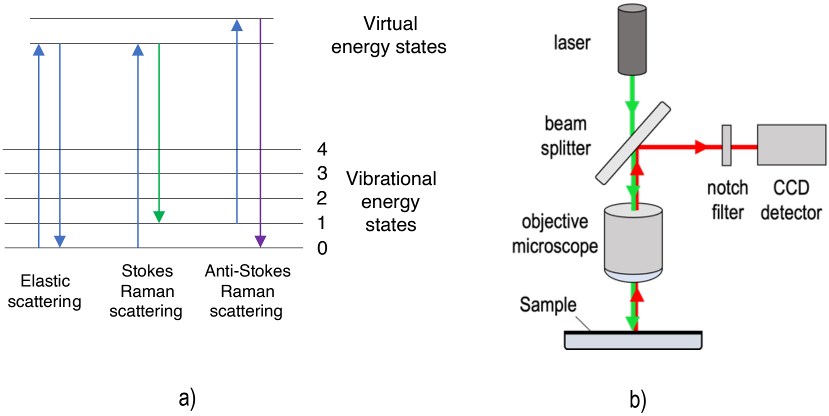

Figure 50: a) Energy level diagram in Raman scattering. b) Schematical representation of the μ-Raman setup.

undergo a shift in energy. The energy shift contains the information about the vibrational modes of the molecules that constitute the material under analysis and can be used to identify their composition and chemical structure. From a theoretical point of view, the photons from the source excite the molecules from either the ground vibrational state (v0) or a higher energy vibrational state (e.g. v1,v2) to a virtual excited state Photons are emitted and the molecules relax to the ground vibrational state or to different vibrational state. The energy level diagram of the process is depicted in Figure 50. Two Raman scattering schemes are possible: a scattering where the energy of the emitted photon is lower than the initial energy (Stokes Raman scattering) and a scattering where the emitted photon energy increases (Anti-Stokes Raman scattering). In the process one must consider that photon undergo elastic scattering as well, i.e. with no shift in energy. To eliminate the contribution from elastically scattered photons, in practice a notch filter is generally used to select the energy of the outcoming photons to analyze. When the excitation energy used for the analysis is close to the excitation energy of the molecules, we speak about *resonant* Raman spectroscopy. This technique provides much higher sensitivity compared to standard non-resonant Raman spectroscopy, because it is possible to excite electrons to a higher electronic state. However, this requires to use a tunable laser which is not needed for the non-resonant counterpart.

Not all the vibrational modes are Raman-active and thus can be identified with this technique though, but only the modes that result in change in the polarizability of the molecules. Raman spectroscopy is particularly suitable for molecules that have weak dipole moment and high polarizability, namely molecules that possess C=C, C-C, C-H bonds. A complementary technique that is often used in combination with Raman spectroscopy is infrared spectroscopy.

Nowadays Raman instrumentation is often coupled with an optical microscope and it is possible to illuminate and analyze areas of few μm^2 . This instrument is called micro-Raman spectrometer.

A.2 X-ray photoelectron spectroscopy

Another powerful spectroscopic technique used to determine the elemental fingerprint of a compound is X-ray photoelectron spectroscopy (XPS), which is based on the photoelectric effect. The photoelectric effect has been introduced in Chapter 1 (see the corresponding section for more details). Briefly, the electrons constituting the atoms of the investigated sample absorb the X-rays and are emitted as photoelectrons. The task of the XPS is to analyze the emitted electrons and, from their binding energy, deduce the elemental composition of the sample.

The experimental setup of an XPS experiment is depicted in Figure 51. The system is kept in ultra-high vacuum (~10^{-10} bar), to avoid discharges and interference to the produced photoelectrons. The sample is illuminated with an almost monochromatic source of X-rays. The X-rays are produced with a process described in Chapter 1 (see section 1.2.2), using a target of magnesium (Mg) or aluminum (Al), for which the X-ray emission spectrum is dominated by the characteristic unresolved X-ray doublet $K_{\alpha 1,2}$ (transition from $2p_{1/2}$ and $2p_{3/2}$ to 1s states, respectively) at 1253.6 eV for Mg and 1486.6 eV for Al. The photoelectrons are collected by an electron analyzer that measures the kinetic energy of the photoelectrons. The kinetic energy of the electrons can be written as follows:

$$E_K = h\upsilon - E_B - \phi_S \qquad (2)$$

Where $h\upsilon$ is the energy of the X-rays, E_B is the binding energy of the electron in the atom and ϕ_S is the work function of the sample, i.e. the energy needed to bring the electron from the sample surface to the vacuum level. XPS is a surface technique that can probe a few nanometers of the sample, depending on the energy of the X-rays. This is associated with the kinetic energy of the photoelectrons that need to traverse the medium before escaping and being collected.

The XPS setup can be also combined with a sputtering mechanism. Sputtering means the removal of atomic layers of the material when it is bombarded with energetic particles, in form of a gas or plasma. Argon is often used for sputtering since it is an inert gas and thus is expected not to react with the sample species. Sputtering combined with XPS allows to access the layers beneath the material surface that would not be accessible with XPS only.

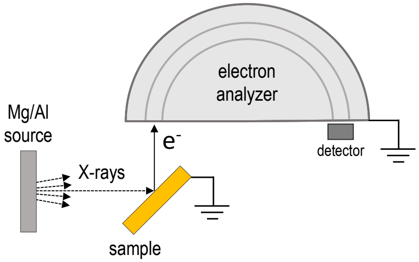

Figure 51: Scheme of the XPS experimental setup.

A.3 Scanning electron microscopy (SEM)

A Scanning electron microscope (SEM) is a microscope producing an image of a sample thanks to a focused beam of electrons that scans the sample surface. SEM is used mainly for its resolution which goes way beyond the optical microscope. With a SEM it is indeed possible to resolve objects at the nanometer scale. This is due to the wavelength of the electrons used in SEM that is orders of magnitude smaller than the visible light exploited in optical microscopes.

The electrons interacting with the sample undergo different processes, mainly produce secondary electrons (SE), they are back scattered (BSE) via elastic

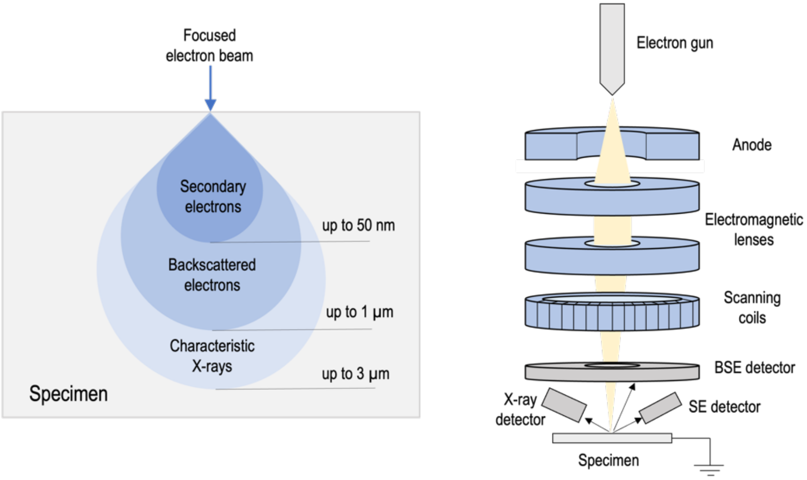

a) b)

Figure 52: a) Sketch of the regions of a specimen that are probed with different SEM acquisition modes. b) Setup of an SEM

scattering, or their interaction with the atoms can produce characteristic X-rays. SEM produce images collecting the SE and BSE escaping the material after their production, while characteristic X-rays can be used to perform elemental analysis of the sample. The produced SE generally have energies below 50 eV, resulting in mean-free paths in the sample of few nanometers after the production. Therefore, the SE signal is likely to come from the very first nanometers of the sample and allow the highest resolution for an SEM. The BSE (and the characteristic X-rays) have instead a larger mean-free path and allow to access the layers beneath the sample surface. This comes with the drawback of a lower spatial resolution. This is summarized in Figure 52(a), where the regions from where the signal is acquired are depicted.

The experimental setup of a typical SEM is reported in Figure 52(b). The whole system is kept in high vacuum. An electron gun is used as source of electrons. The electrons are produced with a tungsten filament with energies up to 40 keV. The electron beam is focused by one or two electromagnetic lenses to a spot with nanometer-scale in diameter. The beam passes through scanning coils, which deflects it along the x and y axes so that it raster scan the specimen area. Detectors for SE, BSE and characteristic X-rays are placed close to the specimen surface allowing data acquisition in different modes. The sample needs in the end to be electrically connected to the ground to discharge the amount of electrons delivered on the specimen. For non-conductive specimens, a metallization step is required prior to the analysis.

A.4 X-ray diffraction (XRD)

X-ray diffraction (XRD) is a technique used to obtain information on the crystalline structure of materials. The technique is non-destructive and can be used to analyze crystalline powders, bulk crystals, and thin films.

XRD exploits an X-ray source that is diffracted by the lattice atoms of the material via elastic scattering. Each atom acts as a diffraction center, generating a coherent front of spherical waves. According to wave diffraction theory, the waves interfere constructively only if the path difference between the scattered waves is an integer multiple of their wavelength. This can be expressed with the Bragg law:

$$n\lambda = 2d\ sin\vartheta \tag{3}$$

Where n is an integer number, λ is the X-ray wavelength, d is the distance between the crystal planes, and ϑ is the angle of incidence of the X-ray beam with respect to the plane of the crystal plane (Figure 53). For a Bragg-Bentano geometry, the experimental setup is composed of an X-ray tube, commonly based on Cu ($K_{\alpha 1}$ = 8.047 keV) or Mo ($K_{\alpha 1}$ = 17.479 keV) target, a goniometer that varies the incidence angle ϑ, and an X-ray detector preceded by a graphite monochromator. The output of the measure is a pattern of the signal intensity vs. the angle 2ϑ, from which is possible to extract information about the distance of the crystalline planes and thus on the crystal lattice parameters, and identify the crystalline phases. Quantitative phase analysis and other information as crystallite size, strains etc. can be calculated from XRD patterns.

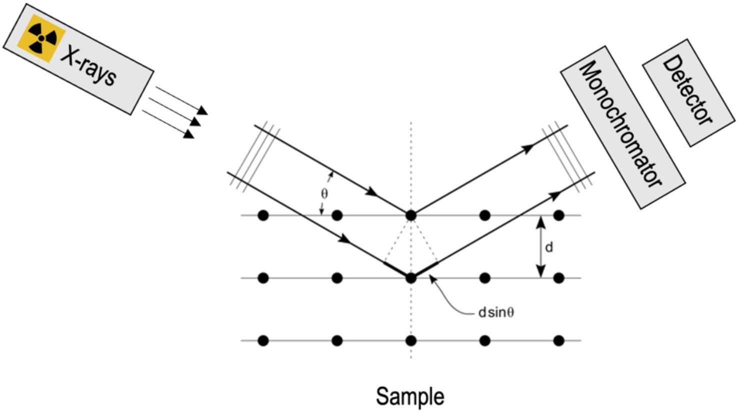

Figure 53: Scheme of the Bragg's law and of an XRD setup.

A.5 Atomic force microscopy (AFM)

Atomic force microscope (AFM) is a powerful tool able to return high-resolution topographical images of the analyzed samples. AFM gives information about surface roughness of materials, and it is capable of measuring interaction forces down to the nanometer scale.

The schematical structure of an AFM is depicted in Figure 54. It is composed by a cantilever with a sharp tip (5-50nm diameter) that probes the surface of the sample. The tips is tilted due to the local force between the tip and the material surface. To measure the vertical motion of the cantilever, a laser pointing the tip of the cantilever gets deflected into a photodiode. A change in the laser position at the photodiode is recorded as a voltage amplitude, from which the force is reconstructed.

The cantilever raster scans the surface in the xy plane thanks to a piezoelectric motor stage. Combining the information on the xy scan and the vertical motion of the cantilever, a map of the surface is obtained. A feedback loop is also needed to monitor

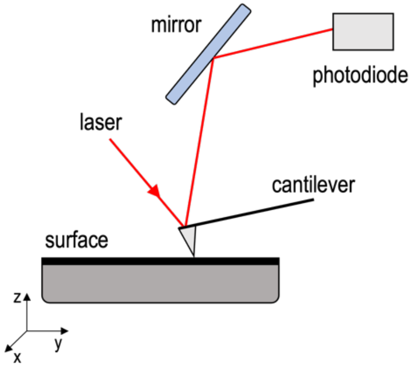

Figure 54: Schematic representation of the AFM setup.

the z-position of the cantilever and dynamically adjust its position point by point while scanning. This mode is called *contact mode*.

When dealing with soft samples, such as organic materials held together with van der Waals forces, the lateral force applied by the tip during the scan might damage the sample. Therefore, an intermittent mode called *tapping mode* can be used, i.e., the tip oscillates instead of staying in contact with the sample surface.

A.6 UV-VIS-NIR spectroscopy

Ultraviolet-visible-near infrared (UV-VIS-NIR) spectroscopy probes the interaction of the material with electromagnetic radiation in a broad wavelength range (200 nm – 2500 nm), namely from the near ultraviolet (NUV) to near infrared (NIR) spectrum. UV-VIS spectrum gives information about the electronic properties of the material, since it is associated with the electronic transition of atoms or molecules, while the NIR spectrum is often responsible for the molecular vibrational modes.

UV-VIS-NIR spectroscopy can be performed in transmission mode or in diffused reflectance mode. In transmission mode, the instrument measures the light intensity I_1 after it passes through the sample and compare it with intensity of the incident light (I_0). The ratio I_1 / I_0 is called transmittance T and can be expressed as percentage (%T). It is common to calculate the absorbance A from the transmittance, that is $A = -\log(T)$. The transmittance or absorbance measurement is related to the Lambert-Beer law, which is often used to determine the concentration of absorbers (chromophores)

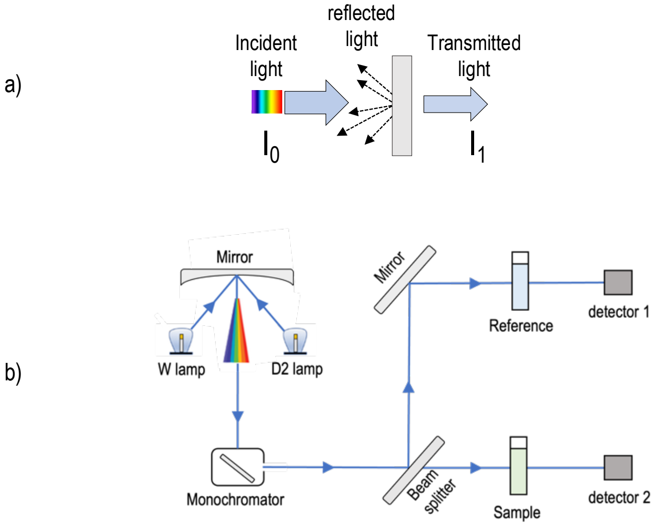

Figure 55: a) scheme of the light interaction with a sample in the UV-VIS-NIR spectrometer; b) scheme of a UV-VIS-NIR spectrophotometer setup.

in solutions. Moreover, the absorbance spectrum gives important information about the electronic transitions of a material. Such measurements are particularly interesting to study semiconductor electronic properties. In fact, ideal semiconductors possess an electronic band structure, where the valence band is separated from the conduction band by an energy gap of ~1-2 eV with no energy states in between (see section). It happens that there is a cut-off energy of the photons under which semiconductors are almost transparent to light, while they start to absorb photons right above the band gap energy. This feature can be easily recognized with a spectrometer since the absorbance spectrum shows a steep increase when the photon energy approaches the energy bandgap.

The spectrometer can be configured to measure reflectance. Reflectance is calculated as the ratio between the light intensity I_R reflected from the sample and the light intensity I_{R0} reflected from a reference material ($R = I_R / I_{R0}$), and it is expressed as percentage, similarly to transmittance. Reflectance measurements are of particular importance for example when dealing with anti-reflecting coating, vastly used nowadays in semiconductor technology and photovoltaic panel industry.

The scheme of a spectrophotometer is depicted in Figure 55. The radiation source is composed of a tungsten lamp (emitting in the range 300-2500 nm) for the VIS-NIR spectrum and a deuterium lamp (190-400 nm) for the UV spectrum. The source is followed by a monochromator to select the spectral line to be used as excitation. A beam splitter splits the radiation is two paths, one that passes through the sample, and one used as a reference, prior to collect them in a photodetector.

A.7 Thermal analyses

Thermal analysis is a fundamental technique used to study the evolution of a material when the temperature varies. The evolution can be due to physical phenomena such as phase transitions or adsorption/desorption processes, as well as chemical phenomena such as thermal decomposition or chemisorption, occurring when the temperature increases [136].

Thermogravimetric analysis (TGA) is a thermal analysis method in which the mass of a sample is measured as a function of the temperature. A thermogravimetric analyzer is composed of a precision balance that continuously monitors the mass, a furnace that hosts a crucible in which the sample is loaded, and a second crucible that can be used as a reference (Figure 56). The furnace has a programmable temperature control and can be heated up to more than 1000 °C. The sample can be kept in air, vacuum, or inert gas atmosphere, depending on the reactions to be investigated. TGA curve is often combined with its time derivative, called DTG, that can be used to determine inflection points.

Differential thermal analysis (DTA) is used in combination with TGA and often share the same experimental setup. While TGA is used to determine the mass variation of the sample, in DTA the temperature difference between the sample and a reference sample is measured while varying the temperature. This measure gives information about the thermodynamics of the reactions occurring in the material and allows to discriminate between endothermic and exothermic phenomena. The combined information from TGA and DTA gives an overview of the processes occurring in a material at different temperatures.

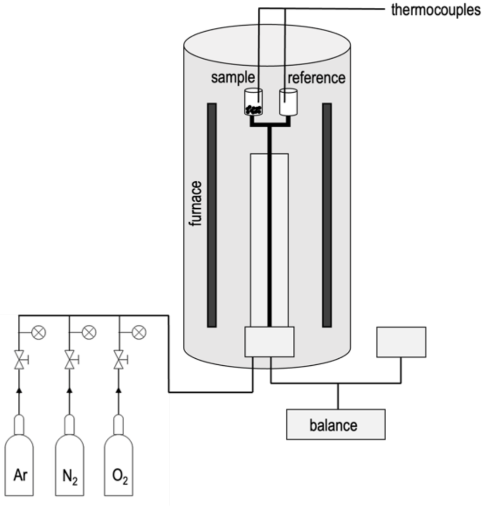

Figure 56: Schematical representation of a TGA/DTA setup

A.8 Electro-optical characterization

When dealing with photodetectors it is important to characterize their electrical response to light. Figure 57 illustrates a potential setup for electro-optical characterization of a device. The device is connected to a voltage bias source and a current is measured. This is generally performed with a source measurement unit. Light sources are then used to illuminate the device under test in the measurement. A simple way is to use LED light sources of know optical power. To perform the measurements, while the source measurement unit is acquiring a current, different LEDs are switched on and off. In this way it is possible to extract several important quantities such as dark (leakage) current, on-off ratio, response time and responsivity. The dark current is current flowing in the photodetector when the illumination is off. The on-off ratio gives the ratio between the current measured under illumination and the current measured in the dark. This is generally displayed in a current-voltage (J-V) plot, where the two curves (dark vs illumination) are compared, and it is preferable to have it as high as possible when very sensitive measurements are needed. The response time gives information on the time needed to react to a variation in the illumination and to reach a new steady state. This is often indicated by two measurements, the rise time τ_r (time needed to go from 0 to 90% of the signal) and decay time τ_d (time needed to go from 100% to 10% of the signal). The measure can

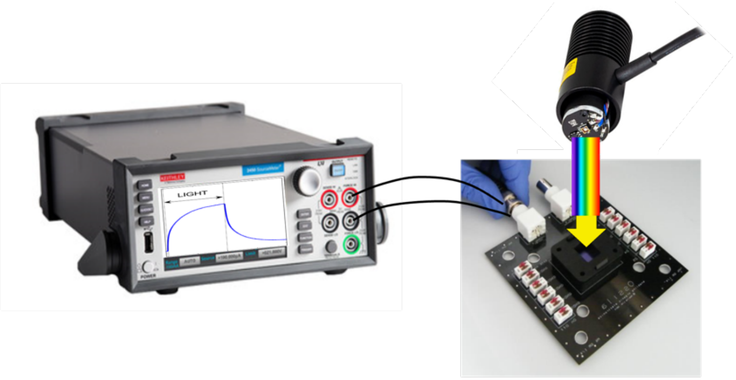

Figure 57: Scheme of the setup used for the electrical characterization of the photodetectors

be limited by the speed of the electronics in very fast devices. This is especially important for devices that need to operate at high frequencies. Responsivity measures the amount of current that is generated in a photodetector when it is illuminated (photocurrent), per unit illuminating power. Responsivity is often used to compare the performance of different photodetectors. Moreover, since responsivity is a measure that depends on the wavelength of the photons illuminating the detector and it gives information on the optical properties of the detecting material.

Acknowledgments

I would like to express my heartfelt gratitude to the following people who have supported me throughout my doctoral journey:

My supervisor, Prof. Lucio Pancheri, for his unwavering support, guidance, and for providing me with a low stress environment to complete my work.
Prof. Emil J.W. List Kratochvil, for his wise advice and for welcoming me in his research group, treating me as a part of the group, rather than a guest.
Dr. Giovanni Ligorio, for his encouragement and mentorship. Thanks for your critical attitude and for making me feel at home in a different country.
A special thanks to Prof. Sandra Dirè, for her continuous help throughout the project from a professional and human point of view.
Prof. Alberto Quaranta, for having appreciated my work, for the precious comments and for the support during the teaching activities.
Thanks to all the people from the industrial engineering department at the University of Trento, for providing me with an environment in which I could thrive and grow as a scholar and as a person.
Thanks to all the people from the IRIS Adlershof center at the Humboldt university of Berlin for the help and patience you demonstrated.

And to my friends and family, thank you for your constant support, patience, and love.

Bibliography

1. Novoselov KS, Geim AK, Morozov S V., Jiang D, Zhang Y, Dubonos S V., Grigorieva I V., Firsov AA. Electric field in atomically thin carbon films. *Science (80-)*. 2004;306(5696). doi:10.1126/science.1102896
2. Radisavljevic B, Radenovic A, Brivio J, Giacometti V, Kis A. Single-layer MoS2 transistors. *Nat Nanotechnol*. 2011;6(3). doi:10.1038/nnano.2010.279
3. Wang C, Yang F, Gao Y. The highly-efficient light-emitting diodes based on transition metal dichalcogenides: From architecture to performance. *Nanoscale Adv*. 2020;2(10):4323-4340. doi:10.1039/d0na00501k
4. Wang H, Li C, Fang P, Zhang Z, Zhang JZ. Synthesis, properties, and optoelectronic applications of two-dimensional MoS2 and MoS2-based heterostructures. *Chem Soc Rev*. 2018;47(16):6101-6127. doi:10.1039/c8cs00314a
5. Nalwa HS. A review of molybdenum disulfide (MoS2) based photodetectors: From ultra-broadband, self-powered to flexible devices. *RSC Adv*. 2020;10(51). doi:10.1039/d0ra03183f
6. Taffelli A, Dirè S, Quaranta A, Pancheri L, Villanueva G. MoS 2 Based Photodetectors: A Review. Published online 2021. doi:10.3390/s21082758
7. Nardi M V., Timpel M, Ligorio G, Zorn Morales N, Chiappini A, Toccoli T, Verucchi R, Ceccato R, Pasquali L, List-Kratochvil EJW, et al. Versatile and Scalable Strategy to Grow Sol-Gel Derived 2H-MoS2 Thin Films with Superior Electronic Properties: A Memristive Case. *ACS Appl Mater Interfaces*. 2018;10(40):34392-34400. doi:10.1021/acsami.8b12596
8. Posar JA, Petasecca M, Griffith MJ. A review of printable, flexible and tissue equivalent materials for ionizing radiation detection. *Flex Print Electron*. 2021;6(4). doi:10.1088/2058-8585/ac32aa
9. Taffelli A, Ligorio G, Pancheri L, Quaranta A, Ceccato R, Chiappini A, Nardi MV, List-Kratochvil EJW, Dirè S. Large area MoS2 films fabricated via sol-gel used for photodetectors. *Opt Mater (Amst)*. 2023;135(September 2022). doi:10.1016/j.optmat.2022.113257
10. Huo N, Konstantatos G. Recent progress and future prospects of 2D-based photodetectors. *Adv Mater*. 2018;30(51). doi:10.1002/adma.201801164
11. Mueller T, Xia F, Avouris P. Graphene photodetectors for high-speed optical communications. *Nat Photonics*. 2010;4(5). doi:10.1038/nphoton.2010.40
12. Mak KF, Lee C, Hone J, Shan J, Heinz TF. Atomically thin MoS2: A new direct-gap semiconductor. *Phys Rev Lett*. 2010;105(13). doi:10.1103/PhysRevLett.105.136805

13. Bernardi M, Palummo M, Grossman JC. Extraordinary sunlight absorption and one nanometer thick photovoltaics using two-dimensional monolayer materials. *Nano Lett*. 2013;13(8). doi:10.1021/nl401544y
14. Jiménez Sandoval S, Yang D, Frindt RF, Irwin JC. Raman study and lattice dynamics of single molecular layers of MoS2. *Phys Rev B*. 1991;44(8). doi:10.1103/PhysRevB.44.3955
15. Voiry D, Goswami A, Kappera R, Silva CDCCE, Kaplan D, Fujita T, Chen M, Asefa T, Chhowalla M. Covalent functionalization of monolayered transition metal dichalcogenides by phase engineering. *Nat Chem*. 2015;7(1). doi:10.1038/nchem.2108
16. Kang Y, Najmaei S, Liu Z, Bao Y, Wang Y, Zhu X, Halas NJ, Nordlander P, Ajayan PM, Lou J, et al. Plasmonic Hot Electron Induced Structural Phase Transition in a MoS2 Monolayer. *Adv Mater*. 2014;26(37). doi:10.1002/adma.201401802
17. Li X, Tao L, Chen Z, Fang H, Li X, Wang X, Xu J Bin, Zhu H. Graphene and related two-dimensional materials: Structure-property relationships for electronics and optoelectronics. *Appl Phys Rev*. 2017;4(2). doi:10.1063/1.4983646
18. Katagiri Y, Nakamura T, Ishii A, Ohata C, Hasegawa M, Katsumoto S, Cusati T, Fortunelli A, Iannaccone G, Fiori G, et al. Gate-tunable atomically thin lateral MoS2 Schottky junction patterned by electron beam. *Nano Lett*. 2016;16(6). doi:10.1021/acs.nanolett.6b01186
19. Li T, Galli G. Electronic Properties of MoS2 Nanoparticles. *J Phys Chem C*. 2007;111(44):16192-16196. doi:10.1021/jp075424v
20. Lebègue S, Eriksson O. Electronic structure of two-dimensional crystals from ab initio theory. *Phys Rev B - Condens Matter Mater Phys*. 2009;79(11). doi:10.1103/PhysRevB.79.115409
21. Cheiwchanchamnangij T, Lambrecht WRL. Quasiparticle band structure calculation of monolayer, bilayer, and bulk MoS 2. *Phys Rev B - Condens Matter Mater Phys*. 2012;85(20). doi:10.1103/PhysRevB.85.205302
22. Kam KK, Parkinson BA. Detailed photocurrent spectroscopy of the semiconducting group VIB transition metal dichalcogenides. *J Phys Chem*. 1982;86(4):463-467. doi:10.1021/j100393a010
23. Splendiani A, Sun L, Zhang Y, Li T, Kim J, Chim CY, Galli G, Wang F. Emerging photoluminescence in monolayer MoS2. *Nano Lett*. 2010;10(4):1271-1275. doi:10.1021/nl903868w
24. Zeng H, Dai J, Yao W, Xiao D, Cui X. Valley polarization in MoS 2 monolayers by optical pumping. *Nat Nanotechnol*. 2012;7(8). doi:10.1038/nnano.2012.95
25. Xiao D, Liu G Bin, Feng W, Xu X, Yao W. Coupled spin and valley physics in monolayers of MoS 2 and other group-VI dichalcogenides. *Phys Rev Lett*. 2012;108(19). doi:10.1103/PhysRevLett.108.196802
26. Schaibley JR, Yu H, Clark G, Rivera P, Ross JS, Seyler KL, Yao W, Xu X.

Valleytronics in 2D materials. *Nat Rev Mater*. 2016;1(11). doi:10.1038/natrevmats.2016.55

27. Liu Y, Gao Y, Zhang S, He J, Yu J, Liu Z. Valleytronics in transition metal dichalcogenides materials. *Nano Res*. 2019;12(11). doi:10.1007/s12274-019-2497-2
28. Dhakal KP, Duong DL, Lee J, Nam H, Kim M, Kan M, Lee YH, Kim J. Confocal absorption spectral imaging of MoS2: Optical transitions depending on the atomic thickness of intrinsic and chemically doped MoS2. *Nanoscale*. 2014;6(21). doi:10.1039/c4nr03703k
29. Kwak JY. Absorption coefficient estimation of thin MoS 2 film using attenuation of silicon substrate Raman signal. *Results Phys*. 2019;13(March):102202. doi:10.1016/j.rinp.2019.102202
30. Choi W, Cho MY, Konar A, Lee JH, Cha GB, Hong SC, Kim S, Kim J, Jena D, Joo J, et al. High-detectivity multilayer MoS2 phototransistors with spectral response from ultraviolet to infrared. *Adv Mater*. 2012;24(43):5832-5836. doi:10.1002/adma.201201909
31. Lopez-Sanchez O, Lembke D, Kayci M, Radenovic A, Kis A. Ultrasensitive photodetectors based on monolayer MoS 2. *Nat Nanotechnol*. 2013;8(7):497-501. doi:10.1038/nnano.2013.100
32. He J, Yang Y, He Y, Ge C, Zhao Y, Gao L, Tang J. Low Noise and Fast Photoresponse of Few-Layered MoS2 Passivated by MA3Bi2Br9. *ACS Photonics*. 2018;5(5):1877-1884. doi:10.1021/acsphotonics.8b00129
33. Gant P, Huang P, Pérez de Lara D, Guo D, Frisenda R, Castellanos-Gomez A. A strain tunable single-layer MoS2 photodetector. *Mater Today*. 2019;27(August):8-13. doi:10.1016/j.mattod.2019.04.019
34. Gonzalez Marin JF, Unuchek D, Watanabe K, Taniguchi T, Kis A. MoS2 photodetectors integrated with photonic circuits. *npj 2D Mater Appl*. 2019;3(1). doi:10.1038/s41699-019-0096-4
35. Wang H, Wang X, Chen Y, Zhang S, Jiang W, Zhang X, Qin J, Wang J, Li X, Pan Y, et al. Extremely Low Dark Current MoS2 Photodetector via 2D Halide Perovskite as the Electron Reservoir. *Adv Opt Mater*. 2020;8(6):2-9. doi:10.1002/adom.201901402
36. Klots AR, Newaz AKM, Wang B, Prasai D, Krzyzanowska H, Lin J, Caudel D, Ghimire NJ, Yan J, Ivanov BL, et al. Probing excitonic states in suspended two-dimensional semiconductors by photocurrent spectroscopy. *Sci Rep*. 2014;4:1-7. doi:10.1038/srep06608
37. Wi S, Chen M, Nam H, Liu AC, Meyhofer E, Liang X. High blue-near ultraviolet photodiode response of vertically stacked graphene-MoS2-metal heterostructures. *Appl Phys Lett*. 2014;104(23):1-6. doi:10.1063/1.4882417
38. Li X, Wu J, Mao N, Zhang J, Lei Z, Liu Z, Xu H. A self-powered graphene-MoS2 hybrid phototransistor with fast response rate and high on-off ratio. *Carbon N Y*. 2015;92:126-132. doi:10.1016/j.carbon.2015.03.064

39. Kufer D, Nikitskiy I, Lasanta T, Navickaite G, Koppens FHL, Konstantatos G. Hybrid 2D-0D MoS2-PbS quantum dot photodetectors. *Adv Mater*. 2015;27(1):176-180. doi:10.1002/adma.201402471
40. Long M, Liu E, Wang P, Gao A, Xia H, Luo W, Wang B, Zeng J, Fu Y, Xu K, et al. Broadband Photovoltaic Detectors Based on an Atomically Thin Heterostructure. *Nano Lett*. 2016;16(4):2254-2259. doi:10.1021/acs.nanolett.5b04538
41. Ra HS, Kwak DH, Lee JS. A hybrid MoS2 nanosheet-CdSe nanocrystal phototransistor with a fast photoresponse. *Nanoscale*. 2016;8(39):17223-17230. doi:10.1039/c6nr05393a
42. Huo N, Gupta S, Konstantatos G. MoS2–HgTe Quantum Dot Hybrid Photodetectors beyond 2 µm. *Adv Mater*. 2017;29(17):1-5. doi:10.1002/adma.201606576
43. Chen Y, Wang X, Wu G, Wang Z, Fang H, Lin T, Sun S, Shen H, Hu W, Wang J, et al. High-Performance Photovoltaic Detector Based on MoTe2/MoS2 Van der Waals Heterostructure. *Small*. 2018;14(9):1-7. doi:10.1002/smll.201703293
44. Novoselov KS, Jiang D, Schedin F, Booth TJ, Khotkevich V V., Morozov S V., Geim AK. Two-dimensional atomic crystals. *Proc Natl Acad Sci U S A*. 2005;102(30). doi:10.1073/pnas.0502848102
45. Sun J, Li X, Guo W, Zhao M, Fan X, Dong Y, Xu C, Deng J, Fu Y. Synthesis methods of two-dimensional MoS2: A brief review. *Crystals*. 2017;7(7):1-11. doi:10.3390/cryst7070198
46. Magda GZ, Petõ J, Dobrik G, Hwang C, Biró LP, Tapasztó L. Exfoliation of large-area transition metal chalcogenide single layers. *Sci Rep*. 2015;5. doi:10.1038/srep14714
47. Heyl M, Burmeister D, Schultz T, Pallasch S, Ligorio G, Koch N, List-Kratochvil EJW. Thermally Activated Gold-Mediated Transition Metal Dichalcogenide Exfoliation and a Unique Gold-Mediated Transfer. *Phys Status Solidi - Rapid Res Lett*. 2020;14(11):1-5. doi:10.1002/pssr.202000408
48. Heyl M, Grützmacher S, Rühl S, Ligorio G, Koch N, List-Kratochvil EJW. Low Temperature Heating of Silver-Mediated Exfoliation of MoS2. *Adv Mater Interfaces*. Published online 2022. doi:10.1002/admi.202200362
49. Heyl M, List-Kratochvil EJW. Only gold can pull this off: mechanical exfoliations of transition metal dichalcogenides beyond scotch tape. *Appl Phys A Mater Sci Process*. 2023;129(1):1-17. doi:10.1007/s00339-022-06297-z
50. Lee Y, Lee J, Bark H, Oh IK, Ryu GH, Lee Z, Kim H, Cho JH, Ahn JH, Lee C. Synthesis of wafer-scale uniform molybdenum disulfide films with control over the layer number using a gas phase sulfur precursor. *Nanoscale*. 2014;6(5):2821-2826. doi:10.1039/c3nr05993f
51. Seravalli L, Bosi M. A review on chemical vapour deposition of two-

dimensional mos2 flakes. *Materials (Basel)*. 2021;14(24). doi:10.3390/ma14247590

52. Yang P, Yang H, Wu Z, Liao F, Guo X, Deng J, Xu Q, Wang H, Sun J, Chen F, et al. Large-Area Monolayer MoS2Nanosheets on GaN Substrates for Light-Emitting Diodes and Valley-Spin Electronic Devices. *ACS Appl Nano Mater*. 2021;4(11). doi:10.1021/acsanm.1c02662
53. Dumcenco D, Ovchinnikov D, Marinov K, Lazić P, Gibertini M, Marzari N, Sanchez OL, Kung YC, Krasnozhon D, Chen MW, et al. Large-area epitaxial monolayer moS2. *ACS Nano*. 2015;9(4). doi:10.1021/acsnano.5b01281
54. Van Der Zande AM, Huang PY, Chenet DA, Berkelbach TC, You Y, Lee GH, Heinz TF, Reichman DR, Muller DA, Hone JC. Grains and grain boundaries in highly crystalline monolayer molybdenum disulphide. *Nat Mater*. 2013;12(6). doi:10.1038/nmat3633
55. Ahn C, Lee J, Kim HU, Bark H, Jeon M, Ryu GH, Lee Z, Yeom GY, Kim K, Jung J, et al. Low-Temperature Synthesis of Large-Scale Molybdenum Disulfide Thin Films Directly on a Plastic Substrate Using Plasma-Enhanced Chemical Vapor Deposition. *Adv Mater*. 2015;27(35). doi:10.1002/adma.201501678
56. Zhou X, Xu B, Lin Z, Shu D, Ma L. Hydrothermal synthesis of flower-like MoS2nanospheres for electrochemical supercapacitors. *J Nanosci Nanotechnol*. 2014;14(9). doi:10.1166/jnn.2014.8929
57. Feng X, Tang Q, Zhou J, Fang J, Ding P, Sun L, Shi L. Novel mixed-solvothermal synthesis of MoS2 nanosheets with controllable morphologies. *Cryst Res Technol*. 2013;48(6). doi:10.1002/crat.201300003
58. Suh J, Park TE, Lin DY, Fu D, Park J, Jung HJ, Chen Y, Ko C, Jang C, Sun Y, et al. Doping against the native propensity of MoS2: Degenerate hole doping by cation substitution. *Nano Lett*. 2014;14(12). doi:10.1021/nl503251h
59. Li M, Yao J, Wu X, Zhang S, Xing B, Niu X, Yan X, Yu Y, Liu Y, Wang Y. P-type Doping in Large-Area Monolayer MoS2 by Chemical Vapor Deposition. *ACS Appl Mater Interfaces*. 2020;12(5). doi:10.1021/acsami.9b19864
60. Kim E, Ko C, Kim K, Chen Y, Suh J, Ryu SG, Wu K, Meng X, Suslu A, Tongay S, et al. Site Selective Doping of Ultrathin Metal Dichalcogenides by Laser-Assisted Reaction. *Adv Mater*. 2016;28(2). doi:10.1002/adma.201503945
61. Zhang K, Feng S, Wang J, Azcatl A, Lu N, Addou R, Wang N, Zhou C, Lerach J, Bojan V, et al. Erratum: Manganese Doping of Monolayer MoS2: The Substrate Is Critical (Nano Letters 2015, 15:10 (6586-6591) 10.1021/acs.nanolett.5b02315). *Nano Lett*. 2016;16(3). doi:10.1021/acs.nanolett.6b00760

62. Chen M, Nam H, Wi S, Ji L, Ren X, Bian L, Lu S, Liang X. Stable few-layer MoS2 rectifying diodes formed by plasma-assisted doping. *Appl Phys Lett*. 2013;103(14). doi:10.1063/1.4824205
63. Mouri S, Miyauchi Y, Matsuda K. Tunable photoluminescence of monolayer MoS2 via chemical doping. *Nano Lett*. 2013;13(12). doi:10.1021/nl403036h
64. Nakotte T, Luo H, Pietryga J. PbE (E = S, Se) colloidal quantum dot-layered 2D material hybrid photodetectors. *Nanomaterials*. 2020;10(1). doi:10.3390/nano10010172
65. Tsai DS, Liu KK, Lien DH, Tsai ML, Kang CF, Lin CA, Li LJ, He JH. Few-layer MoS2 with high broadband photogain and fast optical switching for use in harsh environments. *ACS Nano*. 2013;7(5):3905-3911. doi:10.1021/nn305301b
66. Yore AE, Smithe KKH, Jha S, Ray K, Pop E, Newaz AKM. Large array fabrication of high performance monolayer MoS2 photodetectors. *Appl Phys Lett*. 2017;111(4). doi:10.1063/1.4995984
67. Kang MA, Kim S, Jeon IS, Lim YR, Park CY, Song W, Lee SS, Lim J, An KS, Myung S. Highly efficient and flexible photodetector based on MoS2-ZnO heterostructures. *RSC Adv*. 2019;9(34):19707-19711. doi:10.1039/c9ra00578a
68. Sahatiya P, Jones SS, Badhulika S. 2D MoS2–carbon quantum dot hybrid based large area, flexible UV–vis–NIR photodetector on paper substrate. *Appl Mater Today*. 2018;10:106-114. doi:10.1016/j.apmt.2017.12.013
69. Gomathi PT, Sahatiya P, Badhulika S. Large-Area, Flexible Broadband Photodetector Based on ZnS–MoS2 Hybrid on Paper Substrate. *Adv Funct Mater*. 2017;27(31). doi:10.1002/adfm.201701611
70. Tan H, Xu W, Sheng Y, Lau CS, Fan Y, Chen Q, Tweedie M, Wang X, Zhou Y, Warner JH. Lateral Graphene-Contacted Vertically Stacked WS2/MoS2 Hybrid Photodetectors with Large Gain. *Adv Mater*. 2017;29(46):1-8. doi:10.1002/adma.201702917
71. Zhang XM, Tseng SH, Lu MY. Large-area ultraviolet photodetectors based on p-type multilayer MoS 2 enabled by plasma doping. *Appl Sci*. 2019;9(6). doi:10.3390/app9061110
72. Kumar R, Goel N, Raliya R, Biswas P, Kumar M. High-performance photodetector based on hybrid of MoS2 and reduced graphene oxide. *Nanotechnology*. 2018;29(40). doi:10.1088/1361-6528/aad2f6
73. Solanke S, Rathakanthiwar S, Kalra A, Rangarajan M, Raghavan S, Nath DN. Multi-layer MoS2/GaN UV-Visible photodetector with observation of MoS2band edge in spectral responsivity. *arXiv*. Published online 2018.
74. Kumar R, Sharma A, Kaur M, Husale S. Pt-Nanostrip-Enabled Plasmonically Enhanced Broad Spectral Photodetection in Bilayer MoS2. *Adv Opt Mater*. 2017;5(9). doi:10.1002/adom.201700009
75. Zhou X, Zhou N, Li C, Song H, Zhang Q, Hu X, Gan L, Li H, Lü J, Luo J, et

al. Vertical heterostructures based on SnSe2/MoS2 for high performance photodetectors. *2D Mater*. 2017;4(2). doi:10.1088/2053-1583/aa6422
76. Yu WJ, Liu Y, Zhou H, Yin A, Li Z, Huang Y, Duan X. Highly efficient gate-tunable photocurrent generation in vertical heterostructures of layered materials. *Nat Nanotechnol*. 2013;8(12). doi:10.1038/nnano.2013.219
77. Tsai DS, Lien DH, Tsai ML, Su SH, Chen KM, Ke JJ, Yu YC, Li LJ, He JH. Trilayered MoS2 metal -Semiconductor-metal photodetectors: Photogain and radiation resistance. *IEEE J Sel Top Quantum Electron*. 2014;20(1). doi:10.1109/JSTQE.2013.2268383
78. Zhang W, Chuu CP, Huang JK, Chen CH, Tsai ML, Chang YH, Liang C Te, Chen YZ, Chueh YL, He JH, et al. Ultrahigh-Gain Photodetectors Based on Atomically Thin Graphene-MoS2 Heterostructures. *Sci Rep*. 2015;4. doi:10.1038/srep03826
79. Vabbina P, Choudhary N, Chowdhury AA, Sinha R, Karabiyik M, Das S, Choi W, Pala N. Highly Sensitive Wide Bandwidth Photodetector Based on Internal Photoemission in CVD Grown p-Type MoS2/Graphene Schottky Junction. *ACS Appl Mater Interfaces*. 2015;7(28). doi:10.1021/acsami.5b00887
80. Ye K, Liu L, Liu Y, Nie A, Zhai K, Xiang J, Wang B, Wen F, Mu C, Zhao Z, et al. Lateral Bilayer MoS2–WS2 Heterostructure Photodetectors with High Responsivity and Detectivity. *Adv Opt Mater*. 2019;7(20). doi:10.1002/adom.201900815
81. Shin GH, Park J, Lee KJ, Lee GB, Jeon HB, Choi YK, Yu K, Choi SY. Si-MoS 2 vertical heterojunction for a photodetector with high responsivity and low noise equivalent power. *ACS Appl Mater Interfaces*. 2019;11(7). doi:10.1021/acsami.8b21629
82. Wang L, Jie J, Shao Z, Zhang Q, Zhang X, Wang Y, Sun Z, Lee ST. MoS2/Si heterojunction with vertically standing layered structure for ultrafast, high-detectivity, self-driven visible-near infrared photodetectors. *Adv Funct Mater*. 2015;25(19). doi:10.1002/adfm.201500216
83. Zhang Y, Yu Y, Mi L, Wang H, Zhu Z, Wu Q, Zhang Y, Jiang Y. In Situ Fabrication of Vertical Multilayered MoS2/Si Homotype Heterojunction for High-Speed Visible-Near-Infrared Photodetectors. *Small*. 2016;12(8). doi:10.1002/smll.201502923
84. Ye L, Li H, Chen Z, Xu J. Near-Infrared Photodetector Based on MoS2/Black Phosphorus Heterojunction. *ACS Photonics*. 2016;3(4). doi:10.1021/acsphotonics.6b00079
85. NIST: X-ray mass attenuation coefficients. https://physics.nist.gov/PhysRefData/XrayMassCoef/chap2.html
86. Coolidge WD. The development of modern roentgen-ray generating apparatus. *Am J Roentgenol*. 1930;24:605-620.
87. Butson MJ, Yu PKN, Cheung T, Metcalfe P. Radiochromic film for medical radiation dosimetry. *Mater Sci Eng R Reports*. 2003;41(3-5):61-120.

doi:10.1016/S0927-796X(03)00034-2
88. Jones DP. *Biomedical Sensors*. (Jones DP, ed.). Momentum Press; 2010.
89. Devic S. Radiochromic film dosimetry: Past, present, and future. *Phys Medica*. 2011;27(3). doi:10.1016/j.ejmp.2010.10.001
90. Nikl M. Scintillation detectors for x-rays. *Meas Sci Technol*. 2006;17(4). doi:10.1088/0957-0233/17/4/R01
91. Gaseous detectors. https://indico.cern.ch/event/975141/contributions/4157757/attachments/2165443/3654602/2020-Lecture-4-1-Gaseous Detectors.pdf
92. Zhang Q, Zhang C, Lu Y, Yang K, Ren Q. Progress in the development of CdZnTe unipolar detectors for different anode geometries and data corrections. *Sensors (Switzerland)*. 2013;13(2):2447-2474. doi:10.3390/s130202447
93. Damulira E. Radiation dosimetry in medicine using II-VI semiconductors. *J Radiat Res Appl Sci*. 2022;15(3):72-82. doi:10.1016/j.jrras.2022.06.001
94. Milbrath BD, Peurrung AJ, Bliss M, Weber WJ. Radiation detector materials: An overview. *J Mater Res*. 2008;23(10):2561-2581. doi:10.1557/jmr.2008.0319
95. Thirimanne HM, Jayawardena KDGI, Parnell AJ, Bandara RMI, Karalasingam A, Pani S, Huerdler JE, Lidzey DG, Tedde SF, Nisbet A, et al. High sensitivity organic inorganic hybrid X-ray detectors with direct transduction and broadband response. *Nat Commun*. 2018;9(1). doi:10.1038/s41467-018-05301-6
96. Köhler A, Heinz B. *Electronic Processes in Organic Semiconductors*. Wiley-VCH; 2015. doi:10.1002/9783527685172
97. Zhao D, Xu M, Xiao B, Zhang B, Yan L, Zeng G, Dubois A, Sellin P, Jie W, Xu Y. Purely organic 4HCB single crystals exhibiting high hole mobility for direct detection of ultralow-dose X-radiation. *J Mater Chem A*. 2020;8(10):5217-5226. doi:10.1039/c9ta12817d
98. Troisi A. Prediction of the absolute charge mobility of molecular semiconductors: The case of rubrene. *Adv Mater*. 2007;19(15):2000-2004. doi:10.1002/adma.200700550
99. Jurchescu OD, Baas J, Palstra TTM. Effect of impurities on the mobility of single crystal pentacene. *Appl Phys Lett*. 2004;84(16):3061-3063. doi:10.1063/1.1704874
100. Fraboni B, Femoni C, Mencarelli I, Setti L, Pietro R Di, Cavallini A, Fraleoni-Morgera A. Solution-grown, macroscopic organic single crystals exhibiting three-dimensional anisotropic charge-transport properties. *Adv Mater*. 2009;21(18):1835-1839. doi:10.1002/adma.200802904
101. Ciavatti A, Capria E, Fraleoni-Morgera A, Tromba G, Dreossi D, Sellin PJ, Cosseddu P, Bonfiglio A, Fraboni B. Toward Low-Voltage and Bendable X-Ray Direct Detectors Based on Organic Semiconducting Single Crystals. *Adv Mater*. 2015;27(44):7213-7220.

doi:10.1002/adma.201503090

102. Basiricò L, Ciavatti A, Cramer T, Cosseddu P, Bonfiglio A, Fraboni B. Direct X-ray photoconversion in flexible organic thin film devices operated below 1 v. *Nat Commun*. 2016;7. doi:10.1038/ncomms13063

103. Kajal P, Ghosh K, Powar S. Manufacturing Techniques of Perovskite Solar Cells. *Energy, Environ Sustain*. Published online 2018:341-364. doi:10.1007/978-981-10-7206-2_16

104. NRL Research Cell Efficiency record. Published 2019. Accessed January 8, 2023. https://www.nrel.gov/pv/assets/pdfs/best-research-cell-efficiencies.pdf

105. Chen Y, Yi HT, Wu X, Haroldson R, Gartstein YN, Rodionov YI, Tikhonov KS, Zakhidov A, Zhu XY, Podzorov V. Extended carrier lifetimes and diffusion in hybrid perovskites revealed by Hall effect and photoconductivity measurements. *Nat Commun*. 2016;7. doi:10.1038/ncomms12253

106. Hu M, Jia S, Liu Y, Cui J, Zhang Y, Su H, Cao S, Mo L, Chu D, Zhao G, et al. Large and Dense Organic-Inorganic Hybrid Perovskite CH3NH3PbI3 Wafer Fabricated by One-Step Reactive Direct Wafer Production with High X-ray Sensitivity. *ACS Appl Mater Interfaces*. 2020;12(14):16592-16600. doi:10.1021/acsami.9b23158

107. Liu J, Shabbir B, Wang C, Wan T, Ou Q, Yu P, Tadich A, Jiao X, Chu D, Qi D, et al. Flexible, Printable Soft-X-Ray Detectors Based on All-Inorganic Perovskite Quantum Dots. *Adv Mater*. 2019;31(30):1-8. doi:10.1002/adma.201901644

108. Zhang Y, Liu Y, Xu Z, Ye H, Yang Z, You J, Liu M, He Y, Kanatzidis MG, Liu S (Frank). Nucleation-controlled growth of superior lead-free perovskite Cs3Bi2I9 single-crystals for high-performance X-ray detection. *Nat Commun*. 2020;11(1):1-11. doi:10.1038/s41467-020-16034-w

109. Zhuge F, Luo P, Zhai T. Lead-free perovskites for X-ray detecting. *Sci Bull*. 2017;62(22):1491-1493. doi:10.1016/j.scib.2017.10.013

110. Zhou Y, Sternlicht H, Padture NP. Transmission Electron Microscopy of Halide Perovskite Materials and Devices. *Joule*. 2019;3(3):641-661. doi:10.1016/j.joule.2018.12.011

111. Lang F, Juma A, Somsongkul V, Dittrich T, Arunchaiya M. Rutherford Backscattering Spectroscopy of Mass Transport by Transformation of PbI2 into CH3NH3PbI3 within np-TiO2. *Hybrid Mater*. 2015;1(1). doi:10.2478/hyma-2014-0002

112. Büchele P, Richter M, Tedde SF, Matt GJ, Ankah GN, Fischer R, Biele M, Metzger W, Lilliu S, Bikondoa O, et al. X-ray imaging with scintillator-sensitized hybrid organic photodetectors. *Nat Photonics*. 2015;9(12):843-848. doi:10.1038/nphoton.2015.216

113. Temiño I, Basiricò L, Fratelli I, Tamayo A, Ciavatti A, Mas-Torrent M, Fraboni B. Morphology and mobility as tools to control and

unprecedentedly enhance X-ray sensitivity in organic thin-films. *Nat Commun*. 2020;11(1):1-10. doi:10.1038/s41467-020-15974-7
114. Leijten ZJWA, Keizer ADA, De With G, Friedrich H. Quantitative Analysis of Electron Beam Damage in Organic Thin Films. *J Phys Chem C*. 2017;121(19):10552-10561. doi:10.1021/acs.jpcc.7b01749
115. Raval HN, Sutar DS, Nair PR, Ramgopal Rao V. Investigation of effects of ionizing radiation exposure on material properties of organic semiconducting oligomer-Pentacene. *Org Electron*. 2013;14(6). doi:10.1016/j.orgel.2013.02.018
116. Raval HN, Tiwari SP, Navan RR, Rao VR. Determining ionizing radiation using sensors based on organic semiconducting material. *Appl Phys Lett*. 2009;94(12). doi:10.1063/1.3107266
117. Kim JJ, Ha JM, Lee HM, Raza HS, Park JW, Cho SO. Effect of Electron-Beam Irradiation on Organic Semiconductor and Its Application for Transistor-Based Dosimeters. *ACS Appl Mater Interfaces*. 2016;8(30). doi:10.1021/acsami.6b05555
118. Neuhold A, Novák J, Flesch HG, Moser A, Djuric T, Grodd L, Grigorian S, Pietsch U, Resel R. X-ray radiation damage of organic semiconductor thin films during grazing incidence diffraction experiments. *Nucl Instruments Methods Phys Res Sect B Beam Interact with Mater Atoms*. 2012;284:64-68. doi:10.1016/j.nimb.2011.07.105
119. Fraboni B, Ciavatti A, Merlo F, Pasquini L, Cavallini A, Quaranta A, Bonfiglio A, Fraleoni-Morgera A. Organic semiconducting single crystals as next generation of low-cost, room-temperature electrical X-ray detectors. *Adv Mater*. 2012;24(17):2289-2293. doi:10.1002/adma.201200283
120. Edri E, Kirmayer S, Mukhopadhyay S, Gartsman K, Hodes G, Cahen D. Elucidating the charge carrier separation and working mechanism of CH 3 NH 3 PbI 3-x Cl x perovskite solar cells. *Nat Commun*. 2014;5:1-8. doi:10.1038/ncomms4461
121. Yang S, Xu Z, Xue S, Kandlakunta P, Cao L, Huang J. Organohalide Lead Perovskites: More Stable than Glass under Gamma-Ray Radiation. *Adv Mater*. 2019;31(4):1-7. doi:10.1002/adma.201805547
122. Arnold AJ, Shi T, Jovanovic I, Das S. Extraordinary Radiation Hardness of Atomically Thin MoS 2. *ACS Appl Mater Interfaces*. 2019;11(8):8391-8399. doi:10.1021/acsami.8b18659
123. Gao J, Li B, Tan J, Chow P, Lu TM, Koratkar N. Aging of Transition Metal Dichalcogenide Monolayers. *ACS Nano*. 2016;10(2):2628-2635. doi:10.1021/acsnano.5b07677
124. Brinker CJ, Scherer GW. *Sol-Gel Science: The Physics and Chemistry of Sol-Gel Processing*.; 1990. doi:10.1016/C2009-0-22386-5
125. Brinker CJ, Hurd AJ, Frye GC, Ward KJ, Ashley CS. Sol-gel thin film formation. *J Non Cryst Solids*. 1990;121(1-3). doi:10.1016/0022-

3093(90)90147-E

126. Viscosity, Surface Tension, Specific Density and Molecular Weight of Selected Liquids. https://www.accudynetest.com/visc_table.html?sortby=sort_molecular_weight DESC#004

127. Patterson AL. The scherrer formula for X-ray particle size determination. *Phys Rev*. 1939;56(10). doi:10.1103/PhysRev.56.978

128. Li H, Zhang Q, Chong Ray Yap C, Kang Tay B, Hang Tong Edwin T, Olivier A, Baillargeat D. From Bulk to Monolayer MoS 2 : Evolution of Raman Scattering. *Adv Funct Mater*. 2012;22:1385-1390. doi:10.1002/adfm.201102111

129. Buscema M, Steele GA, Zant HSJ Van Der, Castellanos-gomez A. The effect of the substrate on the Raman and photoluminescence emission of atomically thin MoS2. *Nano Res*. 2014;7:561-571. https://arxiv.org/ftp/arxiv/papers/1311/1311.3869.pdf

130. Briggs D. X-ray photoelectron spectroscopy (XPS). *Handb Adhes Second Ed*. Published online 2005:621-622. doi:10.1002/0470014229.ch22

131. Kumar Panigrahi P, Pathak A. Aqueous Medium Synthesis Route for Randomly Stacked Molybdenum Disulfide. *J Nanoparticles*. 2013;2013. doi:10.1155/2013/671214

132. George A, Fistul M V., Gruenewald M, Kaiser D, Lehnert T, Mupparapu R, Neumann C, Hübner U, Schaal M, Masurkar N, et al. Giant persistent photoconductivity in monolayer MoS2 field-effect transistors. *npj 2D Mater Appl*. 2021;5(1). doi:10.1038/s41699-020-00182-0

133. Tommasino F, Rovituso M, Fabiano S, Piffer S, Manea C, Lorentini S, Lanzone S, Wang Z, Pasini M, Burger WJ, et al. Proton beam characterization in the experimental room of the Trento Proton Therapy facility. *Nucl Instruments Methods Phys Res Sect A Accel Spectrometers, Detect Assoc Equip*. 2017;869. doi:10.1016/j.nima.2017.06.017

134. Li X, Zhu H. Two-dimensional MoS2: Properties, preparation, and applications. *J Mater*. 2015;1(1):33-44. doi:10.1016/j.jmat.2015.03.003

135. Furchi MM, Polyushkin DK, Pospischil A, Mueller T. Mechanisms of photoconductivity in atomically thin MoS2. *Nano Lett*. 2014;14(11). doi:10.1021/nl502339q

136. Coats AW, Redfern JP. Thermogravimetric analysis. A review. *Analyst*. 1963;88(1053). doi:10.1039/AN9638800906

List of Figures